EFFECTS OF BAROCLINICITY ON STORM DIVERGENCE AND STRATIFORM RAIN IN A PRECIPITATING SUBTROPICAL REGION

A Thesis

by

LARRY JOHN HOPPER, JR.

Submitted to the Office of Graduate Studies of
Texas A&M University
in partial fulfillment of the requirements for the degree of

MASTER OF SCIENCE

May 2008

Major Subject: Atmospheric Sciences

EFFECTS OF BAROCLINICITY ON STORM DIVERGENCE AND STRATIFORM RAIN IN A PRECIPITATING SUBTROPICAL REGION

A Thesis

by

LARRY JOHN HOPPER, JR.

Submitted to the Office of Graduate Studies of
Texas A&M University
in partial fulfillment of the requirements for the degree of

MASTER OF SCIENCE

Approved by:

Chair of Committee,	Courtney Schumacher
Committee Members,	Brent Miller
	Fuqing Zhang
Head of Department,	Kenneth Bowman

May 2008

Major Subject: Atmospheric Sciences

ABSTRACT

Effects of Baroclinicity on Storm Divergence and Stratiform Rain
in a Precipitating Subtropical Region. (May 2008)
Larry John Hopper, Jr., B.S., University of Oklahoma
Chair of Advisory Committee: Dr. Courtney Schumacher

Divergence structures associated with the spectrum of precipitating systems in the subtropics and midlatitudes are not well documented. A mesoscale model (MM5) is employed to quantify the relative importance different baroclinic environments have on divergence profiles for common storm types in southeast Texas, a subtropical region. Divergence profiles averaged over a 100 x 100 nested grid with 3-km grid spacing are calculated from the model-derived wind fields for each storm. The divergence profiles simulated for selected storms are consistent with those calculated from an S-band radar using the velocity-azimuth display (VAD) technique.

Divergence profiles from well-modeled storms vary in magnitude and structure across the spectrum of baroclinicities and storm types common in southeast Texas. Barotropic storms more characteristic of the Tropics generate the most elevated divergence (and thus diabatic heating) structures with the largest magnitudes. As the degree of baroclinicity increases, stratiform area fractions increase while the levels of non-divergence (LNDs) decrease. However, some weakly baroclinic storms contain stratiform area fractions and divergence profiles with magnitudes and LNDs that are

similar to barotropic storms, despite having lower tropopause heights and less deep convection. Additional convection forms after the passage of some of the modeled barotropic and weakly baroclinic storms that contain elevated divergence signatures, circumstantially suggesting that heating at upper-levels may cause diabatic feedbacks that help drive regions of persistent convection in the subtropics.

Applying a two-dimensional stratiform-convective separation algorithm to MM5 reflectivity data generates realistic stratiform and convective divergence signals. Stratiform regions in barotropic storms contain thicker, more elevated mid-level convergence structures with larger magnitudes than strongly baroclinic storms, while weakly baroclinic storms have LNDs that fall somewhere in between with magnitudes similar to barotropic storms. Divergence profiles within convective regions typically become more elevated as baroclinicity decreases, although variations in magnitude are less coherent. These simulations suggest that MM5 adequately captures mass field perturbations within convective *and* stratiform regions, the latter of which produces diabatic feedbacks capable of generating additional convection. As a result, future research determining the climatological dynamic response caused by divergence profiles in MM5 may be feasible.

ACKNOWLEDGEMENTS

I would like to thank my parents, sisters, and grandparents for their unwavering support and encouragement throughout my academic career and for trusting my decision to leave Oklahoma back in July 2005 when I had the opportunity to stay. They have all listened to my successes and struggles with research and gave me the strength to persist when I needed it most. Many of my high school and college friends back in Oklahoma and here at Texas A&M have also been very supportive, especially Emily Riley, who has listened to virtually all of my scientific struggles more than anyone else.

I would like to thank my committee chair, Dr. Schumacher, and my committee members, Dr. Zhang and Dr. Miller, for their guidance and support throughout the course of this research. Dr. Schumacher has been especially helpful in listening to my future personal and career goals while helping me develop into the best scientist and person I can be.

Thanks also go to Cameron Homeyer for cleaning up the code created by Dr. Brian Mapes at the University of Miami and Dr. Jialin Lin at NOAA's Climate Diagnostics Center in Boulder, CO so that it could be used with our radar data. I also thank Neil Smith and Shuguang Wang for the technical support they provided and to Zhiyong (Ellie) Meng, Jason Sippel, and Shuguang for the numerous helpful discussions I had with them over the past few years. These contributions allowed me to take advantage of the outstanding students and staff we have in this department to write the best scientific thesis I could at this point in my career.

TABLE OF CONTENTS

Page

1. INTRODUCTION

Atmospheric motions are driven by variations in the vertical structure of diabatic heating and the related horizontal divergence profiles that arise from deep convection. The ability of future higher-resolution global climate and circulation models to predict global precipitation patterns accurately will likely depend upon how well these models parameterize the large-scale dynamic feedback caused by precipitating cloud systems. Haynes and McIntyre (1987) were among the first to suggest that cloud-scale effects on the synoptic-scale vorticity field may need to be parameterized, particularly mesoscale diabatic heat sources that induce synoptic motions. They also showed that the generation of potential vorticity is directly proportional to the local vertical gradient of the diabatic heating rate, which has important dynamic implications because this can cause additional convection to form.

Although many studies have shown that the vertical distribution of heating in the atmosphere causes changes in divergence, heating is a derived quantity in observational meteorology. Calculations of heating consist of estimates of vertical mass fluxes, which are derived from measurements of the horizontal wind divergence. Mapes and Houze (1993a) contend that because these divergence profiles are integrated vertically to get a mean vertical velocity and multiplied by the time-invariant static stability to yield heating profiles, divergence errors at one level are smeared to all levels in the resulting heating profiles and therefore cause the heating profiles to look similar from case to

---

This thesis follows the style of *Monthly Weather Review*.

case. On the other hand, divergence is estimated from direct measurements of the vertical distribution of the horizontal wind field from sounding data, wind profilers, and airborne, ground-based, or dual-Doppler radars. Further, Mapes and Houze (1995) used a scale analysis argument to show that the diabatic divergence greatly exceeds the adiabatic divergence in tropical mesoscale convective systems (MCSs). Adiabatic temperature perturbations noted in this study are too small (<1^{o}C) to support high values of adiabatic heating for any extended period of time, although the latent heating associated with just 1 cm of rainfall can support large sustained magnitudes of diabatic heating. Therefore, the diabatic component of divergence is nearly equal to the actual horizontal divergence and thus can be used to estimate atmospheric heating in tropical convection. This thesis attempts to control the number of potential error sources by presenting observational and model-derived horizontal divergence calculations instead of diabatic heating calculations for a variety of subtropical storm types that frequently occur within varying degrees of environmental baroclinicity in southeast Texas. Once these differences are established, future work will focus on developing idealized diabatic heating profiles for different subtropical storm types and baroclinicities that can be applied to investigate the large-scale response they cause in global models.

a. Deep convection and stratiform rain in the Tropics

Nearly all tropical rainfall is the product of convection, with convective rain resulting from young, vigorous convection and stratiform rain resulting from older, less active convection with radar echoes that have some combination of a weak horizontal

gradient, layered vertical structure, and a bright band (Houze 1997). This thesis does not differentiate a third intermediate (or transition) region used in some of the literature because Houze (1997) indicates the region's microphysical and dynamical processes are more closely related to those found in stratiform precipitation. Figure 1 illustrates some of the idealized microphysical and kinematic differences between vigorous convection and old convection, or stratiform rain. Convective precipitation areas contain strong maximum vertical velocities ($|w| \sim$ 1-10 m s^{-1}) and high rain rates (> 5 mm hr^{-1}) whereas stratiform precipitation regions have lower rain rates (< 5 mm hr^{-1}) and vertical velocities that are generally an order of magnitude smaller than those in convective regions ($|w| <$ 1 m s^{-1}; Houze 1993). Convective updrafts supply moisture to the cloud and increase the time precipitation particles grow within the cloud (primarily by collection) until they fall out of the updraft cores or become too large. The weaker, more mesoscale updrafts in decaying convection and regions of stratiform precipitation enable precipitation particles to grow (primarily by vapor diffusion) as they settle down from higher levels in the cloud. Steiner and Smith (1998) note that the melting of aggregates, ice particles that collect other ice particles of similar habits, at the melting level is the physical explanation for why bright bands are evident in vertical cross-sections of radar reflectivity in stratiform rain. Stratiform radar echo are generally more widespread (~100-km horizontal dimension) and horizontally homogenous than smaller (~1-10-km horizontal dimension), more intense convective radar echo.

Meteorologists widely believed that stratiform precipitation resulted from baroclinicity in mid-latitude cyclones and fronts until Schupiatsky et al. (1975, 1976a,b)

produced radar display photographs of a strong bright-band echo region in the Intertropical Convergence Zone of the eastern Atlantic. Numerous radar studies resulting from the Global Atmospheric Research Program's Atlantic Tropical Experiment (GATE) confirmed and expanded upon the Schupiatsky et al.'s studies. Lopez (1976, 1978) and Houze and Cheng (1977) showed that large stratiform radar echoes on the scale of 10^3-10^4 km^2 in area were present in the Tropics along with areas of primarily convective radar echoes. Houze (1977) showed that large areas of stratiform precipitation falling from widespread anvil clouds contained small 1-10 km^2 cores of convective rainfall within a distinctly mesoscale region. This study also found that, on average, 40% of tropical rainfall reaching the ocean surface in GATE was stratiform, a result verified recently by Schumacher and Houze (2003) using TRMM satellite data.

Beginning with Riehl and Malkus (1958), it was well understood that deep cumulus-scale "hot" towers of convection over the equatorial oceans were the primary driver of the large-scale circulation through the transport of heat from the planetary boundary layer to the upper troposphere; however, the effect that mesoscale vertical motions within larger tropical cloud clusters had upon the large-scale circulation was not. Using indirect thermodynamic evidence from a tropical leading-line trailing stratiform mesoscale convective system (LLTS-MCS) in the central Pacific, Zipser (1969) first identified the presence of a low-level unsaturated mesoscale downdraft within the trailing stratiform region. This mesoscale downdraft transported cold, dry mid-tropospheric air to lower levels and was reinforced by evaporative cooling from widespread rain falling from the midlevel base of the anvil cloud. Convective growth

immediately behind the system (~6-12 h) was discouraged, but new convection along the leading edge of the cold pool was encouraged as commonly seen in midlatitude LLTS-MCSs. The mesoscale downdrafts seen in this study and in oceanic cloud clusters by Riehl (1969) and Venezuelan cumulonimbus by Betts (1973) undoubtedly influenced the initiatives of GATE and likely influenced many others to pursue studies on stratiform rain, to which GATE greatly contributed.

Scientists began to make progress in understanding the complexity of the heat and moisture budgets in the Tropics, which are necessary for parameterizing convection in numerical models, by the time the GATE occurred during the summer of 1974. Previous to GATE, Reed and Recker (1971) successfully computed diabatic heating from sounding-based heat and moisture budgets and measured divergence and variations in vertical motion within different phases of synoptic-scale tropical easterly waves. Moisture availability and heating were found to be greatest upstream from the trough axis. Differences in diabatic heating between trough and ridge regions exceeded $8^{o}C\ day^{-1}$ at 400 hPa. Yanai et al. (1973) advanced these findings by combining the observed large-scale heat and moisture budgets with an entrainment-detrainment model of a cumulus cloud ensemble to calculate bulk heating and moisture quantities of tropical cloud clusters. Yanai and his colleagues found that clouds affect their environment by causing large-scale heating in compensating downward motions through dry adiabatic subsidence warming and by causing large-scale cooling through detrainment of water vapor and liquid water from clouds. Even with these advances, scientists in the early 1970s were beginning to question the applicability of numerical results using the

existing cumulus parameterization schemes because the schemes inadequately represented cloud clusters containing stratiform rain (Houze and Betts 1981).

b. Tropical divergence and heating

Gamache and Houze (1982) were among the first to show that vertical air motions associated with stratiform and convective rain within a tropical LLTS-MCS during GATE induce two very different atmospheric responses. Figure 2 shows that the mean horizontal divergence profile for tropical LLTS-MCSs predominantly consists of low-level convergence and upper-level divergence with some surface divergence. Convective cells induce a two-layered atmospheric response characterized by strong convergence at low-levels and strong divergence aloft, whereas stratiform precipitation areas induce a three-layered response characterized by moderate convergence at the 0^{o}C level and moderate divergence at lower and upper levels. Additional experiments performed in MCSs during the Australian monsoon (Mapes and Houze 1993a) and in the western Pacific (Mapes and Houze 1995) yield similar divergence structures, although the magnitudes are somewhat higher.

Mapes and Houze (1995) clarified how the synoptic and planetary-scale atmosphere adjusts to disturbances in its mass field from deep tropical convection by forcing a linear spectral primitive-equation model with diabatic divergence profiles observed within tropical MCSs during the Tropical Ocean-Global Atmosphere program's Coupled Ocean-Atmosphere Response Experiment (TOGA-COARE). Figure 3a displays the spectral transform of the Doppler radar "purl" divergence measurements

and Fig. 3b shows the model-derived temperature perturbation fields that exist six hours after mesoscale latent heating sources have begun. These "purl" measurements were obtained by flying Doppler radar-bearing aircraft in tight circles intermittently along their generally straight flight paths. Two distinct gravity wave bores are evident in Fig. 3a, with a divergence minimum (convergence maximum) characteristic of stratiform rain regions at 23 m s^{-1} and a divergence maximum typical of convective regions at 52 m s^{-1}. The atmosphere adjusts to active tropical convection through compensating subsidence represented in the form of the fast-moving convective gravity wave bore that balances the convergent inflow at low levels with divergent outflow aloft. Because stratiform regions typically have maximum convergence at midlevels, the slower-moving gravity wave bore displaces mass upward in the lower troposphere and downward in the upper troposphere to balance the low-level mesoscale downdraft and upper-level updraft.

Figure 3b shows that the fast convective gravity wave bore causes deep adiabatic subsidence warming throughout the troposphere with a maximum near 1000 km at mid-levels, which suppresses convection in these areas. Conversely, the slower-moving stratiform gravity wave bore causes generalized subsidence warming above 500 hPa and cooling below 500 hPa due to adiabatic upward motions from about 150-600 km. Therefore, stratiform rain regions cause gravity waves that encourage rising motion and new convection to form within and near existing MCSs. Mapes and Houze (1995) reinforced the study of Mapes (1993), which also simulated two distinct gravity wave buoyancy bores propagating away from a slab-symmetric heat source characteristic of tropical MCSs, where the slower buoyancy bore also caused adiabatic upward

displacements favoring additional convection near the heat source at low levels. Combining these modeling implications with observations of persistent west Pacific superclusters in Mapes and Houze (1993b), Mapes (1993) theorized that tropical deep convection is gregarious and can have a positive feedback on the large-scale circulation by generating planetary waves.

Other studies before Mapes' work have shown that elevated diabatic heating within mature tropical MCSs has nontrivial feedbacks on the large-scale circulation. This elevated heating pattern is also evident in the stratiform gravity wave bore shown in Fig. 3b. Houze (1982) was among the first to distinguish the difference in diabatic heating caused by mature cloud clusters containing large amounts of stratiform rain from that produced by isolated convective towers. Houze (1982) showed that latent heating and cooling due to condensational processes in convective and stratiform updrafts and evaporation in downdrafts dominate the total heating while convection is active. The sensible heat flux (which is independent of moist processes) due to these same updrafts and downdrafts is secondary but still can contribute a significant amount of heating, whereas radiative processes within convection only have a small contribution to total heating. However, the absorption of longwave and shortwave radiation within anvil cloud decks connecting the active cumulonimbus of a cloud cluster continues to heat the upper troposphere long after deep convection ceases, causing an enhancement of diabatic heating near 400 hPa. Hartmann et al. (1984) forced a simple linear steady-state global model with Houze's (1982) idealized heating structures and found that the mature cloud cluster produced a more realistic Walker Circulation with centers at the observed

altitudes (~400 hPa) and a westward tilt with height compared to the convective heating profile, which produced unrealistic lower circulation centers (~500 hPa) without a westward tilt. DeMaria (1985) was also able to simulate similar realistic responses to tropical heating from summertime convection in South America using an elevated heating profile.

Although the aforementioned studies are notable advances, Schumacher and Houze (2003) showed that their common assumption of geographically uniform vertical heating profiles is flawed. Their precipitation radar-based study using data from the Tropical Rainfall Measuring Mission (TRMM) found that although stratiform precipitation accounted for 73% of the area covered by rain and 40% of rainfall in the tropics, large temporal and geographical variations in stratiform rain and area fractions were observed, particularly across the equatorial Pacific. Schumacher et al. (2004) compared the dynamical response generated by version 3 of the Community Climate Model (CCM3) when forcing the model with the observed horizontal variations in stratiform rain shown by TRMM as opposed to geographically uniform stratiform rain fractions of 0%, 40% and 70%. Including the geographical variations in stratiform rain fraction produced a model response most similar to that evoked by the uniform 40% case because this is closest to the global annually averaged stratiform rain fraction. However, the non-uniform case also contained larger horizontal variations in the height and vertical extent of ω and its associated circulation centers, causing a more realistic westward tilt in the zonal wind field, similar to the results of Hartmann et al. (1984). Schumacher et al. (2004) also found that the large-scale response is even more sensitive

to latent heating variations during El Niño when the east-west gradient in stratiform rain fraction is more pronounced than usual, further supporting the conclusion that the large-scale circulation is very sensitive to stratiform precipitation variations in the Tropics.

c. Extratropical divergence and heating

Although many studies have investigated how the vertical structure of divergence and diabatic heating associated with deep convection influences the large-scale dynamical response in the tropics, the effect precipitating systems have on the large-scale circulation is not as well understood in the subtropics or midlatitudes. Recent case studies suggest that midlatitude convection may feedback on the large-scale circulation at mesoscale to synoptic scales (~ 500 km) within weakly baroclinic environments by inducing cyclogenesis and intensifying frontogenesis**.** Zhang and Harvey (1995) showed how a LLTS-MCS over the Central Plains influenced the development of a midlatitude cyclone by increasing the phase lag between the pressure and thermal waves, thereby enhancing the environmental baroclinicity and providing more favorable conditions for surface cyclogenesis. Mesoscale model simulations neglecting moist convective processes produced a surface cyclone from the initial environment baroclinicity with much weaker intensity, smaller horizontal extent, and slower displacement than simulations including moist convective feedbacks. Using the fifth-generation Pennsylvania State University-National Center for Atmospheric Research (PSU-NCAR) nonhydrostatic Mesoscale Model (MM5), Bryan and Fritsch (2000) also found that horizontal variations in diabatic heating within a frontal MCS can create a temperature

gradient and mesoscale pressure perturbation that alters the wind field. This induces confluence and tilting frontogenesis along a separate, rapidly intensifying boundary that makes the original cold front appear to be propagating discretely. This discrete propagation is not evident for sensitivity experiments that neglect the effects of cloud radiative heating and precipitation, suggesting that diabatic processes can sometimes overwhelm preexisting baroclinic temperature gradients and drive midlatitude frontogenesis.

Diabatic heating is also critical in maintaining the two major Northern Hemispheric storm tracks off the east coasts of Asia and North American where relatively warm sea-surface temperatures (SSTs) reside. Hoskins and Valdes (1990) found that large-scale latent heat release in warm air just east of these coasts causes disturbances to intensify, suggesting that condensational heating helps maintain enhanced baroclinicities in the entrance regions of the Pacific and Atlantic storm tracks. Chang et al. (2002) also described how diabatic heating from condensational processes within the warm sector of incipient cyclones strengthens midlatitude storm tracks, but indicated that deep convection inhibits cyclogenesis because it generally occurs in cold air behind a cold front. In agreement with Chang (2001), they also observed a distinct midwinter suppression of the Pacific storm track when the background baroclinicity is strongest and surface sensible heat fluxes generally overwhelm condensational heating. However, Chang (2001) also recognized that although diabatic heating dissipates eddy potential energy during midwinter, it generates eddy potential energy during fall and spring when condensational heating is larger. Since Mapes and Houze (1995) showed

that diabatic heating is nearly equal to horizontal divergence in tropical convection, one can surmise that variations in horizontal divergence within extratropical precipitating systems also has some effect on storm tracks and cyclogenesis.

Many studies have documented how some extratropical MCSs and mesoscale convective complexes (MCCs) generate upper-tropospheric anticyclonic and mid-tropospheric cyclonic perturbations. Ninomiya (1971a,b) was one of the first to recognize that mesoscale outflow from a group of midlatitude thunderstorms can create a warm core anticyclone maintained by diabatic heating that increases the large-scale baroclinicity and intensifies upper-level divergence and lower-level convergence. Maddox et al. (1981) also identified strong changes in upper-tropospheric temperatures, wind, and 200 hPa heights within a central Mississippi Valley MCC over only 6 h, leading them to surmise that a deep layer of mid-tropospheric convective warming induced a mesoscale mass circulation that intensified upper-level divergence and jet streaks in the vicinity of persistent convection. A study of the same MCC performed by Keyser and Johnson (1984) attributed the upper-tropospheric perturbations associated with the intense mesoscale mass circulation to the strong vertical diabatic mass flux within the MCC. Diabatically forced ageostrophic motions in the right entrance region of the jet streak directed along the synoptic scale pressure gradient intensified the thermally direct mass circulation and generated kinetic energy that produced stronger winds in the jet streak downstream. Some studies have also investigated what causes long-lived mesoscale convective vortices (MCVs) to develop at midlevels within stratiform regions of extratropical MCSs, although Bartels and Maddox (1991) estimate that only a fraction

of MCSs (less than 5%) generate a persistent MCV that is still visible on satellite imagery after the MCS's cirrus deck dissipates. Because preexisting vortices may explain why some relatively small, short-lived convective systems generate MCVs in their study, Bartels and Maddox speculate that both the background environment and magnitude and duration of latent heating may control whether many convective systems develop persistent MCVs or not.

Individual MCSs generally have lifetimes that are too short to significantly affect the large-scale environment at synoptic to planetary scales (> 1000 km); however, Stensrud (1996) demonstrated that the cumulative effects of an entire group of MCSs occurring in the southern Plains over roughly three days produced significant changes in the large-scale flow patterns. MM4 simulations including the diabatic effects of convection enhanced the baroclinicity and inflow of warm, moist air at low-levels and produced significant upper-level perturbations over a 50^{o} longitude spread, encouraging additional convection to form. Global rainfall analyses and barotropic model runs performed over multiple years by Stensrud and Anderson (2001) showed that persistent convection caused by MCSs in central North America and southeast Asia can produce source regions for Rossby waves that alter midlatitude circulation patterns. Stensrud and Anderson further suggest that the continuous succession of MCSs during the 1993 Midwestern floods may have significantly altered the hemispheric circulation by producing persistent upper-level divergence that encouraged low-level convection. Bell and Janowiak (1995) identified a 200 hPa divergence anomaly centered over eastern Nebraska during the summer of 1993 (Fig. 4b), which Stensrud and Anderson (2001)

nearly collocated with the tropical-like frequencies (> 20%) of cold cloud-top temperatures less than -38^{o}C observed by satellite (Fig. 4a). Future research will determine if similar mechanisms caused persistent regions of convection responsible for widespread flooding in the southern Plains during the anomalous[1] spring and summer of 2007, during which some cases presented in this thesis occurred. This widespread, long-term flooding event along with numerous shorter-term warm season flooding events throughout Texas since 1993 (i.e., southeast Texas in October 1994 and Texas Hill Country in October 1998 and July 2002) underscore the importance of investigating the large-scale feedbacks of persistent midlatitude and subtropical convective activity.

[1]According to the NCDC, June-August 2007 was Texas' wettest and Oklahoma's fourth wettest summer on record. Similarly, March 2007 was Texas' wettest March on record. (http://lwf.ncdc.noaa.gov/oa/climate/research/2007/cmb-prod-us-2007.html)

2. BAROCLINICITY AND STORM TYPES IN THE SUBTROPICS

Southeast Texas, a subtropical location, experiences a wide range of precipitating systems and background environments commonly found in both the tropics and midlatitudes, making the region ideal for investigating how storm divergence and stratiform rain production vary across different baroclinicities and storm types. Conventional definitions place the subtropics between the 20^{o} and 35^{o} latitudes in both hemispheres, separating the Tropics from more temperate midlatitude climates. The subtropics are assumed to be a zonally uniform region of subsidence warming in the downward branch of the thermally direct Hadley circulation, which is primarily responsible for transporting heat and energy away from the Tropics to about 31^{o}N and 31^{o}S (Trenberth and Stepaniak 2003). Trenberth and Stepaniak also note that subsidence warming in the subtropics is compensated by the cooling predominantly caused by transient baroclinic eddies, which are strongest in the winter hemisphere and transport heat and energy to the midlatitudes. However, the Hadley cell is considerably smaller and weaker in the summer hemisphere when the latitude of maximum heating and ICTZ is shifted closer to the subtropical region in question, such that the effects of generalized subsidence warming are reduced. Furthermore, Cook (2003) showed that land surfaces enhanced these seasonal variations by doubling the intensity of the winter hemisphere Hadley cell and weakening the summer cell by a factor of two, suggesting that the traditional axisymmetric model neglecting the effect of land distributions may not accurately capture the intensity of the mean meridional circulation.

a. Baroclinicity in the subtropics

Seasonal variations in the subtropical latitudes cause the region to experience a wide array of baroclinicities. Holton (1992) defines a barotropic atmosphere as one in which density is only a function of pressure, whereas density is a function of both pressure and temperature in a baroclinic environment. Unlike in barotropic environments where contours of constant height, thickness, and temperature are all parallel, contours of constant height and thickness intersect in baroclinic environments and cause the geostrophic wind to flow across isotherms, causing much stronger horizontal temperature gradients and vertical wind shears by the thermal wind relationship (Wallace and Hobbs 1977). Purely barotropic conditions—where pressure surfaces are vertically stacked, the direction and speed of the geostrophic wind is independent of height, and no horizontal temperature gradients exist—are highly idealized and rarely exist at the same time even in the tropics, which is generally considered a barotropic environment. Equivalent barotropic atmospheres, defined by Wallace and Hobbs (1977) as regions where thickness and height contours are parallel in the presence of horizontal temperature gradients, are more common and dictate that the geostrophic wind speed may vary with height while maintaining constant direction.

Barotropic conditions typical of the tropics predominate in the subtropics during the summer months when the strength and southern penetration of midlatitude cyclones decrease, causing much weaker vertical wind shear and weak horizontal temperature gradients. Fritsch and Forbes (2001) note that convective systems forming in these types of environments tend to depend more strongly on features and processes imposed by the

convection itself, such as the moist-downdraft production of a surface based cold pool and the large stratiform and anvil cloud shield characteristic of MCCs. Conversely, when baroclinic conditions with strong horizontal temperature gradients and vertical wind shears common to the midlatitudes predominate in the subtropics, storms are thought to have a much less active large-scale feedback and develop primarily from externally imposed forcings like frontal systems and other mesoscale components of synoptic-scale baroclinic systems. However, considering the fact that the subtropics are a transition zone, Brugman (2007) suggests that a mixture of barotropic and baroclinic conditions appear to occur during the transitional seasons of spring and autumn in southeast Texas, when most convective systems appear to arise from weakly baroclinic background environments with either moderate horizontal temperature gradients, wind shears, or a combination of both. Although additional research is needed to better quantify subtropical baroclinicities, it is likely that subtropical locations like southeast Texas tend to experience these weakly baroclinic types of environments frequently, and that the storms associated with these environments may have a greater convective feedback on the large-scale circulation than previously thought.

b. Storm types in the subtropics

Seasonal variations also cause the subtropics to experience a wide variety of storm types. Brugman (2007) developed a climatology of storm types for southeast Texas (Table 1) based upon both dynamical forcing and precipitation structure during the time a particular storm was is in its most mature stage over a disdrometer site in

College Station, Texas (30.7°N, 96.4°W). Frontal systems composed over half (57%) of the 74 storms observed from December 2004-November 2006, with cold fronts and stationary fronts contributing the most to these systems. Brugman (2007) found that convective and non-convective frontal storm types were typical of weakly and strongly baroclinic environments, while non-frontal storm types (i.e., weak forcing, drylines, and upper-level disturbances) were common in barotropic environments. Cold fronts usually tended to be more strongly baroclinic than stationary fronts, many of which would fall into a more weakly baroclinic category. Storms caused by more barotropic influences, or weak forcing, contributed to 22% of the total. The study suggests that drylines, warm fronts, and upper-level disturbances do not make up a large percentage of storms in southeast Texas, although preliminary studies extending the climatology through more years of data indicate that upper-level disturbances contribute more than the 12% Brugman's study indicates. Upper-level disturbances are also very important in studying differences in storm divergence and stratiform rain production because it is the only forcing that appears to be prevalent across all degrees of baroclinicity.

The storms presented for comparison in this thesis were selected because of their ability to model relatively well in MM5, their large areal coverage, and comparability to similar storm types with different baroclinicities. Convective lines and isolated scattered convective cases containing little stratiform rain do not model well at the resolutions selected for this study and are generally not large enough to generate useful MM5-based divergence calculations or radar-based divergence measurements using the velocity-azimuth display (VAD) technique (Mapes and Lin 2005). In addition, Brugman (2007)

indicated that most storms in the subtropics contain relatively large amounts of stratiform rain with the exception of cold frontal convective lines, dryline systems, and isolated convection caused by weak forcing. After describing the methodologies employed in this work (section 3), section 4 will compare MM5-based divergence calculations from representative storms of varying baroclinicities with radar-based divergence measurements using the VAD technique. Section 5 will include additional comparisons of MM5 divergence calculations from common subtropical storm types (frontal LLTS-MCSs, scattered convection from weak forcing, upper-level disturbances, and other frontal systems) of varying baroclinicities. Finally, sensitivity studies underscoring the importance of the ability of model parameterizations to accurately capture stratiform rain processes will be given in section 6 before conclusions are presented in section 7.

3. METHODS

a. Model and calculations

Model simulations of each case are conducted using version 3-7 of the fifth-generation NCAR-PSU nonhydrostatic Mesoscale Model, or MM5 (Dudhia 1993). The 27-km resolution outermost coarse domain (D1) consists of 133 x 133 grid points with 27 vertical sigma levels covering the majority of the continental United States and Mexico (Fig. 5). The second domain (D2) incorporates 130 x 130 grid points with 9-km grid spacing, while the inner-most 3-km resolution domain (D3) contains 100 x 100 grid points. Initial and lateral boundary conditions are created using the National Centers for Environmental Prediction (NCEP) Global Final Tropospheric Analysis with 1^{o} horizontal and 6-h temporal resolution, and two-way nesting is utilized for the lateral boundary conditions of D2 and D3. Each model run was initialized at either 0000 or 1200 UTC because upper-air observations are taken globally at these times. Most model runs were initialized 6-18 hours before the onset of precipitation within the analyzed domain (D3), although a few of the storms were better simulated by initializing the model runs outside of this period. Table 2 lists all of the cases presented in this thesis with the initialization and termination times of each model run, the time period over which all of the model-derived calculations are taken, and the actual time periods of the storm's duration as seen in NEXRAD radar imagery.

A uniform set of schemes is used to parameterize radiative and planetary boundary layer processes for each case (including the sensitivity studies). Radiative processes are handled using a scheme that accounts for longwave and shortwave

interactions in clouds and the clear atmosphere implemented by Dudhia (1989). The planetary boundary layer is parameterized with a high-resolution Blackadar (1976, 1979) scheme adapted for MM5 by Zhang and Anthes (1982) and Zhang and Fritsch (1986) that incorporates the effects of moist vertical diffusion in clouds. Sensitivity tests performed for this study suggest that the Blackadar scheme yields the most realistic three-dimensional wind and radar reflectivity structures (not shown). Similarly, Bright and Mullen (2002) showed that the Blackadar scheme accurately predicted the structure of the planetary boundary layer and convective available potential energy within Arizona summertime convection despite yielding spurious convective inhibition values.

After investigating many different combinations of cumulus and microphysics parameterization schemes, one uniform set of parameterizations appeared to best handle convective and stratiform processes for storms overall. Although a cumulus scheme is not used for either of the two nested domains (D2 and D3), the Grell cumulus parameterization scheme (Grell 1993) is employed on the coarse domain (D1) for all of the model runs simulated in this thesis. This single-cloud scheme, which is most effective for smaller grid sizes ~10-30 km, considers the effects of shear on precipitation efficiency and balances resolved rainfall and convective rainfall. The Goddard explicit microphysics parameterization scheme (Tao and Simpson 1993), which includes cloud ice, snow, and graupel processes, is used on all grids for each case. This scheme appears to simulate stratiform processes better then the Reisner-2 microphysics scheme with graupel (Reisner et al. 1998). Sensitivity tests comparing the vertical structures of simulated horizontal divergence, radar reflectivity, and vertical wind between these two

microphysics schemes are presented in section 6. Employing the Grell cumulus parameterization on D2 is investigated as well, along with the stratiform area fractions generated for different combinations of parameterization schemes run for each case.

Model-derived radar reflectivity (hereafter referred to as MM5 reflectivity) and horizontal divergence are both calculated over D3 during the times for which convection was occurring within the inner-most domain for each storm. The outermost five grid squares are not used in calculating the model-derived values for reflectivity and divergence or in retrieving additional forecast fields because of inconsistencies between the resolved (D3) and parameterized (D2) convection along D3's outer boundary when the Grell cumulus scheme is used on D2. Even though the cases presented in this study do not employ a cumulus parameterization (CP) on D2, the outermost five grid squares are still discarded to maintain consistency with the sensitivity tests presented in section 6. Radar reflectivity calculations are based on Stoelinga's (2005) algorithm, which assumes the size distribution of precipitation particles follows an exponential distribution with fixed intercepts of $8x10^{6}$, $8x10^{7}$, and $4x10^{-4}$ for rain, snow, and graupel, respectively. Although the assumption of fixed intercepts does not affect MM5 reflectivity calculations for the Goddard scheme, it does affect reflectivity calculations for the Reisner-2 scheme with graupel because the Reisner-2 scheme incorporates a mixing-ratio dependent value for the intercept parameter for snow. A more recent version of the Reisner-2 scheme uses a temperature-dependent snow intercept as described in Thompson et al. (2004).

All variables are defined in the middle of each of the 27 vertical layers, or half-sigma levels, except for vertical velocity which is given at each of the 28 full-sigma levels. The horizontal grid has a type-B staggering (Arakawa and Lamb 1977) of horizontal velocity variables (*u, v*) with respect to all other scalar variables (*T, p', q,* etc.) and vertical velocity (*w*) as shown in Fig. 6. Therefore, horizontal divergence is calculated for the center of the grid square using the velocity components collocated at the corners of the square. The horizontal velocity values on both sides of the point for which horizontal divergence is calculated are averaged together before finding the horizontal velocity derivatives of those points (*du, dv*). These horizontal velocity derivates are then divided by the grid spacing (*dx=dy=3000 m*) and added together to get the horizontal divergence (Eq. 1).

$$\delta_h = du/dx + dv/dy \qquad (1)$$

Using the horizontal velocities at the corners of each grid square to calculate horizontal divergence for the center of each grid square where all other model-derived calculations are provided allows each horizontal divergence calculation to be directly correlated with a MM5 reflectivity value. The mean horizontal divergence profiles in sections 4 and 5 only include grid squares whose MM5 reflectivity exceeds 5 dBZ to provide a more direct comparison to previous radar studies. MM5 reflectivity and horizontal divergence is also objectively classified as stratiform or convective using Steiner et al.'s (1995) radar-based algorithm (see section 3b for a description of the Steiner et al. method). The algorithm is applied to MM5 reflectivity values at the seventh half-sigma level above the surface that exceed 5 dBZ.

b. Stratiform-convective separation algorithm

Stratiform and convective areas of precipitation are identified using a radar-based technique developed by Steiner et al. (1995) based on the horizontal structure of the precipitation field. Steiner and his colleagues indicate that identifying stratiform regions based exclusively on the presence of a bright band will underestimate the stratiform component because the bright band is only well defined within mature stratiform precipitation regions. In addition, beam spreading causes the radar data to be too coarse at far ranges ($\geq$ 100 km) to distinguish bright band features that have relatively small vertical extents (~200 m). Steiner et al. also note that although it would be ideal to use vertical velocities to separate stratiform from convective rain regions since this is where the physical distinction lies, doing so would not be practical because vertical velocity information is not readily available from traditional radar observations. Furthermore, devising a separation algorithm on the basis of the horizontal structure of vertical velocity at only one level poses challenges because the storms modeled in this thesis indicate that the level of maximum vertical velocity varies dramatically depending upon the type of convection (i.e., elevated or surface-based) and baroclinicity. For example, although convective rain typically has its strongest vertical velocities in the lower troposphere, Cifelli and Rutledge (1998) showed that monsoonal MCSs near Darwin, Australia usually have the largest magnitudes of convective vertical velocity in the middle-to-upper-troposphere with low values below the 0^{o}C level. Likewise, Cifelli et al. (2000) found that the mean vertical velocity within convective regions in these tropical MCSs is considerably less than 1 m s^{-1}, which the storms modeled in this thesis confirm.

Nevertheless, the presence of a bright band and smaller, more homogeneous vertical velocities with height in stratiform regions are valuable sanity checks that ensure that the separation algorithm is generating reasonable results from both microphysical and kinematic standpoints.

Steiner et al. (1995) applied their separation algorithm to Cartesian-gridded radar reflectivity data from Darwin, Australia. The radar data had 2-km horizontal resolution and the chosen altitude was 3 km because this is far enough below the bright band and high enough to provide radar data out to a 140 km range. In this study, the separation algorithm applied to MM5 reflectivities with 3-km horizontal resolution at the seventh sigma level above the surface for all cases, which generally falls between 1.6-1.7 km in altitude. Selecting a lower level than Steiner et al. (1995) originally used is necessary because midlatitude environments, which are generally cooler and drier than tropical ones, sometimes undergo significant amounts of evaporation in the lower troposphere and have more variable melting levels that may occur below 3 km. In addition, the problem of ground-based radars missing data in the lower troposphere at far ranges due to the Earth's curvature does not apply to model grid points.

Convective centers are identified in the Steiner et al. (1995) separation algorithm for grid points whose radar reflectivities exceed a specified threshold or are significantly higher than nearby reflectivity values. Any grid point in the radar reflectivity field that is 40 dBZ or greater is automatically classified as a convective center because classifying rain of this intensity as stratiform would not be physically reasonable. Grid points that have radar reflectivities below 40 dBZ may still be classified as a convective center if

the reflectivity at that point differs from the mean radar reflectivity (of all echoes greater than 5 dBZ) taken over the grid point's surrounding background radius of 11 km by at least the difference shown by the curve in Fig. 7. This curve, which was applied to radar data collected in Darwin, Australia by Steiner et al. (1995), is given by the piecewise function

$$\Delta Z = \begin{cases} 10, & Z_{bg} < 0 \\ 10 - Z^2_{bg}/180, & 0 \leq Z_{bg} < 42.43, \\ 0, & Z_{bg} \geq 42.43 \end{cases} \qquad (2)$$

Figure 7 shows that the peakedness criteria for previous separation schemes employed by Churchill and Houze (1984) and Steiner and Houze (1993) used constant reflectivity difference values below 5 dB across all mean background reflectivities. Steiner et al. (1995) notes that the Churchill and Houze (1984) algorithm overestimated convective area fractions because several moderate echo cores in the range of 20-30 dBZ were identified as stratiform even though they exhibited a bright band signature. The gradually decreasing peakedness criteria with increasing background reflectivity used by Steiner et al. (1995) helps address this problem. Furthermore, Steiner and his colleagues suggest that the peakedness criteria curve and the specified absolute convective threshold must be tuned to best distinguish convection for a particular region. Although the 40 dBZ convective threshold remains unchanged, the curve is tuned slightly for this thesis (Eq. 3) to better satisfy the variety of cases modeled in this study and the generally higher than observed MM5 reflectivity values.

$$\Delta Z = \begin{cases} 10, & Z_{bg} < 0 \\ 10 - Z^2_{bg}/180, & 0 \le Z_{bg} < 43.75, \\ 0, & Z_{bg} \ge 43.75 \end{cases} \qquad (3)$$

Sensitivity studies performed on this peakedness criteria indicate that changing this curve alters stratiform area fractions but has little effect on the divergence profiles generated for stratiform and convective regions. This finding suggests that the convective and stratiform divergence profiles generated by MM5 are indeed robust instead of being an artifact of how the separation algorithm is tuned.

Once convective centers that satisfy the peakedness criteria or convective intensity threshold are identified, a specified area surrounding each convective center is also classified as convective using the intensity-dependent step function shown in Fig. 8. The remainder of the precipitation is classified as stratiform. Sizes of the surrounding area for the convective radius range from 1-5 km, with larger convective radii generated for increasing values of the mean reflectivity over the 11 km background radius. The heavy solid line labeled “medium” in Fig. 8 is the relation used to determine the size of the convective area radius in this thesis and in Steiner et al.’s (1995) study. This relation produces its maximum convective area radii of 5 km for all reflectivity values that are 40 dBZ or greater. Larger convective radii are created by decreasing the value for the maximum convective radius below 40 dBZ while smaller convective radii are generated if reflectivity values above 40 dBZ are used. Steiner et al. (1995) suggest that although some adjustment of this portion of the algorithm is necessary, it is less important than tuning the peakedness and intensity criteria that establish the convective centers because

the surrounding area criterion appears to be primarily a function of grid resolution instead of precipitation regime. Sensitivity studies performed for the present study affirm this observation, with smaller changes in the divergence profiles and stratiform area fractions than when tuning the portions of the algorithm that determine the convective centers themselves.

c. Radar observations and VAD divergence

Observational results from the Texas A&M University (TAMU) Aggie Doppler Radar (ADRAD) are used to show that the mean divergence profiles generated by MM5 for the cases presented in section 4 are reasonable and that the methodologies utilized in this thesis may be applied across varying storms types and baroclinicities. ADRAD, an S-band Doppler radar, is located on the roof of the fifteen-story Eller Oceanography and Meteorology Building on TAMU's main campus. Figure 9 displays the 16 elevation angles incorporated in the volume scan strategy run every ten minutes by ADRAD and shows how the altitudes of these elevation angles change with range from the radar. A more basic scan strategy excluding the highest four elevation angles is employed for the 7 April 2007 storm. Undergraduate meteorology TAMU students supervised by three graduate students and the principal investigator (PI) of the NSF-CAREER grant funding this project gathered some of the radar data as part of the Student Operational ADRAD Project (SOAP). SOAP students will continue to run ADRAD semi-operationally every spring until 2010, while the PI, graduate students, and SOAP volunteers will run ADRAD ad-hoc during other seasons to obtain a more complete radar climatology.

Mean divergence profiles from ADRAD are generated using a code developed by Mapes and Lin (2005) for tropical convection using the VAD technique (Browning and Wexler 1968). Instead of remapping the radar data to a Cartesian grid, the horizontal space of the ADRAD data is binned into polar coordinates temporally using CYLBIN, a space-time binning algorithm, to retain the range-dependent aspects of the radar's sampling characteristics and to better interpret the radial velocity data. Figure 10 shows this approach schematically; hourly data is separated into 500-m vertical layers and placed in a coarse horizontal grid with twenty-four 15^{o} bins in azimuth and twelve 8-km bins in range. Hourly histograms of radar reflectivity, radial velocity, and other parameters of interest are created. Most importantly, the mean radial velocity is also retained for each spatial grid cell so that it may be used later to calculate mean horizontal divergence using the VAD technique after radial velocities are unfolded.

When there is incomplete echo coverage (whether in time or space), estimates of mean wind and divergence tend to be of poor quality because Doppler radars do not measure radial velocity when hydrometeors or other large particles are not present. Therefore, the cases presented in section 4 were selected because they have very good azimuthal coverage within the analysis domain for many consecutive hours. Additionally, the Mapes and Lin (2005) code "pools" the data in range and height from different original cells into coarser cells by simply adding all the histograms and radial velocities from adjacent cells together to increase the number of available divergence estimates. Because data is generally sparse at upper levels, all data are repooled from 500-m height layers into 50-hPa pressure layers such that some pressure levels further

aloft will have multiple measurements available for analysis, increasing the probability that there will be enough data for a VAD divergence estimate at upper levels. In addition, the VAD divergence estimates from ADRAD pool data in the horizontal by supplementing the data in each 8-km range interval with data from the two adjacent 8-km annuli on both sides. The five-range pooled observed divergence profiles presented in section 4 include the most data with four sets of 40-km annuli centered about 28, 44, 60, and 76 km from ADRAD's center. Similarly, the three-range pooled and raw divergence profiles include four sets of 24-km and 8-km annuli, respectively, centered about the same radii as the five-range pooled data. Although pooling the data in range and height introduces small additional sources of error, the cases shown by Mapes and Lin (2005) and those investigated in this study indicate that the benefits of increasing the coverage in azimuth and at upper levels in otherwise echo-sparse regions to improve mean wind and divergence estimates far outweigh the potential drawbacks. Likewise, the mean divergence estimates using range pooled data from ADRAD are in better agreement with the model-derived mean divergence calculations than those with no range pooled radar data.

4. MODEL AND OBSERVATIONAL COMPARISONS BY BAROCLINICITY

Before applying the methodologies used in this study to a wider range of storm types and baroclinicities, this section presents three storms with disparate degrees of baroclinicity. In particular, model-derived mean divergence profiles are compared to ADRAD's mean divergence profiles calculated using the VAD technique. These storms also test the validity of Steiner et al.'s (1995) convective-stratiform separation algorithm by displaying the MM5 reflectivities, vertical velocities, and divergence profiles that each case generates for each rain type. Table 2 lists the storms investigated in this section along with those in section 5 broken down by storm type. Table 2 also gives the times for which each MM5 run is initialized along with a comparison of the analysis times in MM5 with those they represent in observations. In this section, the barotropic case with tropical-like deep convection and a more midlatitude-like strongly baroclinic case consisting of a wintry mix of stratiform precipitation with a few pockets of elevated convection provide an excellent test of these methodologies by comparing storms at opposite ends of the baroclinicity spectrum. For the weakly baroclinic case, two separate storms are presented that have very different divergence profiles. The first storm highlights the potential importance of diabatic feedbacks and the second storm illustrates how diabatic feedbacks can become overwhelmed by synoptic forcing mechanisms.

a. Barotropic case: 20 July 2007

Many summertime storms in southeast Texas develop in weakly forced environments that lack synoptic forcing from fronts, drylines, or upper-level

disturbances. These storm types account for over one-fifth of all storms in southeast Texas (Table 1; Brugman 2007). The first case study of this section is a storm composed of scattered convection that formed in a barotropic environment on 20 July 2007. This was a period of persistent convection in Texas that began on 14 July, one of many throughout the record-breaking spring and summer of 2007. Thunderstorms began to develop overnight along the upper Texas Gulf coast around 0900 UTC and rapidly increased in areal coverage by forming large stratiform regions from aging deep convection as the system propagated inland later that morning and afternoon. Although MM5 simulates the evolution of convection reasonably well, its timing is delayed because convection does not develop until 1500 UTC. This discrepancy may occur because the model was initialized too late (0000 UTC) to accurately simulate the diabatic feedbacks from the previous day's convection. However, model runs initialized on 19 June at 1200 UTC do not produce convection at the appropriate time either. Figure 11 shows a snapshot comparison of the radar reflectivities determined by NEXRAD with the MM5 reflectivities for this storm. The images of NEXRAD and model-derived radar images shown throughout this thesis correspond to similar points in the storm's evolution as opposed to an actual time match-up.

The synoptic flow pattern over the Central U.S. was dominated by a strong ridge of high pressure that stretched as far north as southern Manitoba and Saskatchewan. Aside from some weak boundary layer shear and any mesoscale boundaries and heating mechanisms leftover from the previous day's convection, the environment was essentially barotropic on 20 July. Additional convection formed in the region the

following two days before a weak “back-door” cold front from the northeast provided southeast Texas with a brief reprieve from precipitation on 23-24 July before convection began again on 25 July. This barotropic storm is representative of many of the rain events that occurred in Texas during the summer of 2007 when convection did indeed seem to be “gregarious” and “persistent” in the same sense Mapes (1993) generalized for tropical convection and Stensrud (2001) described for the Midwestern floods during the summer of 1993, respectively.

The mean divergence profile generated by MM5 for this barotropic storm compares favorably with the calculated divergence from ADRAD. Figure 12a shows that the model-derived mean divergence profile is generally characterized by convergence at lower and mid-levels and divergence aloft. Divergence is also present near the surface due to outflow from convection. All of these features are present on the divergence profiles calculated using the VAD technique (Mapes and Lin 2005) on radar data from ADRAD shown in Fig. 12b. As expected, the five- and three-range pooled radar data produce smoother divergence profiles in closer agreement with each other and the model than the divergence profile using data from just one 8-km annuli because using one ring does not provide enough data to overcome the effects of outliers in the velocity field. The model-derived level of non-divergence (LND) at 6.8 km is also very close to the 7.0 km LND found in the ADRAD calculations, suggesting that the model is accurately simulating the depth of convection throughout the troposphere. However, the magnitudes of the divergence structures in MM5 are generally greater than the ADRAD divergence profiles by as much as a factor of two. Although some of this difference may

be an artifact of the VAD technique, it is probably more likely that MM5 is overpredicting the magnitudes of storm divergence in general because the observed ADRAD magnitudes are more aligned with those shown in other studies of tropical convection. This problem would need to be resolved before attempting to calculate the magnitudes of diabatic heating in MM5, although the general structure of diabatic heating profiles would most likely be accurate.

Another result shown by this case is that MM5 produces robust stratiform and convective divergence signals when Steiner et al.'s (1995) separation algorithm is applied to MM5 reflectivities. The stratiform profile shown in Fig. 12a consists of moderate magnitudes (~7×10^{-5} s^{-1}) of mid-level convergence peaking at the melting level near 5 km with moderate upper- and lower-level divergence. On the other hand, the convective profile has strong convergence at lower levels peaking around just above 1 km and strong divergence at upper levels. MM5's maximum magnitudes of convergence and divergence are approximately four times greater in the convective regions than the stratiform region, which is in close agreement with the stratiform and convective divergence profiles in Fig. 2 found by Gamache and Houze (1982) within tropical squall lines. However, MM5's divergence magnitudes are greater than Gamache and Houze's by a factor of two in some places, lending credibility to the assertion that MM5 is overpredicting the magnitudes of divergence. Similar to previous studies, the model-derived stratiform LND at 9.0 km is significantly higher than the model-derived convective LND at 5.5 km. Although the placement of the stratiform LND is close to that found by Gamache and Houze, the convective and mean LNDs are 1.5-2 km higher

in the model. One reason for this elevated convective profile might be that the separation algorithm is overclassifying convective rain. The stratiform area fraction generated by the algorithm for this storm in MM5 is 56%, which is much less than the 73% found by Schumacher and Houze (2003) for tropical convection using the TRMM PR. However, increasing the stratiform area fraction to 62% by liberally altering the Steiner et al. (1995) algorithm does not change the height of the LND and only causes small increases in the peaks of the convective divergence profiles. Therefore, MM5 is most likely underpredicting the area experiencing stratiform rain for this storm, which accounts for the slightly lower model-derived mean LND compared to the LND derived using the VAD technique.

Histograms of the model-derived radar reflectivities within the stratiform and convective regions show that applying the Steiner et al. (1995) algorithm to MM5-derived reflectivities captures some of the major microphysical differences between these two rain regimes, but also has some flaws. Figures 13a and 13b display the vertical distribution of reflectivity within stratiform and convective regions, respectively, using a frequency by altitude diagram that will be used throughout this thesis. Each line represents a 10% quantile (from 10-90%) of echo occurrence with height and the plots are cut off at levels that do not have an adequate number of reflectivity values (< 0.5% of the total count).

The stratiform MM5 reflectivities (Fig. 13a) are tightly contoured representing more homogeneous growth processes. Figure 13a also exhibits a prominent bright band at the melting level. The stratiform reflectivity distribution is similar to those for tropical

stratiform rain over the East Atlantic and West Africa shown in Schumacher and Houze (2006). However, the median reflectivity at the surface is about 3-4 dBZ lower than Schumacher and Houze found, implying that evaporative processes are stronger (perhaps overly strong) in stratiform regions simulated by MM5. This issue, along with the overprediction of snow and graupel aloft, also occurs when using the Reisner-2 microphysics scheme (Reisner et al. 1998). Further, the Reisner-2 scheme generates significantly lower stratiform area fractions for tropical convection than the Goddard microphysics scheme (Tao and Simpson 1993).

The convective MM5 reflectivities (Fig. 13b) have a wider contour spacing representing more heterogeneous precipitation growth processes. Convective reflectivities are 15-20 dBZ higher than their stratiform counterparts and have a median of 40 dBZ, which is also 3-4 dBZ greater than the convective reflectivity distribution shown by Schumacher and Houze (2006). In addition, hydrometeors within convective regions do not increase in size from the melting level towards the surface in the MM5 simulation, whereas some increase in size due to collection processes would be expected. A bright band is evident in the convective reflectivity histograms as well, albeit less pronounced than within stratiform regions, suggesting that the Goddard scheme may be biased towards stratiform microphysical processes. Nevertheless, the Goddard scheme is employed for all cases in this research because the Reisner-2 scheme seems to be biased toward convective processes and produces even larger reflectivity values, as will be shown in section 6.

Despite potential microphysical problems with the separated radar reflectivities, the algorithm appears to work from a kinematic perspective because it generates reasonable vertical velocity structures for stratiform and convective regions. As expected, the stratiform region (Fig. 13c) has weak model-derived vertical velocity values with magnitudes within $\pm$ 1 m s^{-1}. The convective region (Fig. 13d) has more variation in vertical velocity with height, with 20-40% of the velocities exceeding 1 m s^{-1} depending on the level evaluated. Downdraft velocities at the 10^{th} percentile and updraft velocities at the 70^{th}, 80^{th}, and 90^{th} percentiles also appear to have two modes near 12 km for the downdrafts and 4 and 8 km for the updrafts. The mode near 4 km indicates that MM5 may be accurately simulating deep convection because Cifelli and Rutledge (1998) showed a prominent peak in diabatic heating near this height for tropical convection near Darwin. These reasonable kinematic structures for stratiform and convective regions, along with the agreement between the model-derived divergence profiles with those calculated from ADRAD using the VAD technique and from other tropical studies, suggest that MM5 can be used to study divergence of barotropic storms outside the Tropics.

b. Strongly baroclinic case: 7-8 April 2007

During late fall, winter, and early spring, Southeast Texas experiences stronger vertical wind shears and horizontal temperature gradients, which is at the opposite end of the baroclinicity spectrum compared to the barotropic conditions discussed in section 4a. The second case study is a strongly baroclinic storm that was predominantly stratiform

with a few embedded elements of elevated convection which occurred on 7-8 April 2007 (Fig. 14a and 14b). MM5 generally matched the timing and placement of precipitation with observations throughout the storm's duration. A large upper-level low in New Mexico, a developing subtropical jet, and a stationary front stretching through New Mexico into the Rio Grande Valley provided a focus for precipitation to develop around 0000 UTC on 7 April. Cloud cover north and west of the analysis domain and a cold front associated with an upper-level trough in the northeast U.S. inhibited daytime warming on 6 April, causing a fairly strong temperature gradient at the surface and 850 hPa. This complex synoptic environment was devoid of any surface-based instability, but area soundings displayed elevated instability above a temperature inversion from 850-650 hPa with strong vertical shear and veering winds with height. As the storm grew rapidly and evolved on 7 April, low-level evaporative cooling from rain further decreased temperatures during the afternoon across southeast Texas, allowing wet snow and sleet to fall in some areas in the northern half of the analysis domain, making it the first time accumulating snow has ever been recorded in southeast Texas during April.[2]

Figure 15 shows that the model-derived mean divergence profile for the strongly baroclinic case closely matches ADRAD's and is a stark contrast to the barotropic mean divergence profile (cf. Fig. 12a). MM5's mean divergence profile (Fig. 15a) contains convergence associated with stratiform rain from 1.1-4.2 km with weak divergence below and above, similar to the divergence observed by ADRAD (Fig. 15b), except

[2]According to a Public Information Statement issued by the National Weather Service office in League City, TX on 9 April 2007 (http://www.srh.noaa.gov/hgx/climate/reviews/040907pns.txt)

above 8.5 km where ADRAD indicates a convergent layer. Only 1.6 percent of the near-surface MM5 reflectivities were classified as convective, and the convection in this storm was elevated as opposed to being surface-based as in the barotropic case. As a result, the convective LND (5.8 km) is higher than the stratiform LND (4.1 km) in Fig. 15a, implying that this type of stratiform rain is very different from that which is directly caused by deep, surface-based convection. The model-derived convective divergence profile has larger magnitudes than the barotropic case, possibly suggesting that the higher degree of baroclinicity causes higher values for divergence in convective regions, particularly at upper levels. On the other hand, the model-derived stratiform convergence peak is of the same magnitude as that in the barotropic case ($\sim 7 \times 10^{-5}$ s^{-1}), albeit at a lower level.

Reflectivity distributions for this storm (Fig. 16a-b) are different than in the barotropic case, particularly within the stratiform region, which accounts for most of the rain in this storm. The stratiform reflectivity distribution (Fig. 16a) has a median surface value of 25 dBZ and is almost trimodal with height, with peaks occurring 5 km, 2 km and at the surface. The upper peak is most likely due to stratiform rain from the elevated convection forming aloft or a small amount of convection being misclassified as stratiform. The lower two peaks are caused by complex phase changes with height. A strong temperature inversion aloft, evident in area soundings on 7-8 April, causes two melting levels located between 2.5-5 km and below 1 km, with hydrometeors potentially attempting to refreeze between 0.5-2.5 km depending on the depth of the melting layers. Variations in the strength of the temperature inversion occur across the analysis domain

over time, with the Lake Charles, LA and Corpus Christi, TX soundings having more pronounced melting layers and a higher upper melting level than in Shreveport, LA and Fort Worth, TX. Therefore, the trimodal stratiform reflectivity distribution is probably an artifact of these inversion variations across the analysis domain.

The convective reflectivity distribution (Fig. 16b) has a higher median surface reflectivity of 37 dBZ with less contour spread than in the stratiform region. About half of the isolated cores classified as convective exhibit a distinct bright band located near 3 km. Both the stratiform and convective profiles have similar structures above 5 km with larger reflectivity magnitudes for the latter, supporting the claim that some of the stratiform distribution's upper mode at 5 km is due to misclassification of elevated convection as stratiform rain.

The stratiform vertical velocity distribution with height is similar to the barotropic case, but the convective profile is much different because the convection in this strongly baroclinic case is of an elevated, slantwise nature. Vertical velocities within the stratiform regions (Fig. 15c) change little with height, have magnitudes less than 1 ms^{-1} at all levels, and have a positive median. They differ from the barotropic case in that they have a small increase in velocities at mid-levels due to stratiform rain occurring from elevated convection near 5 km. The increase in vertical velocities at midlevels is much more pronounced within the convective region (Fig. 15d), with almost 30% of the convective vertical velocities exceeding 1 m s^{-1} at 5 km. Aside from this difference, the distribution of convective vertical velocities is similar to those in the more dominant stratiform region. These results combined with the high stratiform area fraction of 98.4%

suggest that Steiner et al.'s (1995) separation algorithm is accurate for systems with large amounts of stratiform rain and that the methodologies employed in this thesis may also be applied to systems with high degrees of baroclinicity and elevated convection.

c. Weakly baroclinic cases: 13-14 and 14-15 March 2007

Southeast Texas regularly experiences barotropic conditions in summer and strongly baroclinic systems from the midlatitudes in winter, early spring, and late autumn. However, many of the precipitating systems the region commonly experiences during spring and autumn and sporadically during summer and winter are weakly baroclinic. These storms have significantly weaker temperature gradients and wind shears than typically found in stronger winter storms, but have too much synoptic forcing to be classified as barotropic.

Two weakly baroclinic MCSs occurred in succession on 13-15 March 2007 as a closed low pressure system stretching through the depth of the troposphere slowly progressed eastward across Texas. This low pressure system originated from a shortwave trough that intensified as it crossed the Rocky Mountains on 10-11 March before becoming cutoff in west Texas and slightly retrograding into southeast New Mexico on 12 March. A kicker shortwave weakened a ridge of high pressure that had briefly built in over the coast of California and eventually forced the closed low pressure system to begin a slow eastward progression across Texas during the afternoon on 13 March. These complex dynamic elements created an environment with moderate speed and directional vertical wind shears that fall between those found in the barotropic and

strongly baroclinic cases. Area soundings also displayed a moderate amount of instability above a capped planetary boundary layer. A weak temperature gradient was present because temperatures were unable to rebound quickly in parts of west Texas from a weak cold front that passed through on 11-12 March with an associated large LLTS-MCS.

Convection began around 1500 UTC on 13 March along a line in south Texas extending from Corpus Christi to Laredo. The line quickly moved northeast and increased in areal coverage throughout the afternoon to form a large disorganized MCS with numerous pockets of intense convective cores. By 2300 UTC, the convection began to align itself in a series of small lines on the south and east sides of the MCS where an outflow boundary that was left behind by the original convection was initiating new convective cells and reinforcing existing ones (Fig. 17a). The MM5 model run for this storm is delayed by about 3 hours but simulates the system fairly well by placing most convection on the southern and eastern sides of the MCS with convective pockets embedded within stratiform rain elsewhere, although it fails to develop convection in northeast Texas outside the analysis domain (Fig. 17b). The same model run extended further in time is used to simulate the additional convection that began to develop the next morning in two places around 1400 UTC on 14 March: in central Texas in the vicinity of the closed low pressure system aloft and along the same outflow boundary responsible for enhancing convection the previous evening, now centered near Matagorda Bay. The convection in central Texas increased in size and appears to have developed a small MCV coinciding with the closed low pressure system by 2000 UTC

as it propagated southeast during the afternoon and evening hours. MM5 initiates the convection in central Texas that accounts for almost all of the convection that occurs in the analysis domain, simulating a smaller MCS with a greater proportion of convective rain than occurred on the previous day (Fig. 17c and 17d). The model fails to develop much convection along the outflow boundary, which accounts for little of the convection that occurs in the analysis domain because most of it remains south of D3. This inability to develop convection along the outflow boundary may be caused by problems with grid interactions between D2 and D3 because the outflow boundary is situated close to the analysis domain's southern boundary.

As in the previous case studies, MM5 generates realistic mean divergence profiles for these two weakly baroclinic cases that are comparable to those calculated from ADRAD observations. The structures of the model-derived divergence for both 13-14 March (Fig. 18a) and 14-15 March 2007 (Fig. 18c) exhibit convergence at lower and mid-levels sandwiched between divergence near the surface and at upper-levels, in close agreement with the observed divergence profiles shown in Figs. 18b and 18d, respectively. The model-derived mean LNDs for both cases are only 0.2-0.3 km below those observed by ADRAD, with the 13-14 March storm having an LND (6.4 km in MM5; 6.6 km in observations) that is over 1.5 km higher than for 14-15 March case (4.7 km in MM5; 5.0 km in observations). The convective and stratiform LNDs are also elevated in the 13-14 March case, which has a thicker layer of stratiform convergence from 1.5-8.1 km compared to the following day's storm, which only extends from 3.0-7.4 km. MM5 reflectivity histograms shown in Fig. 19 indicate that convection extends

up to heights that are 1 km greater on 13-14 March than on the following day when the LND is over 1.5 km lower. Coincidentally, soundings from Fort Worth, Texas display a 1 km decrease in the tropopause height from 0000 UTC 14 March to 0000 UTC 15 March associated with the increased baroclinicity from the passage of the upper-level low pressure system during the day on 14 March. The lowered tropopause that occurred with the passage of the baroclinic wave caused a less-elevated divergence profile on 14 March because it prevented convective cells from reaching as high as on 13 March.

Another observation from these two weakly baroclinic storms, which is supported by other cases presented in this thesis, is that areas containing larger amounts of deep convection appear to have mean divergence profiles with greater magnitudes. The magnitudes of the model-derived divergence profiles are slightly larger for the 14-15 March storm (Fig. 18c) when the stratiform area fraction is lower (51.8%) than on the previous day (Fig. 18a, 57.2%). Although this may be partly due to the greater synoptic forcing on 14-15 March, the higher percentage of deep convection for this storm may have also caused the higher magnitudes of divergence because convective regions modeled in this study have peak magnitudes of low-level convergence and upper-level divergence that are approximately four to five times larger than that of stratiform regions. In addition, the 14-15 March observed divergence profiles (Fig. 18d) have greater magnitudes than on the previous day (Fig. 18b). Some of this difference is caused by ADRAD oversampling stratiform regions on 13-14 March and convective regions on 14-15 March relative to the rest of southeast Texas. Most of the convection on 13-14 March occurred south of ADRAD's analysis range (but still was captured

within MM5's analysis domain), whereas most of the convection that developed on 14-15 March formed within ADRAD's analysis range, likely causing stratiform rain regions to be undersampled. Nevertheless, ADRAD's sampling problems on these two days supports the argument that higher convective area fractions can cause greater magnitudes of divergence, which is also affirmed by the mean divergence profiles generated in MM5 for these two storms and others presented in this thesis.

Vertical distributions of the radar reflectivity and vertical velocity for both weakly baroclinic storms are presented for consistency. MM5 reflectivities within the stratiform regions on 13-14 March (Fig. 19a) and 14-15 March (Fig. 19c) are ~1 km lower than their convective counterparts (Figs. 19b and 19d, respectively). In addition, MM5 reflectivity values within the stratiform region on 13-14 March are about 4 dBZ higher than on 14-15 March, although the reflectivities in the convective regions are only about 1 dBZ higher. Other than the higher surface reflectivities in the stratiform region on 13-14 March, lower surface reflectivities within the convective regions, and a lower bright band (~3-3.5 km), the reflectivity structures for these weakly baroclinic storms are similar to those in the barotropic case (Figs. 13a and 13b).

As expected, the vertical velocity histograms display smaller magnitudes (<1 m s^{-1}) within the stratiform regions for both storms. However, on 13-14 March (Fig. 20a) the presence of a prominent downdraft that peaks near 3 km (just below the melting level) and a weaker updraft signal that peaks near 8 km, causes about 10% of the vertical velocity values to exceed the 1 m s^{-1} threshold at these heights. The 14-15 March storm (Fig. 20c) contains less pronounced low-level downdrafts and upper-level updrafts in the

stratiform region. Interestingly, the barotropic storm's stratiform vertical velocity structure (Fig. 13c) does not display a prominent downdraft. The stratiform rain on this day was caused more by convection dying in place than having hydrometeors advected downshear from the convective regions and then descending in a strong, organized rear inflow jet to form the stratiform region as is more common in LLTS-MCSs. Vertical velocities within the convective region on 13-14 March (Fig. 20b) are also larger and more elevated than on 14-15 March (Fig. 20d), implying larger values of diabatic heating extending through a greater vertical extent of the troposphere on 13-14 March. Although the barotropic case has larger vertical velocities above 11 km within convective regions, the 13-14 March case has larger magnitudes elsewhere with a higher peak in convective updrafts near 5 km. Therefore, although lower tropopause heights in the weakly baroclinic cases prevent convection from reaching as high as in the barotropic case, the magnitudes of the convective updrafts and downdrafts in the 13-14 March storm are generally larger below this level and produce a stratiform region with stronger downdrafts than occur in the barotropic case.

Finally, although the convection on 14-15 March is largely forced by the low pressure system that was propagating into the region, the 13-14 March storms may have had a small thermodynamic upscale feedback that played a role in enhancing convection the next day over southeast Texas. The convection in the 13-14 March weakly baroclinic storm is not as deep as the convection in the barotropic case, but its LND is only 0.4 km lower in both the model and observations, indicating that some weakly baroclinic systems in the subtropics may have heating structures that are nearly as elevated as those

occurring in more barotropic, tropical environments with deep convection. Interestingly, no additional convection forms after the passage of the low pressure system in the wake of the 14-15 March storm, which has a lower stratiform rain fraction and leaves behind a divergence profile that is less elevated than the previous day. Previous studies have shown how stratiform rain in the Tropics can produce slow-moving gravity waves that heat the upper troposphere while cooling the lower troposphere, thus destabilizing the environment and encouraging additional convection to form (Mapes 1993, Mapes and Houze 1995). Circumstantially, some subtropical weakly baroclinic systems with deep convection and elevated heating profiles more characteristic of the Tropics (like the one on 13-14 March) may also play a small role in driving additional convection as long as synoptic forcing mechanisms do not overwhelm diabatic convective feedbacks. Although it is likely that the higher degree of synoptic forcing present in weakly baroclinic storms prevents these feedbacks from spreading as far upscale temporally and spatially as barotropic storms, additional research needs to be performed to quantify the diabatic effects of convection within numerically-quantified baroclinic regimes and whether certain storm types have a greater diabatic feedback than others.

5. MODEL COMPARISONS OF COMMON STORM TYPES

a. Upper-level disturbances

Investigating upper-level disturbances is critical to understanding how storm divergence varies in the subtropics because they are the only storm type that is prevalent in a wide range of baroclinic environments (including barotropic). Baroclinic storms caused exclusively by upper-level disturbances commonly have relatively small temperature gradients, but have moderate to strong vertical wind shears depending on the strength of the longwave or shortwave trough, jet streak, and/or closed low that is causing them. Barotropic upper-level disturbances tend to be more vertically stacked and have significantly lower background vertical wind shears than their baroclinic counterparts (hurricanes have large diabatically-driven wind shears within them that are separate from their background environment). Additionally, barotropic upper-level disturbances in the subtropics tend to be separated from synoptic features and generally appear as a westward-propagating wave feature from the Gulf of Mexico, an eastward-propagating wave feature cutoff from the main synoptic flow, or a mesoscale stationary or meandering disturbance formed from previous regions of convection.

Three additional upper-level disturbances have been simulated in MM5 to supplement the 13-14 March 2007 weakly baroclinic and 7 April 2007 strongly baroclinic cases presented in the previous section. The barotropic upper-level disturbance consisted of air mass thunderstorms that rotated around a 500-700 hPa closed low pressure system located in central Texas during the day on 4 July 2006. The model simulation captures the organizational mode of convection rotating around the

low with stratiform rain forming from old convection, but is not able to pinpoint the exact timing and locations of cells due to their random, chaotic nature (Figs. 21a and 21b). Area soundings also indicate that the environment was more tropical in nature with weak shear, deep moisture and precipitable water values above 60 mm. The initial mesoscale low pressure system originated on 30 June-1 July from a weak longwave trough, part of which cut-off from the synoptic-scale flow and formed the upper-level low in question. Persistent convection over the next three days in the region may have helped maintain this low, which meandered around the Hill Country in central Texas before beginning a slow eastward progression on 4 July, eventually moving out of Texas on 6 July. Numerous air mass thunderstorms also formed on 5 July in southeast Texas near the propagating low, which were likely driven in part by diabatic convective feedbacks.

This barotropic case is contrasted with two baroclinic upper-level disturbances whose synoptic forcing appears to overwhelm diabatic feedbacks. The weakly baroclinic upper-level disturbance formed in far southern New Mexico and west Texas near Big Bend during the afternoon of 25 March 2007 downstream of a trough cutoff from the main jet stream. As this midlevel trough became more negatively-tilted and the subtropical jet moved into the region from the southwest on 26 March, the storm matured into a large blobular MCS containing stratiform rain with regions of embedded convection, which MM5 simulates fairly well (Figs. 21c and 21d). The storm slowly weakened and decreased in area into the evening and overnight hours of 27 March before moving out of southeast Texas by 0900 UTC. The strongly baroclinic upper-level

disturbance formed on 25 February 2006 within the left-exit region of a stronger subtropical jet downstream of a midlevel shortwave trough. This system is also a well-modeled stratiform MCS (Figs. 21e and 21f), but with less embedded convection than the weakly baroclinic case. Area soundings indicate that temperatures were colder and that the vertical wind shear was stronger for this storm than the weakly baroclinic case, although the temperature gradient is still small. Even though a cold front was quickly moving in from Kansas and Oklahoma and a stationary front was situated in the Gulf, the precipitation formed between these far removed frontal zones in response to the upper-level disturbances and moved east during the afternoon. The temperature gradient within the domain was small because the cold front did not move through until early on 26 February after the convection passes.

Many of the same variations with increasing degrees of baroclinicity present in the divergence profiles presented in section 4 are evident in the model-derived structures these upper-level disturbance storms caused. The barotropic case (Fig. 22a) generates the most elevated divergence profile with significantly higher mean, stratiform, and convective LNDs than the weakly baroclinic case (Fig. 22b), which in turn has higher LNDs than the strongly baroclinic case (Fig. 22c). Convective regions in both the barotropic and weakly baroclinic cases have a secondary peak in convergence near their melting levels of 5 km and 4 km, respectively, likely due to misclassification of some stratiform echoes. As a result, the convective profiles for these two storms have higher LNDs than they should, but this problem does not affect the mean divergence profile because correctly classifying these echoes as stratiform would only change the separated

divergence profiles. In agreement with the cases shown in the previous section, the mean magnitudes of divergence at upper levels are greatest for the barotropic case, which has the largest amount of deep convection, and decreases with increasing baroclinicity. However, the magnitudes of low-level convergence in the barotropic and strongly baroclinic cases are similar and are smallest in the weakly baroclinic case, suggesting that greater variation in divergence at low levels is not necessarily attributable to baroclinicity and the amount of deep convection.

Stratiform area fractions are once again highest in the strongly baroclinic case (79.5%) and lowest in the barotropic case (59.3%) with the weakly baroclinic case falling in between (72.2%). Distinct stratiform profiles with pronounced convergence at mid-levels and divergence near the surface and at upper levels are evident in the weakly baroclinic and barotropic cases, the latter of which has larger magnitudes and a thicker region of mid-level convergence because stratiform rain is arising from deeper, more tropical-like convection. Although stratiform rain results from relatively deep convection in the weakly baroclinic case as well, the tropopause is lower and prevents convection from penetrating as high into the atmosphere which generates divergence profiles that are more compressed but similar in structure to the barotropic case. The strongly baroclinic storm's stratiform divergence profile is much less pronounced, although it does exhibit a small convergent peak near the melting level at 4 km. As expected, no additional convection forms after the passage of the low pressure disturbances in the weakly baroclinic and strongly baroclinic cases, indicating that the synoptic forcing is overwhelming any potential diabatic feedbacks. However, convection from the

barotropic case appears to help drive additional convection in the region for the next few days because there are no synoptic forcing mechanisms to overwhelm the diabatic convective feedbacks. Although the evidence is circumstantial, the significant elevation in the barotropic case's model-derived mean divergence profile coupled with a very deep layer of mid-level convergence within stratiform rain suggests that subtropical deep convection in barotropic environments behaves like tropical deep convection. Likewise, a fraction of weakly baroclinic upper-level disturbances like the 13-14 March 2007 case presented in section 4c may also exhibit these features, although their diabatic convective feedbacks may not be as far reaching as in more barotropic environments.

b. Frontal leading line-trailing stratiform MCSs

Frontal storm systems by definition cannot be barotropic, but they still have a wide variety of baroclinicities associated with them depending on the front's temperature gradient and the trough's vertical wind shear. One common orientation of convection in cold and stationary frontal MCSs is that of a leading line of convection followed by a trailing stratiform region, commonly referred to as a LLTS-MCS. Investigating frontal LLTS-MCSs is beneficial because identifying stratiform and convective rain regions is relatively simple in these storms, thereby providing a check on the procedures used to separate stratiform rain from convection. Similarly, model-derived divergence structures within convective and stratiform regions of LLTS-MCSs may also be compared to other tropical and midlatitude studies of these systems.

Two baroclinic LLTS-MCSs with disparate degrees of environmental baroclinicity were successfully simulated in MM5 for this purpose. The weakly baroclinic LLTS-MCS began as a cluster of storms that formed south of a dissipating surface front along the southwest Oklahoma-Texas border around 2200 UTC 17 June 2006. The weakly baroclinic LLTS-MCS evolved into a bowed line of convection with a mature stratiform region as it propagated southeast into a warmer, more unstable environment away from the surface front overnight on 18 June 2006 (Figs. 23a and 23b). Although the temperature gradients were small, this storm is considered to be weakly baroclinic because moderate wind shear (both in magnitude and direction) was present due to a mid-to-upper-level trough that extended into central Texas from Canada. The strongly baroclinic LLTS-MCS was an intense, frontal line of convection that had a fairly robust stratiform rain region throughout its duration (Figs. 23c and 23d). Unlike its weakly baroclinic counterpart, this storm occurred during daytime hours and moved *along* a cold front with a very strong temperature gradient downstream of a strong midlevel trough. Convection began to form around 0500 UTC on 31 October 2005 near the southwest Kansas-Oklahoma border along a warm front and cold front extending from the surface low located there. The cold frontal convection evolved into a squall line and moved southeast during the day. By 2030 UTC, as the squall line was passing through College Station, a large stratiform rain region had formed and some convection began to develop ahead of the convective line, both of which are captured by the model output shown in Fig. 23d.

Consistent with the storms shown thus far, the weakly baroclinic divergence profile (Fig. 24a) has a mean LND that is about 1 km higher than its strongly baroclinic counterpart (Fig. 24b). Both storms have similar magnitudes of low-level convergence within convective regions, but the strongly baroclinic LLTS-MCS contains larger magnitudes of upper-level divergence that are probably caused by the greater shear and synoptic forcing present along the cold front. However, divergence aloft extends higher in the troposphere in the weakly baroclinic LLTS-MCS because its tropopause is higher, which allows convection to penetrate a few kilometers higher than in the strongly baroclinic storm. A double peak in the low-level convergence profile is also present within the convective region of each storm, but the stratiform regions display maxima in convergence that are much higher than the convective convergent regions suggesting that the double peak in convergence is not necessarily due to misclassification of stratiform rain as convective. Within the stratiform rain region, the weakly baroclinic LLTS-MCS has a thicker layer of mid-level convergence along with greater magnitudes of divergence aloft and mid-level convergence than in the strongly baroclinic storm where convection does not extend as deep into the troposphere.

Although these frontal LLTS-MCSs exhibit some of the same trends as other storms that have been presented, they differ by having much lower stratiform area fractions and larger magnitudes of mean convergence and divergence than other types of storms with similar baroclinicities. MM5 generates a stratiform area fraction of 41.5% for the weakly baroclinic LLTS-MCS and 52.9% for the strongly baroclinic storm, both of which are lower than either of the barotropic storms shown and for other storm types

with similar degrees of baroclinicity. Although MM5 is probably overestimating the amount of convection in these cases because the separation algorithm classifies some of the trailing stratiform region as convective, the relative decrease in stratiform area fraction compared with other storm types remains plausible. Stratiform rain within LLTS-MCSs arises from deep convection, but it is inherently different from stratiform rain within other storm types in that it is caused primarily by wind shear that advects hydrometeors directly behind the leading convective line instead of coming from elevated convection, decaying deep convection, or a combination of these factors thus limiting its hydrometer source. In addition, stratiform rain generally covers larger areas in more strongly baroclinic LLTS-MCSs, which have stronger wind shears that advect hydrometeors further behind convection.

Although LLTS-MCS stratiform area fractions are lower, their magnitudes of mid-level convergence and upper-level divergence are larger in MM5, most likely because of the amount of deep convection relative to other storm types and their strong ascending front-to-rear and descending rear inflow jets induced by the storm itself. This is particularly true for the weakly baroclinic storm whose convergence at mid-levels within the stratiform region is greater than its low-level convergence in the convective region. In addition, the weakly baroclinic storm has pronounced low-level downdrafts and upper-level updrafts within the stratiform region, with vertical velocities exceeding 1 m s^{-1} for over 20% of the grid points. In contrast, the strongly baroclinic storm has a distinct downdraft signature, with vertical velocities exceeding 1 m s^{-1} for over 10% of the data (not shown). Diabatic convective feedbacks on the large-scale circulation occur

in the weakly baroclinic LLTS-MCS because it leaves behind a mesoscale low pressure system in its wake that splits apart from the synoptic flow. This slowly retrograding mesoscale low helped drive convection in the region for the next few days even though the longwave trough responsible for developing the original frontal LLTS-MCS propagated away from the region. On the other hand, no additional convection forms after the passage of the strong cold front and trough associated with the strongly baroclinic LLTS-MCS because its synoptic forcing overwhelms any diabatic feedbacks present. Regardless, large magnitudes of mid-level convergence and upper-level divergence within concentrated stratiform rain regions may have important dynamic implications on the large-scale circulation that need further investigation.

c. Other frontal storms

Although the diabatic feedbacks that cause persistent convection are generally overwhelmed by synoptic forcing in most frontal storms, studying these systems is vital in deciphering how storm divergence varies in the subtropics because their diabatic feedbacks can affect frontogenesis and the movement and intensity of frontal storm systems (Bryan and Fritsch 2000, Chang et al. 2002). Stationary and cold fronts also cause about half of the precipitating systems in southeast Texas (Brugman 2007; Table 1), so two of these common storm systems are simulated in MM5 to help paint a more complete picture of how storm divergence changes with baroclinicity. The weakly baroclinic frontal storm developed on 26 November 2005 as a shortwave trough moved in and enhanced lift along a stationary front situated near the Gulf Coast. Temperature

gradients and wind shears associated with this front were not exceptionally large, but the dew points were 5-10^{o}C higher south of it. This front originated from a cold front that moved into the region on 25 November before becoming stationary and propagating northeast as a weak warm front with the disorganized MCS that developed the following day. MM5 initiates convection correctly in south Texas and develops a disorganized MCS containing a large region of stratiform rain with numerous embedded convective cells that generally matches the observations (Figs. 25a and 25b).

This storm is compared to the strongly baroclinic frontal system on 13-14 January 2007 that contains much larger temperature gradients and wind shear associated with a very slow-moving surface cold front. The cold front gradually moved through on 13 January before becoming stationary across the southeastern side of the analysis domain for much of 14 January before a longwave trough forced the front to propagate east the following day. Throughout the MM5 simulation, strong convective cells continually developed along the front and ahead of it in the warm sector where temperatures and dew points were around 20^{o}C. Large areas of stratiform rain formed primarily from decaying convection and convective cells that moved into stable air in the cold sector of the baroclinic zone that synoptically forced convection to weaken. Although the model overpredicts some of the rainfall in the cold sector, it generally simulates this linear storm system with a large amount of stratiform rain well by slowly propagating the system eastward with the front while individual convective cells that developed along and ahead of the front moved northeast (Figs. 25c and 25d).

Like the cases shown previously, the mean divergence profile contains larger magnitudes and the LND is more elevated for the weakly baroclinic frontal storm (Fig. 26a). On the other hand, the strongly baroclinic storm (Fig. 26b) has larger magnitudes of convergence at the surface with upper-level divergence that extends through a greater depth of the troposphere, although with much lower magnitudes than in the weakly baroclinic case. The convective profiles for both cases have some structural similarities, but the LND is about 1 km higher and there is greater upper-level divergence above 6 km associated with more deep convection for the weakly baroclinic storm. Likewise, the magnitudes of low-level convergence and upper-level divergence within the convective region are larger for the weakly baroclinic storm. This result combined with other cases indicates that convective regions have variable magnitudes from case to case that are not necessarily closely related to baroclinicity. However, the LND and magnitudes of divergence in the upper troposphere with deep convection appear to be greater for storms with lower degrees of baroclinicity.

In agreement with the other storm types shown, the weakly baroclinic storm has a lower stratiform area fraction (64.9%) than its strongly baroclinic counterpart (76.9%), which has lower magnitudes of mid-level convergence. Stratiform rain in the weakly baroclinic case has a traditional mean divergence structure with convergence at mid-levels sandwiched between divergence near the surface and at upper-levels. The stratiform rain in the strongly baroclinic storm, however, has strong convergence at the surface that becomes divergent at 1.4 km and peaks near 2.8 km before exhibiting the more typical structures of mid-level convergence and upper-level divergence. This

discrepancy is due to the Steiner et al. (1995) algorithm classifying developing convection as stratiform, a problem that occurs in all of the modeled storms but usually is not prominent enough to show up in the stratiform divergence structure. Aside from this strongly baroclinic frontal case, the only other exceptions are the LLTS-MCS cases which have similar shallow convective divergence structures in their stratiform divergence profiles (Figs. 24a and 24b), albeit with lower magnitudes of surface convergence.

Although neither of these frontal storms have diabatic feedbacks that alter the large-scale circulation in the same sense that many barotropic and some weakly baroclinic storms do in the subtropics, both appear to have diabatic feedbacks that may cause the existing fronts to propagate discretely as Bryan and Fritsch (2000) have shown. Although investigating this further is outside the scope of this thesis, it is worth mentioning that the stationary front in the 26 November 2005 storm only began to propagate northeast as a warm front *after* convection had formed and propagated with it. Therefore, although it is hard to discern whether diabatic processes within the MCS caused the front to discretely propagate with it or if the front itself caused the MCS to move, it is likely that both the MCS and front interacted with one another. Similarly, the cold front that caused precipitation on 13-14 January 2007 also appears to propagate discretely and perhaps may also have been affected by diabatic processes. Although the magnitudes of mid-level convergence are very small within the stratiform region, this convergence stretches through an unusually large depth of the troposphere for a strongly baroclinic system up to a stratiform LND of 8.2 km. In conjunction with deep Pacific

moisture and upper-level jet streaks, the weak elevated heating associated with stratiform rain on 13-14 January may have helped enhance convection aloft at the beginning of the ensuing winter storm that produced large amounts of freezing rain, sleet, and snow across the region on 15-17 January. Although this diabatic contribution is probably difficult to quantify and secondary to synoptic forcing mechanisms, future researchers and forecasters may benefit from investigating whether previous convection can help initiate and enhance convection in winter storms.

d. Importance of deep convection on stratiform mid-level convergence

Although the degree of baroclinicity has a large influence on the depth and magnitude of mid-level convergence within stratiform rain, a storm with stronger baroclinicity but more deep convection than one with weaker degrees of baroclinicity may have more robust mid-level convergence structures. Significant variations in divergence profiles can also occur within the same storm system over time if the amount of deep convection changes or the mode of convection switches from elevated to deep and surface-based or vice-versa. One final weakly baroclinic frontal storm system that occurred on 28 March 2006 is separated into two evolutionary stages to illustrate these differences. Most of the stratiform rain during the evening and overnight hours from 0100-1000 UTC on 28 March was caused by elevated convection due to gentle uplift along a stationary front within the analysis domain. Deep convective activity increased toward the end of this period as a weak shortwave trough moved in from the west, forming stratiform rain directly from deep convection as opposed to weak elevated

frontal convection. The line of precipitation stopped moving north and began to propagate south away from the front around 1000 UTC, with the majority of convective cells aligning along the southern end of the system. This storm evolved rapidly into a LLTS-MCS that was much less severe than the two presented in section 5b as it moved south throughout the analysis domain, eventually moving south of it by 2100 UTC. MM5 simulates this frontal system well over time and includes the noticeable shift from more elevated convection (Figs. 27a and 27b) to deep convection (Figs. 27c and 27d) from 0900-1100 UTC.

Histograms of the MM5 reflectivities and vertical velocities for both time periods clearly display the transition from elevated to deep convection from a microphysical and kinematic standpoint. Both the stratiform (Fig. 28a) and convective (Fig. 28b) MM5 reflectivities during the first part of the storm have a reflectivity peak near 4.5 km with a general decrease in reflectivity up to echo tops past 8 km and 10 km for the stratiform and convective regions, respectively. During the deep convective period of the storm, however, the stratiform (Fig. 28c) and convective (Fig. 28d) precipitation-sized hydrometeors reach about 2 km higher in the troposphere, with increased near surface reflectivities and distinct bright band peaks near the melting level just above 3 km. These changes are also evident in the vertical velocity distributions in the convective regions for the elevated (Fig. 29b) and deep convective (Fig. 29d) periods of the storm. During the time with elevated convection, the magnitudes of vertical velocity are generally below 1 ms^{-1} except for 10-20% of the grid points with higher updraft velocities from 2-7 km. After the transition to deep convection, more pronounced

updrafts and downdrafts are evident through a much greater depth of the troposphere. Little change occurs between the stratiform regions before (Fig. 29a) and after (Fig. 29c) the transition to deep convection, with both having very homogeneous vertical velocity structures with height and containing magnitudes below 1 m s^{-1}. In addition, the stratiform area fraction decreases from the elevated convective stage to the deep convective stage (i.e., 77.0% to 72.4%), suggesting that the changes evident in the divergence profiles are caused by a switch in the mode of convection instead of lower stratiform area fractions.

Large changes in the divergence profiles are present between the two storm stages (Figs. 30a and 30b). The surge in deep convection increases the height and magnitude of low-level convergence and upper-level divergence in the mean profile. The convective divergence profile in particular shows a large increase in divergence above 7 km. Consequently, mid-level convergence increases within the stratiform region because of the larger amount of deep convection during the second stage of the storm, causing the stratiform divergence profile in Fig. 30b to have structures more typical of some of the other weakly baroclinic storms, with magnitudes of mean divergence less than 1.0 x 10^{-4} s^{-1} and a LND at 5.9 km. The divergence structures during the first stage of the storm are more comparable to those in the strongly baroclinic frontal case (Fig. 26b), which also includes a shallow convective profile in the lower 3 km of the stratiform profile and very low magnitudes of mid-level convergence and upper-level divergence. One additional similarity is that the elevated convective portion of the storm has a stratiform divergence profile whose LND is significantly elevated at 8.9 km despite

having small magnitudes. This may have caused some diabatic feedbacks that combined with additional forcing from the weak shortwave that moved in to cause the transition towards deep convection over the ensuing daytime hours. The LLTS-MCS that formed as a result propagated the weakening stationary front toward the Gulf Coast, which provided a focus for additional convection to form during the afternoon of 29 March when yet another weak shortwave passed through the region. Although investigating the diabatic contribution is beyond the scope of this thesis, this is yet another example of why some attempt should be made to quantify the diabatic convective feedbacks between subtropical storms and the large-scale circulation.

6. MM5 SENSITIVITY TESTS

Many combinations of cumulus parameterization (CP) and microphysics parameterization (MP) schemes were used to model different storms in MM5 across a wide range of baroclinicities. However, after simulating numerous cases it became apparent that the Grell CP (Grell 1993) along with the Goddard (Tao and Simpson 1993) and Reisner-2 (Reisner et al. 1998) MP schemes generally produced the most realistic simulations of radar reflectivity, vertical velocity, and divergence. Therefore, four combinations of MP and CP schemes are used in modeling each storm in MM5 following the model description given in section 3: Grell CP on D1 only with Goddard MP (hereafter referred to as GRLNC2gd), Grell CP on D1 only with Reisner-2 MP (GRLNC2r2), Grell CP on D1 and D2 with Goddard MP (GRLgd), and Grell CP on D1 and D2 with Reisner-2 MP (GRLr2).

Large differences in the vertical structure and magnitude of radar reflectivity are apparent between model runs using the Reisner-2 and Goddard MP schemes. The vertical distribution of mean radar reflectivity (i.e., not separated into convective and stratiform components) from the four different runs of the 26 November 2005 weakly baroclinic frontal storm system is shown in Fig. 31 to illustrate general differences in the reflectivity structures that are consistent across most of the cases investigated in this thesis. The GRLNC2gd run (Fig. 31a), which is the parameterization set employed for all storms presented in this thesis, contains a pronounced bright band above the melting level at 3 km with most echo tops not extending as deep into the troposphere as the GRLNC2r2 run (Fig. 31b). The GRLNC2r2 run does not exhibit as pronounced a bright

band for the majority of the data and generates much larger reflectivity values from the melting level downward to the surface compared to the GRLNC2gd run. The GRLNC2gd run, for example, has a median surface reflectivity of 29 dBZ versus the 36.5 dBZ median value in the GRLNC2r2 run.

Larger model-derived radar reflectivities occur above the bright band in the GRLNC2gd run, suggesting that the Goddard MP produces more and/or larger snow and graupel aloft than the Reisner-2 MP. Both of these schemes appear to overpredict the amount of snow (~< 35 dBZ) and graupel (~≥35 dBZ) aloft because Schumacher and Houze (2006) and others typically have shown stratiform and convective reflectivity structures that decrease more rapidly with height above the 0^{o}C level. Additionally, Garvert et al. (2005) showed the Reisner-2 MP in MM5 overpredicts rainfall on the lee slopes and certain areas along the foothills of the Cascade Mountains because it generates too much snow aloft and misclassifies some graupel as snow. The Goddard scheme's enhanced production of snow and graupel aloft suggests that this is a more widespread problem in MM5 for MP schemes that incorporate the mixed phase processes vital to accurately simulating and quantifying diabatic processes.

The GRLgd (Fig. 31c) and GRLr2 (Fig. 31d) model runs, which employ the Grell CP on D1 and D2, display many of these same characteristics, although the majority of echoes extend through about a 1 km lower depth of the troposphere than their MM5 counterparts that explicitly resolve convection on D2. Reflectivity values are also slightly reduced above 8 km compared to the model runs that do not employ the Grell CP on D2, especially for the GRLgd run. The decrease in the height of most echo

tops and reduction of reflectivity values in the upper troposphere are supported by histograms of vertical velocity (not shown), which contain slightly lower magnitudes in the upper troposphere in the model runs that employ the Grell CP on D2. In addition, updrafts are generally larger in the lower and mid-troposphere for the Reisner-2 model runs, although updrafts and downdrafts are normally greater in the upper troposphere for the Goddard runs. Although there are some exceptions, these kinematic generalizations are supported by the larger reflectivities below the bright band for the Reisner-2 runs and in the upper troposphere for the Goddard runs that appear to have more graupel formation.

After performing the Steiner et al. (1995) stratiform-convective separation for many storms, it became apparent that the Goddard MP was a better choice than its Reisner-2 counterpart for this research because of its capability to better model stratiform rain and produce lower, more reasonable surface reflectivities. Vertical distributions of reflectivities within the stratiform region for the GRLNC2gd (Fig. 32a) and GRLNC2r2 (Fig. 32b) runs of the 26 November 2005 storm display many of the same differences already discussed and which occur over most of the storms modeled in this thesis. The GRLNC2gd run contains a more pronounced bright band with larger reflectivities above 8 km and a median near-surface reflectivity of 24 dBZ, slightly below what Schumacher and Houze (2006) found in the Tropics using the TRMM PR (~25 dBZ). The GRLNC2r2 run generates reflectivities from the bright band to the surface that are 4-6 dBZ higher than in the GRLNC2gd run. Both microphysics schemes also have decreasing reflectivity values from the bright band to the surface, which do not

appear in most radar-observed stratiform reflectivity structures, implying that MM5 may have too much evaporation towards the surface. Cross sections of the storms modeled in this study display realistic mid-level structures of reflectivity with prominent bright bands near the melting level, but some storms show areas with strong reflectivities (>25 dBZ) just a few km above the surface with weak or nonexistent echo directly below them at the surface. This problem seems to be greater for the Reisner-2 scheme and is particularly evident in the LLTS-MCS cases that struggle with where the transition between the precipitating stratiform cloud and non-precipitating anvil cloud should occur, thus leading to an underestimate of the stratiform rain component of the system.

Convective regions between Reisner-2 and Goddard MM5 runs have less disparity in radar reflectivities than stratiform regions do, but the Goddard scheme typically simulates more pronounced bright bands and smaller (~1 dBZ) near-surface reflectivities as shown in the GRLNC2gd (Fig. 32c) and GRLNC2r2 (Fig. 32d) runs' convective reflectivity structures. These generalizations apply to model runs that use the Grell CP on D2 and are applicable across most of the storms in this study, with some storms having even greater disparities in reflectivity structures between model runs using Goddard and Reisner-2 MP schemes. The median surface reflectivity for most storms is approximately 40 dBZ, which is ~6 dBZ higher than Schumacher and Houze (2006) found for all tropical convection and ~3 dBZ higher for tropical convective rain over West Africa, indicating that MM5 typically overestimates convective reflectivities for both MP schemes. However, both schemes usually display little growth of convective hydrometeors from the melting level toward the surface, suggesting that overevaporation

in MM5 may be compensating for the overproduction of graupel and snow that occurs above the melting level. This compensation may be in an effort to generate better surface quantitative precipitation forecasts (QPFs) at the expense of microphysically realistic vertical structures of reflectivity (Sandra Yuter, personal communication).

The Goddard MP scheme was chosen in this study because of its ability to generate more reasonable surface reflectivities and higher stratiform area fractions with less variability between runs than using the Reisner-2 scheme. Table 3 shows that the mean stratiform area fraction for all of the GRLgd and GRLNC2gd runs is 65.7% and 65.4%, respectively, which is greater than the 54.2% and 51.6% generated for the GRLr2 and GRLNC2r2 model runs, respectively. The trend in stratiform area fractions increasing as the degree of baroclinicity increases across each storm type still holds regardless of which parameterization set is used. Most of the barotropic and weakly baroclinic systems have stratiform area fractions that are 10-25% higher in the Goddard model runs, with the disparity between the two MP schemes decreasing as the degree of baroclinicity increases. As a result, stratiform area fractions vary more with baroclinicity in the Reisner-2 model runs as indicated by their larger standard deviations. Similarly, there tends to be more variation in the stratiform area fractions between the GRLNC2r2 and GRLr2 runs for each individual storm than in the Goddard runs.

Although the divergence profiles generally become less elevated as the degree of baroclinicity increases regardless of which parameterization set is employed, LNDs are sensitive to the choice of MP and whether the Grell CP scheme is used on D2. Tables 4-6 summarize the differences in the total, stratiform, and convective LNDs based on

changes in the MP and CP. Mean LNDs for model runs that explicitly resolve convection on D2 are about 0.5 km higher than those that employ the Grell cumulus parameterization on both D1 and D2. Similarly, the GRLNC2gd (5.5 km) and GRLgd (4.9 km) runs have mean LNDs that are higher than their Reinser-2 counterparts (5.2 km and 4.7 km for GRLNC2r2 and GRLr2, respectively). Although this difference does not appear to be caused by a systematic bias in the stratiform LNDs (~7.3-7.4 km), the higher mean LND for the runs using Goddard MP is probably due to the larger stratiform area fractions. However, the bias towards higher mean LNDs for the MM5 runs that explicitly resolve convection on D2 is also apparent in the convective LNDs for the GRLNC2gd (5.1 km) and GRLNC2r2 (4.7 km) model runs which are higher than their counterparts that invoke the Grell CP scheme on both D1 and D2 (4.6 km and 4.5 km for GRLgd and GRLr2, respectively).

The lower total and convective LNDs coupled with the higher echo tops observed for the model runs that explicitly resolve convection on D2 suggests that using a CP at lower resolutions may suppress convection and cause divergence profiles that are less elevated than when explicitly resolving convection. This observation is supported by Warner and Hsu (2000) who used a similar configuration of grid domains in MM5 to simulate a summertime storm in south central New Mexico. Warner and Hsu found that using CPs on an intermediate resolution grid (equivalent to D2 in this study with 10-km resolution) induces warming above 600-700 hPa and cooling below, along with drying from 500-700 hPa and some moistening below, quintessential stratiform characteristics. Although the Grell CP scheme had less suppression of precipitation on D3 than other

CPs evaluated in Warner and Hsu's study, it still induced some stabilization and drying at mid-levels that suppressed convection during times when the simulated QPF was deficient. Hopefully, the ongoing refinement of existing MP and CP schemes and the development of new ones for the Weather Research and Forecasting (WRF) model and MM5 will help improve QPF forecasts at the surface *along with* the vertical structure of hydrometeors and number concentrations of graupel, snow, and ice that are essential to quantifying diabatic heating.

7. CONCLUSIONS AND IMPLICATIONS

Precipitating systems occurring in the subtropical region of southeast Texas that have been simulated in MM5 and observed by ADRAD display mean divergence profiles whose magnitudes and structures vary across the region's wide spectrum of baroclinicities and common storm types. Barotropic storms during the summer months have the most elevated divergence structures (indicated by their highest mean LNDs) because their tropopause heights are highest, allowing convection to penetrate through and distribute mass flux perturbations over a greater depth of the atmosphere. Barotropic storms typically have the largest magnitudes of divergence because these storms have the greatest amount of deep convection relative to stratiform rain (indicated by their low stratiform area fractions). As the degree of baroclinicity increases, stratiform area fractions increase even though tropopause heights decrease, limiting the relative amount of convection and the height to which that convection can reach, respectively. However, some weakly baroclinic storms contain stratiform area fractions and divergence profiles with magnitudes and LNDs that are similar to barotropic storms, despite having lower tropopause heights and convection that is not as deep. Future research developing numerically-based baroclinicity regimes should better correlate divergence variations with baroclinicity and quantify the number of weakly baroclinic storms that have more tropical-like divergence profiles.

Robust stratiform and convective divergence signals were also obtained by applying Steiner et al.'s (1995) separation algorithm to MM5 reflectivity data, despite the fact that MM5 generates stratiform area fractions that are lower than observed and

overestimates radar reflectivities at all levels. Barotropic storms have thicker and more elevated mid-level convergence in stratiform regions than in strongly baroclinic storms because most stratiform rain is caused by convection that is elevated and/or not as deep as in systems with lower degrees of baroclinicity. Weakly baroclinic storms typically fall somewhere in between depending on a particular storm's nature of convection, tropopause height, and stratiform area fraction. Convective divergence profiles have more variable magnitudes and LNDs, although storms with lower degrees of baroclinicity have more elevated profiles associated with deeper convection (except for strongly baroclinic storms containing only elevated convection). The fact that MM5 simulates realistic convective and stratiform divergence profiles is encouraging and has positive implications for future research because it implies that MM5 adequately handles mass field perturbations within not only convective but also stratiform regions, which have a much greater role in producing diabatic feedbacks capable of driving additional convection as shown by Mapes (1993) and Mapes and Houze (1995).

Both of the barotropic storms modeled in this study appear to have some active diabatic feedback by driving additional convection in the region, although it is probably on a smaller spatial and temporal scale than occurs in the Tropics. Some weakly baroclinic systems, particularly the 13-14 March 2007 and 18 June 2006 storms, appear to have some of the same influences as well because their diabatic feedbacks are not overwhelmed by the synoptic forcing mechanisms present. Although these feedbacks usually act over even shorter spatial and temporal scales than in barotropic storms, Stensrud (1996) has shown that the cumulative effects of many MCSs can produce

significant changes in the large-scale flow patterns and serve as a positive feedback mechanism for additional convection to form. In addition, Stensrud and Anderson (2001) have shown that areas of persistent midlatitude convection may have altered large-scale circulation patterns during the Midwestern floods in 1993, which this study speculates may also have contributed to flooding in Oklahoma and Texas during the summer of 2007. Regardless, the elevated divergence profiles (particularly in stratiform regions) generated by these storms circumstantially suggest that heating at upper-levels within stratiform regions can help drive additional convection in the subtropics and provides motivation to better quantify these potential diabatic feedbacks in the future.

Some variations in the stratiform area fractions and the LNDs and magnitudes of the mean divergence profiles are evident between the different storm types modeled in MM5 for southeast Texas, although the general trends with baroclinicity mentioned previously still hold for each storm type. Upper-level disturbances illustrate these trends well because they are the only storm type that is prevalent across all baroclinicities. However, their magnitudes of divergence are more modest than frontal LLTS-MCSs, which appear to have the lowest stratiform area fractions in MM5 and therefore the largest magnitudes of mean divergence. Likewise, the magnitudes of peak mid-level convergence in the stratiform regions of LLTS-MCSs are larger than they are for other storms in the study, most likely because of the concentrated nature of their storm-induced ascending front-to-rear and descending rear inflow jets. The other frontal storms modeled in this study have magnitudes of divergence and stratiform area fractions that are more comparable to upper-level disturbances, and the divergence structures and

magnitudes in both storm types depend upon whether stratiform rain forms from elevated convection, deep convection, or a combination of both. Many of these frontal systems with stronger baroclinicities also contain concentrated diabatic feedbacks that most likely affect the strength and propagation of their associated frontal zones and precipitating storm systems as shown by Bryan and Fritsch (2000) and Chang et al. (2002). Quantifying these diabatic feedbacks would improve future precipitation forecasts of frontal systems and is likely a rich area for further investigation.

Even though the results presented in this study do not appear to be affected by the choice of parameterization schemes employed, MM5 generates stratiform area fractions that are lower than observed and produces reflectivities that are too high near the surface and aloft, caused in part by producing too much snow and graupel at upper levels. MM5 may also have too much evaporation in the lower troposphere because MM5's reflectivities decrease more strongly from the bright band to the surface compared to observations. These deficiencies need to be addressed before attempting to calculate diabatic heating in MM5 (and likely WRF) because they would affect the magnitudes of diabatic heating profiles. In an effort to generate realistic subtropics-wide heating profiles, future work should focus on developing a long-term storm climatology for southeast Texas and analyzing the relative contribution each storm type has toward annual rainfall along with examining the representativeness of southeast Texas to other subtropical regions by TRMM satellite observations. Numerical definitions of baroclinic regimes would also help better correlate the changes in stratiform rain fractions and magnitudes and structures of divergence profiles with baroclinicity. Finally, the

climatological dynamic response caused by representative divergence (or if enough of the above factors are addressed, diabatic heating) profiles should be evaluated first over short time scales (by experimenting with nest interactions in MM5) and then perhaps extended to longer time and space scales by using longer integrations of regional or global models.

REFERENCES

Arakawa, A., and V. R. Lamb, 1977: Computational design of the basic dynamical process of the UCLA general circulation model. *Methods in Computational Physics,* **17,** 173-265.

Bartels, D. L., and R. A. Maddox, 1991: Midlevel cyclonic vortices generated by mesoscale convective systems. *Mon. Wea. Rev.,* **119,** 104-118.

Bell, G., and J. Janowiak, 1995: Atmospheric circulation associated with the Midwest floods of 1993. *Bull. Amer. Meteor. Soc.,* **76,** 681-695.

Betts, A. K., 1973: A composite cumulonimbus budget. *J. Atmos. Sci.,* **30,** 597-610.

Blackadar, A. K., 1976: Modeling the nocturnal boundary layer. Preprints, *Third Symp. On Atmospheric Turbulence, Diffusion and Air Quality,* Raleigh, NC, Amer. Meteor. Soc., 46-49.

--------, 1979: High resolution models of the planetary boundary layer. In *Advances in Environmental Science and Engineering,* J. Pfafflin and E. Ziegler, Eds., Vol. 1, Gordon and Breach, 50-85.

Bright, D. R., and S. L. Mullen, 2002: The sensitivity of the numerical simulation of the Southwest Monsoon boundary layer to the choice of PBL turbulence parameterization in MM5. *Wea. Forecasting,* **17,** 99-114.

Browning, K. A., and R. Wexler, 1968: The determination of kinematic properties of a wind field using Doppler radar. *J. Appl. Meteor.,* **7,** 105-113.

Brugman, K., 2007: Variations in storm structure and precipitation characteristics associated with the degree of environmental baroclinicity in southeast Texas. M.S. thesis, Dept. of Atmospheric Sciences, Texas A&M University, 87 pp.

Bryan, G. H., and J. M. Fritsch, 2000: Diabatically driven discrete propagation of surface fronts: A numerical analysis. *J. Atmos. Sci.,* **57,** 2061-2079.

Chang, E. K. M., 2001: GCM and observational diagnoses of the seasonal and interannual variations of the Pacific storm track during the cool seasons. *J. Atmos. Sci.,* **58,** 1784-1800.

--------, S. Lee, and K. L. Swanson, 2002: Storm track dynamics. *J. Climate,* **15,** 2163-2183.

Churchill, D. D., and R. A. Houze Jr., 1984: Development and structure of winter monsoon cloud clusters on 10 December 1978. *J. Atmos. Sci.,* **41,** 933-960.

Cifelli, R., and S. A. Rutledge, 1998: Vertical motion, diabatic heating, and rainfall characteristics in north Australia convective systems. *Quart. J. Roy. Meteor. Soc.,* **124,** 1133-1162.

--------, C.R. Williams, D.K. Rajopadhyaya, S. K. Avery, K.S. Gage, and P.T. May, 2000: Drop-size distribution characteristics in tropical mesoscale convective systems. *J. Appl. Meteor.,* **39,** 760-777.

Cook, K. H., 2003: Role of continents in driving the Hadley cells. *J. Atmos. Sci.,* **60,** 957-976.

DeMaria, M., 1985: Linear response of a stratified tropical atmosphere to convective forcing. *J. Atmos. Sci.,* **42,** 1944-1959.

Dudhia, J., 1989: Numerical study of convection observed during the Winter Monsoon Experiment using a mesoscale two-dimensional model. *J. Atmos. Sci.,* **46,** 3077-3107.

--------, 1993: A nonhydrostatic version of the Penn State-NCAR Mesoscale Model: Validation tests and simulation of an Atlantic cyclone and cold front. *Mon. Wea. Rev.,* **121,** 764-787.

--------, D. Gill, K. Manning, W. Wang, and C. Bruyere, 2005: PSU/NCAR mesoscale modeling system tutorial class notes and users' guide (MM5 modeling system version 3). http://www.mmm.ucar.edu/mm5/documents/tutorial-v3-notes.html. (Accessed on August 1, 2005)

Fritsch, J. M., and G. S. Forbes, 2001: Mesoscale convective systems. *Meteorological Monographs,* Ch. 9, 323-357.

Gamache, J. F., and Houze, R. A., Jr., 1982: Mesoscale air motions associated with a tropical squall line. *Mon. Wea. Rev.,* **110,** 118-135.

Garvert, M. F., C. P. Woods, B. A. Colle, C. F. Mass, P. V. Hobbs, and M. T. Stoelinga, 2005: The 13-14 December 2001 IMPROVE-2 event. Part II: Comparisons of MM5 model simulations of clouds and precipitation with observations. *J. Atmos. Sci.,* **62,** 3520-3534.

Grell, G. A., 1993: Prognostic evolution of assumptions used by cumulus parameterizations. *Mon. Wea. Rev.,* **121,** 764-787.

Hartmann, D. L., H. H. Hendon, and R. A. Houze Jr., 1984: Some implications of the mesoscale circulations in tropical cloud clusters for large-scale dynamics and climate. *J. Atmos. Sci.*, **41,** 113-121.

Haynes, P. H., and M. E. McIntyre, 1987: On the evolution of vorticity and potential vorticity in the presence of diabatic heating and frictional or other forces. *J. Atmos. Sci.*, **44,** 828-841

Hoskins, B. J., and P. Valdes, 1990: On the existence of storm tracks. *J. Atmos. Sci.,* **47,** 1854-1864.

Holton, J. R., 1992: *An Introduction to Dynamic Meteorology.* San Diego, CA; Academic Press, 511 pp.

Houze, R. A., Jr., 1977: Structure and dynamics of a tropical squall-line system. *Mon. Weather Rev*., **105**, 1540–1567.

--------, 1982: Cloud clusters and large-scale vertical motions in the tropics. *J. Meteor. Soc. Japan,* **60,** 396-410.

--------, 1993: *Cloud Dynamics*. San Diego, CA; Academic Press, 570 pp.

--------, 1997: Stratiform precipitation in regions of convection: A meteorological paradox? *Bull. Amer. Meteor. Soc.,* **78**, 2179-2196.

--------, and A. K. Betts, 1981: Convection in GATE. *Rev. Geophys. Space. Phys.,* **19,** 541-576.

--------, and C.-P. Cheng, 1977: Radar characteristics of tropical convection observed during GATE: Mean properties and trends over the summer season. *Mon. Wea. Rev.,* **118,** 613-654.

Keyser, D. A., and D. R. Johnson, 1984: Effects of diabatic heating on the ageostrophic circulation of an upper tropospheric jet streak. *Mon. Wea. Rev.,* **112,** 1709-1724.

Lopez, R. E., 1976: Radar characteristics of the cloud populations of tropical disturbances in the northwest Atlantic. *Mon. Wea. Rev.,* **104,** 269-283.

--------, 1978: Internal structure and development processes of C-scale aggregates of cumulus clouds. *Mon. Wea. Rev.,* **106,** 1488-1494.

Maddox, R. A., D. J. Perkey, and J. M. Fritsch, 1981: Evolution of upper tropospheric features during the development of a mesoscale convective complex. *J. Atmos. Sci.,***39,** 1664-1674.

Mapes, B. E., 1993: Gregarious tropical convection. *J. Atmos. Sci.,* **50,** 2026-2037.

--------, and R. A. Houze Jr., 1993a: An integrated view of the 1987 Australian monsoon and its mesoscale convective systems. Part II: Vertical structure. *Quart. J. Roy. Meteor. Soc.,* **119,** 733-754.

--------, and --------, 1993b: Cloud clusters and superclusters over the oceanic warm pool. *Mon. Wea. Rev.,* **121,** 1398-1415.

--------, and --------, 1995: Diabatic divergence profiles in western Pacific mesoscale convective systems. *J. Atmos. Sci.,* **52,** 1807-1828.

--------, and J. Lin, 2005: Doppler radar observations of mesoscale wind divergence in regions of tropical convection. *Mon. Wea. Rev.,* **133,** 1808-1824.

Ninomiya, K., 1971a: Dynamical analysis of outflow from tornadic-producing thunderstorms as revealed by ATS III pictures. *J. Appl. Meteor.,* **10,** 275-294.

--------, 1971b: Mesoscale modifications of synoptic situations from thunderstorm development as revealed by ATS III and aerological data. *J. Appl. Meteor.,* **10,** 1103-1121.

Reed, R. J., and E. E. Recker, 1971: Structure and properties of synoptic-scale wave disturbances in the equatorial western Pacific. *J. Atmos. Sci,* **28,** 1117-1133.

Reisner, J., R. M. Rasmussen, and R. T. Bruintjes, 1998: Explicit forecasting of supercooled liquid water in winter storms using the MM5 mesoscale model. *Quart. J. Roy. Meteor. Soc.,* **124B,** 1071-1107.

Riehl, H., 1969: Some aspects of cumulonimbus convection in relation to tropical weather systems. *Bull. Amer. Meteor. Soc.,* **50,** 587-595.

--------, and J. S. Malkus, 1958: On the heat balance in the equatorial trough zone. *Geophsyica,* **6,** 503-538.

Schumacher, C., and R. A. Houze Jr., 2003: Stratiform rain in the tropics as seen by the TRMM precipitation radar. *J. Climate,* **16,** 1739-1756.

--------, and --------, 2006: Stratiform precipitation production over sub-Saharan Africa and the tropical East Atlantic as observed by TRMM. *Quart. J. Roy. Meteor. Soc.,* **132,** 2235-2255.

--------, --------, and I. Kraucunas, 2004: The tropical dynamical response to latent heating estimates derived from the TRMM Precipitation Radar. *J. Atmos. Sci.,* **61,** 1341-1358.

Schupiatsky, A. B., A. I. Korotov, V. D. Menshenin, R. S. Pastushkov, and M. Jovasevic, 1975: Radar investigations of evolution of clouds in the eastern Atlantic. GATE Rep. 14, Vol. II, International Council of Scientific Unions/World Meteorological Organization, 177-187. [Available from WMO, Case Postale 2300, CH-1211, Geneva 2, Switzerland.]

--------, --------, and R. S. Pastushkov, 1976a: Radar investigations of the evolution of clouds in the East Atlantic, in TROPEX-74. *Atmosphere* (in Russian), Vol. 1, Gidrometeoizdat, 508-514.

--------, G. N. Evseonok, and A. I. Korotov, 1976b: Complex investigations of clouds in the ITCZ with the help of satellite and ship radar equipment, in TROPEX-74. *Atmosphere* (in Russian), Vol. 1, Gidrometeoizdat, 508-514.

Steiner, M., and R. A. Houze, Jr., 1993: Three-dimensional validation at TRMM ground truth sites: Some early results from Darwin, Australia. Preprints, *26th Int. Conf. on Radar Meteorology,* Norman, OK, Amer. Meteor. Soc., 417-420.

--------, --------, and S. E. Yuter, 1995: Climatological characterization of three-dimensional storm structure from operational radar and rain gauge data. *J. Appl. Meteor.,* **34,** 1978-2007.

--------, and J. A. Smith, 1998: Convective versus stratiform rainfall: An ice-microphysical and kinematic conceptual model. *Atmos. Res.*, **48**, 317–326.

Stensrud, D. J., 1996: Effects of persistent, midlatitude mesoscale regions of convection on the large-scale environment during the warm season. *J. Atmos. Sci.,* **53,** 3503-3527.

--------, and J. L. Anderson, 2001: Is midlatitude convection an active or passive player in producing global circulation patterns? *J. Climate,* **14,** 2222-2237.

Stoelinga, M., 2005: Simulated equivalent reflectivity factor as currently formulated in RIP: Description and possible improvements. White paper, 5 pgs. http://www.atmos.washington.edu/~stoeling/RIP_sim_ref.pdf. (Accessed on July 1, 2006)

Tao, W.-K., and J. Simpson, 1993: Goddard cumulus ensemble model. Part I: Model description. *Terr. Atmos. Oceanic Sci.,* **4,** 25-72.

Thompson, G., R. M. Rasmussen, and K. Manning, 2004: Explicit forecasts of winter precipitation using an improved bulk microphysics scheme. Part I: Description and sensitivity analysis. *Mon. Wea. Rev.,* **132,** 519-542.

Trenberth, K. E., and D. P. Stepaniak, 2003: Seamless poleward atmospheric energy transports and implications for the Hadley circulation. *J. Climate,* **16,** 3705-3721.

Wallace, J. M. and P. V. Hobbs, 1977: *Atmospheric Science, An Introductory Survey.* San Diego, CA; Academic Press, 467 pp.

Warner, T. T., and H.-M. Hsu, 2000: Nested-model simulation of moist convection: The impact of coarse-grid parameterized convection on fine-grid resolved convection. *Mon. Wea. Rev.,* **128,** 2211-2231.

Yanai, M., S. Esbensen, and J.-H. Chu, 1973: Determination of bulk properties of tropical cloud clusters from large-scale heat and moisture budgets. *J. Atmos. Sci.,* **30,** 611-627.

Zhang, D.-L., 1982: A high-resolution model of the planetary boundary layer---Sensitivity tests and comparisons with SESAME-79 data. *J. Appl. Meteor.,* **21,** 1594-1609.

--------, and J. M. Fritsch, 1986: Numerical simulation of the meso-β scale structure and evolution of the 1977 Johnstown flood. Part I: Model description and verification. *J. Atmos. Sci.,* **43,** 1913-1943.

--------, and R. Harvey, 1995: Enhancement of extratropical cyclogenesis by a mesoscale convective system. *J. Atmos. Sci.,* **52,** 1107-1127.

Zipser, E. J., 1969: The role of organized unsaturated convective downdrafts in the structure and rapid decay of an equatorial disturbance. *J. Appl. Meteor.,* **8,** 799-814.

APPENDIX A: FIGURES

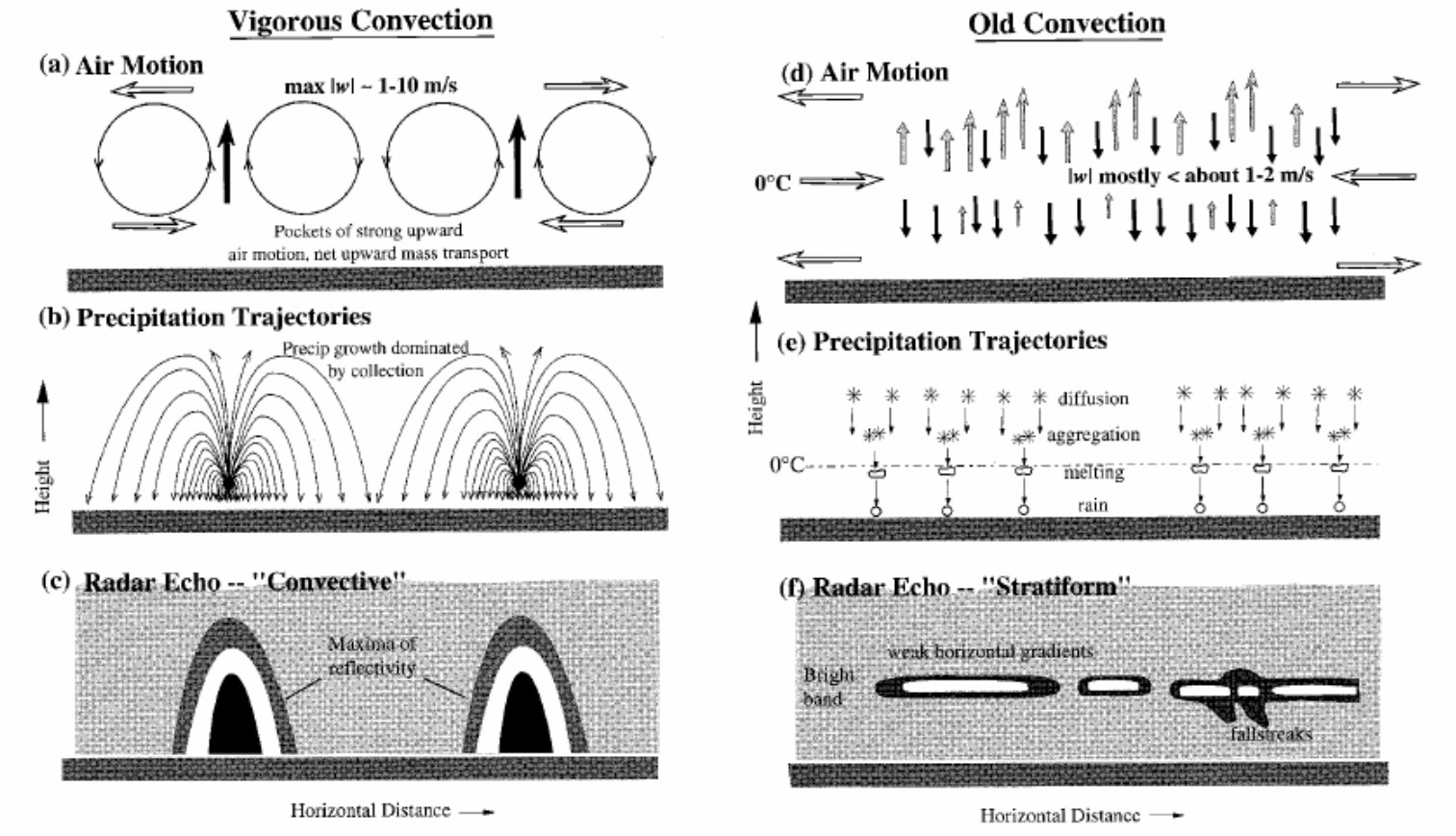

Figure 1 Conceptual model of vertical cross sections through (a)-(c) young, vigorous precipitating convection and (d)-(f) old convection (from Houze 1997).

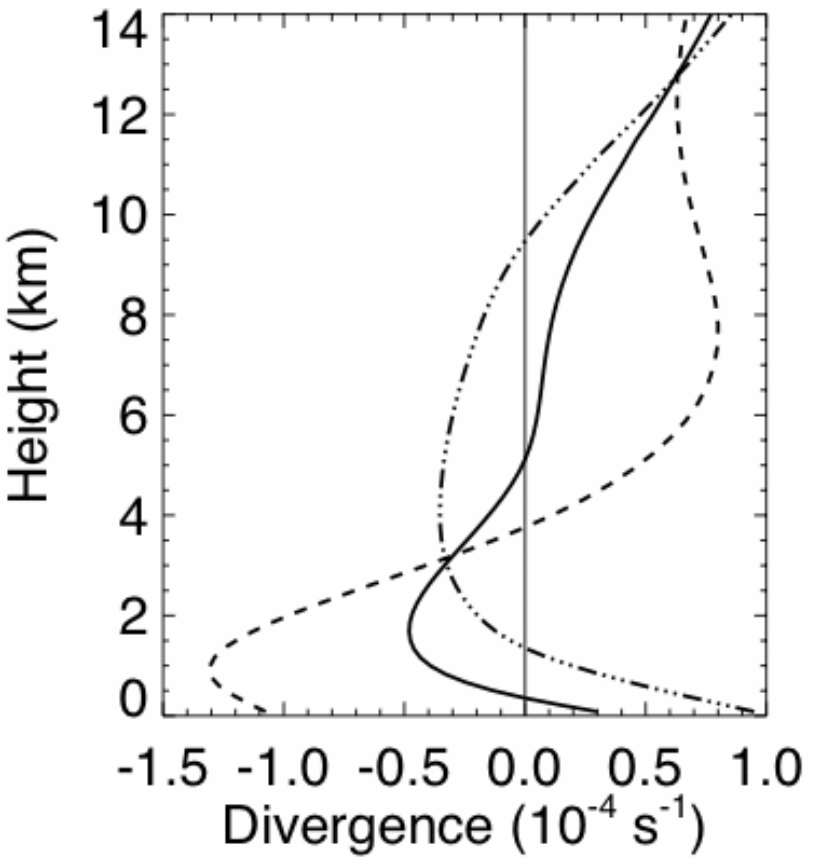

Figure 2 Mean divergence for the convective squall line (dashed), stratiform-anvil (solid) and combined (dotted) regions of a tropical squall-line system (adapted from Gamache and Houze 1982).

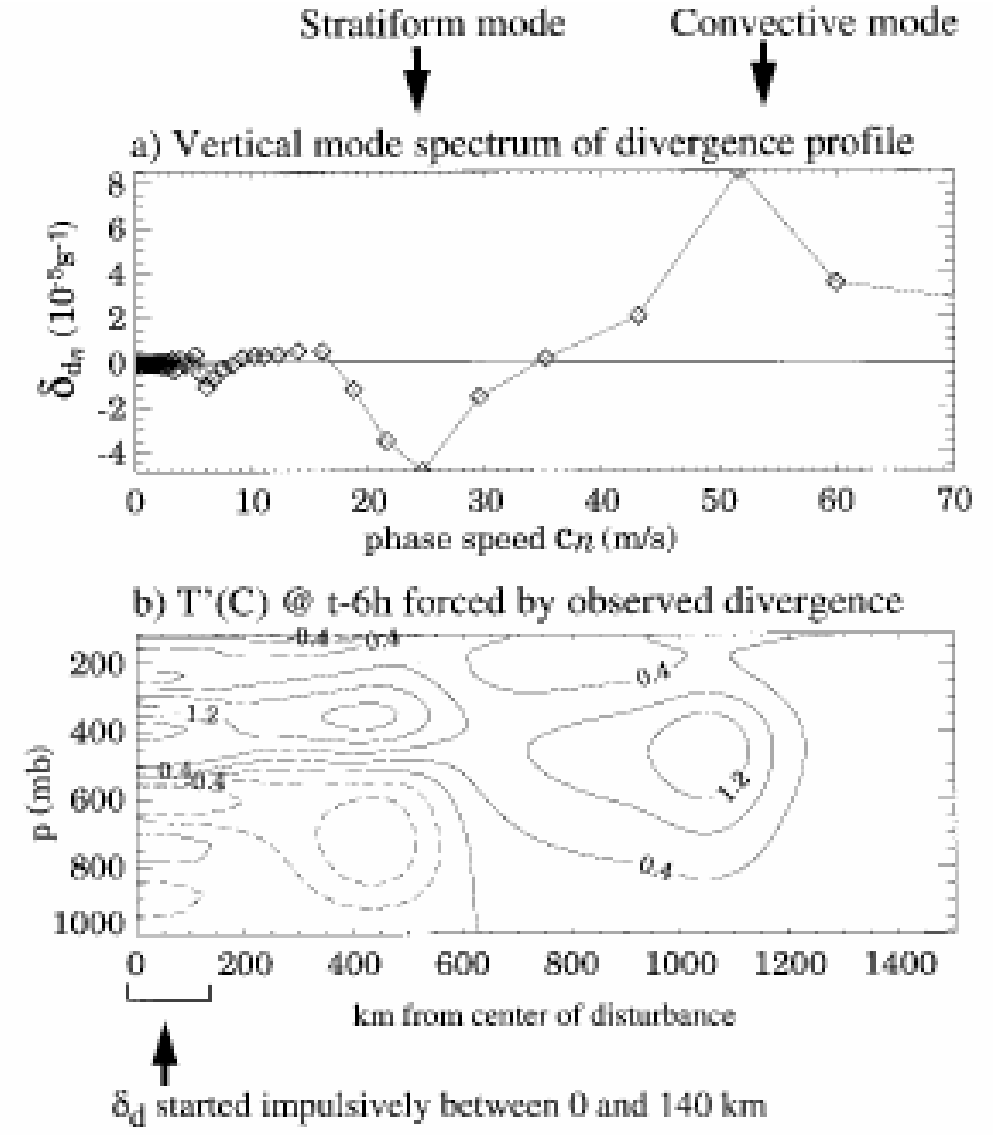

Figure 3 a) Vertical mode spectrum of the mean purl adiabatic divergence (δ_d) profile. (b) Model temperature perturbation field produced by the fast (convective) and slow (stratiform) gravity wave bores 6 h after the impulsive start (time *t*) of the heating from the purl-derived δ_d profile. Contour interval 0.4°C, negative contours dotted (from Houze 1997, originally presented in Mapes and Houze 1995).

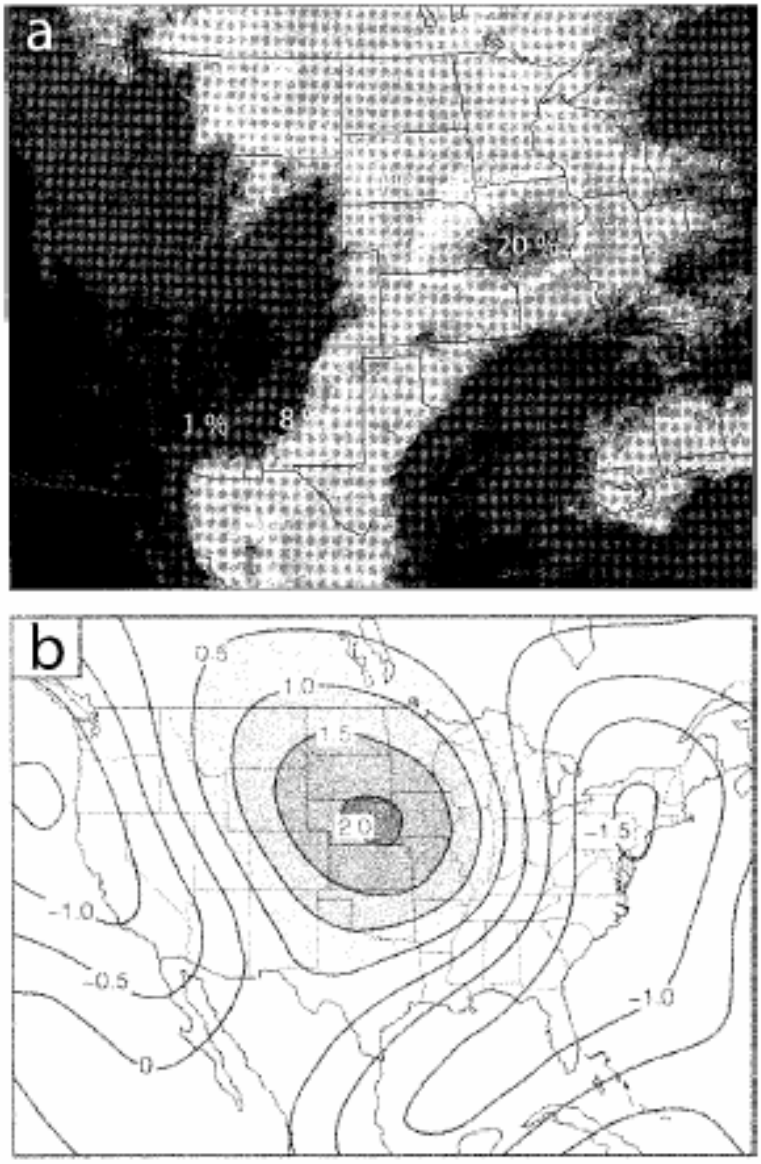

Figure 4 (a) Frequencies of cloud-top temperatures less than -38^{o}C derived from hourly infrared satellite imagery during Jul 1993. Black indicates less than 1% frequency, with other frequency values shown for various shadings. (b) The 200-hPa divergence anomaly from Jun and Jul 1993, with isolines every 0.5 x 10^{-6} s^{-1} (from Stensrud and Anderson 2001, (b) originally presented in Bell and Janowiak 1995).

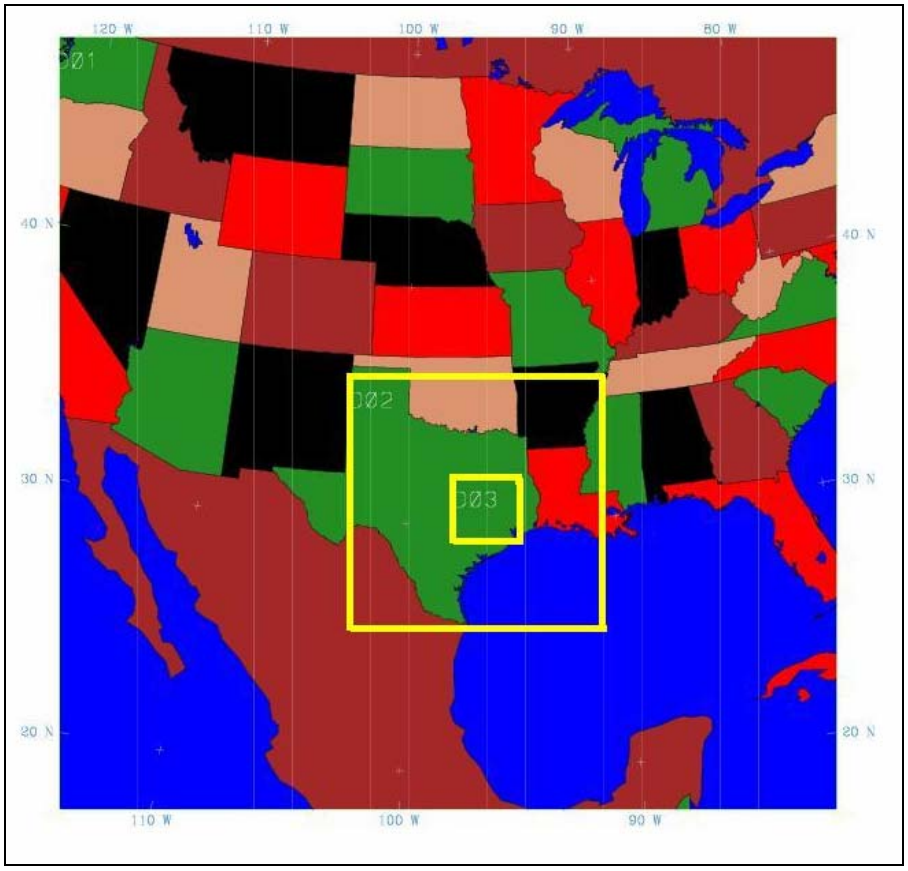

Figure 5 The MM5 model domains. The grid resolution of the outermost coarse domain 1 (D1), domain 2 (D2), and the innermost analysis domain 3 (D3) are 27, 9, and 3 km, respectively.

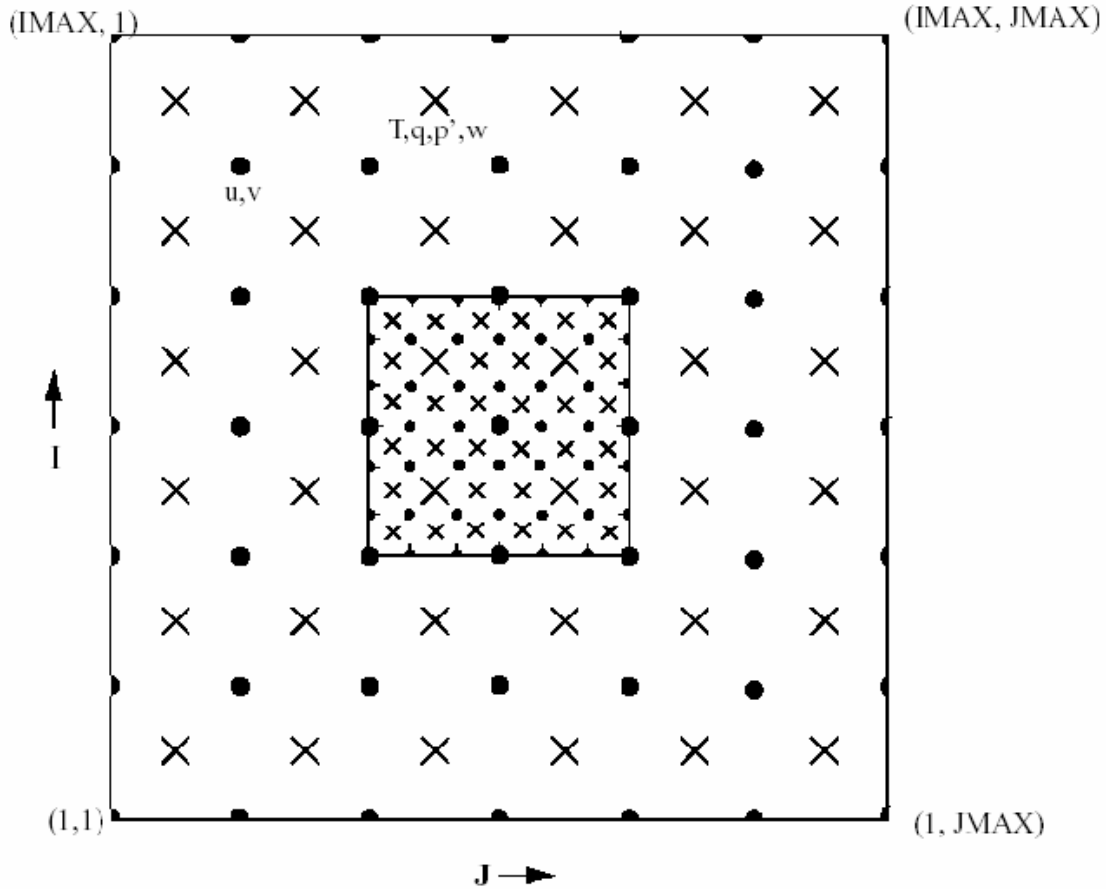

Figure 6 Schematic representation showing the horizontal Arakawa B-grid staggering of the dot (l) and cross (x) grid points. The smaller inner box is a representative mesh staggering for a 3:1 coarse-grid distance to fine-grid distance ratio (from Dudhia et al. 2005).

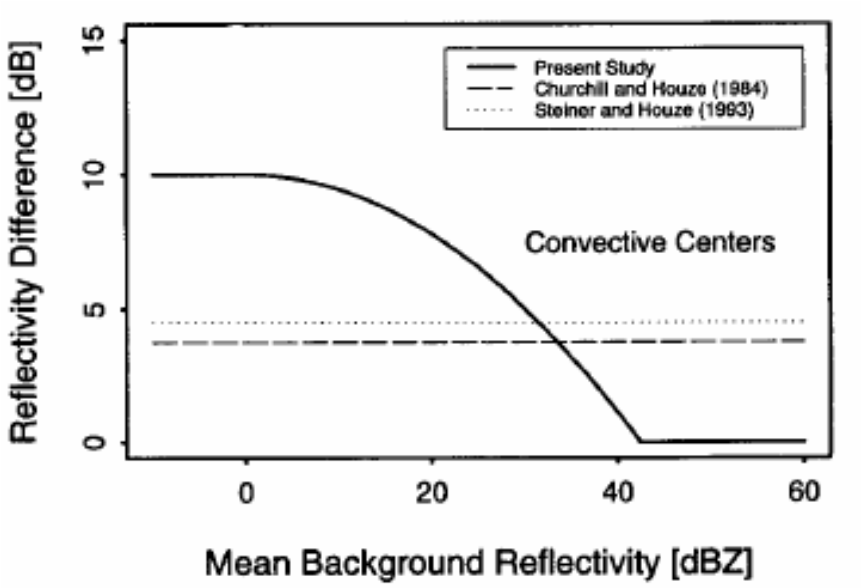

Figure 7 Peakedness criteria---i.e., the reflectivity difference between the grid point and mean background---used for convective center identification. In Steiner et al. (1995), the peakedness criterion is a function of the mean background reflectivity (solid line). Points along and above this curve are classified as convective centers. The constant peakedness criteria used by Churchill and Houze (1984) and Steiner and Houze (1993) are indicated by the dashed and dotted lines, respectively (from Steiner et al. 1995).

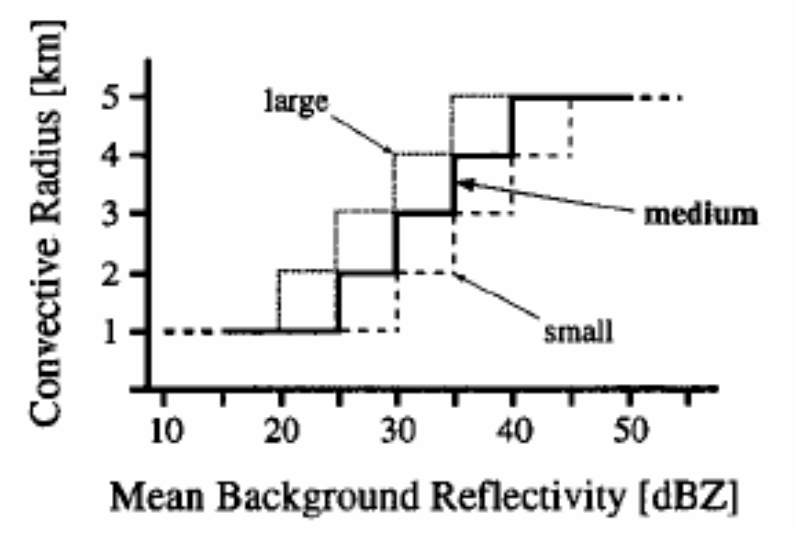

Figure 8 The convective area radius as a function of the mean background reflectivity. Three different relations are tested: large---dotted, medium---heavy, small---dashed line (from Steiner et al. 1995).

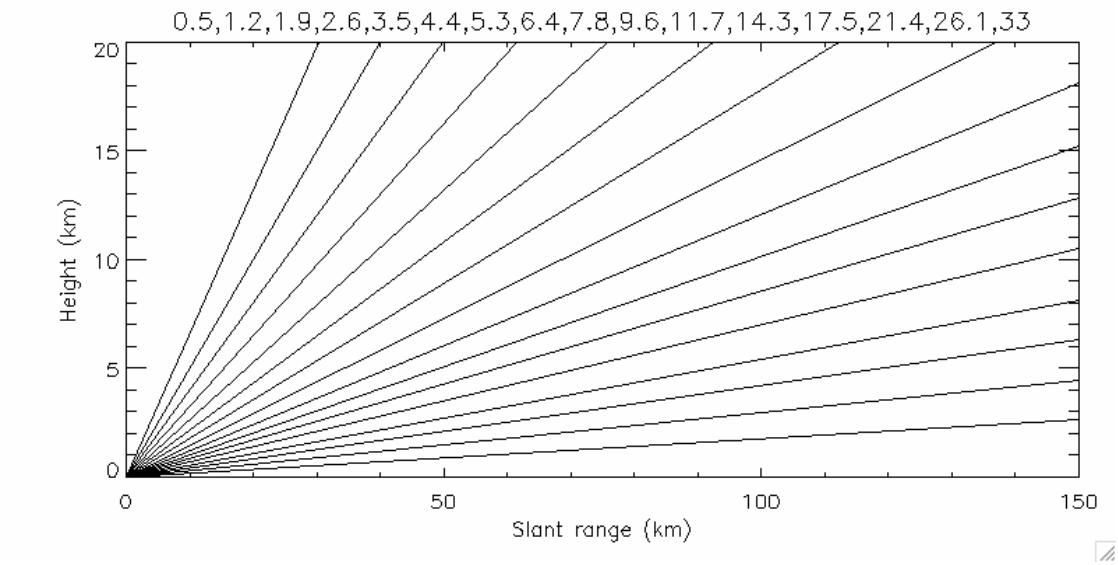

Figure 9 ADRAD's scan strategy used for the cases presented in section 4. Elevation angles (in degrees) are given at the top of the plot. The slant range assumes a standard atmospheric index of refraction and takes into account the curvature of Earth's surface.

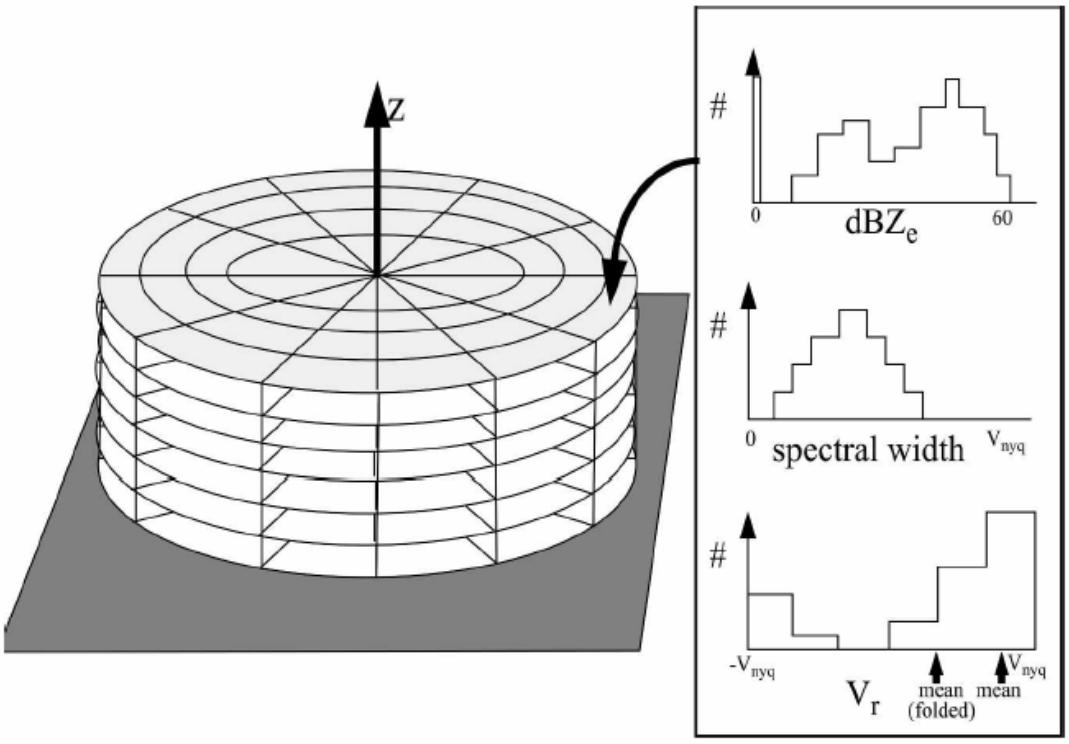

Figure 10 Schematic depiction of the cylindrical coordinate system, with histograms carried in each space-time grid cell (from Mapes and Lin 2005).

a) NEXRAD (1730 UTC 20 July 2007) b) MM5 (1900 UTC 20 July 2007)

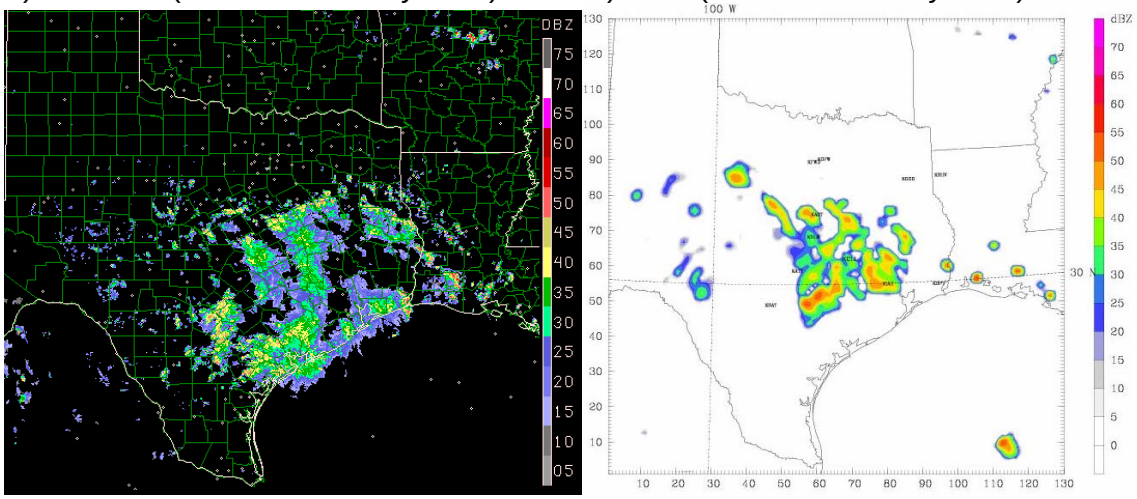

Figure 11 (a) NEXRAD and (b) MM5 reflectivity over D2 at the times indicated for the barotropic case presented in section 4a.

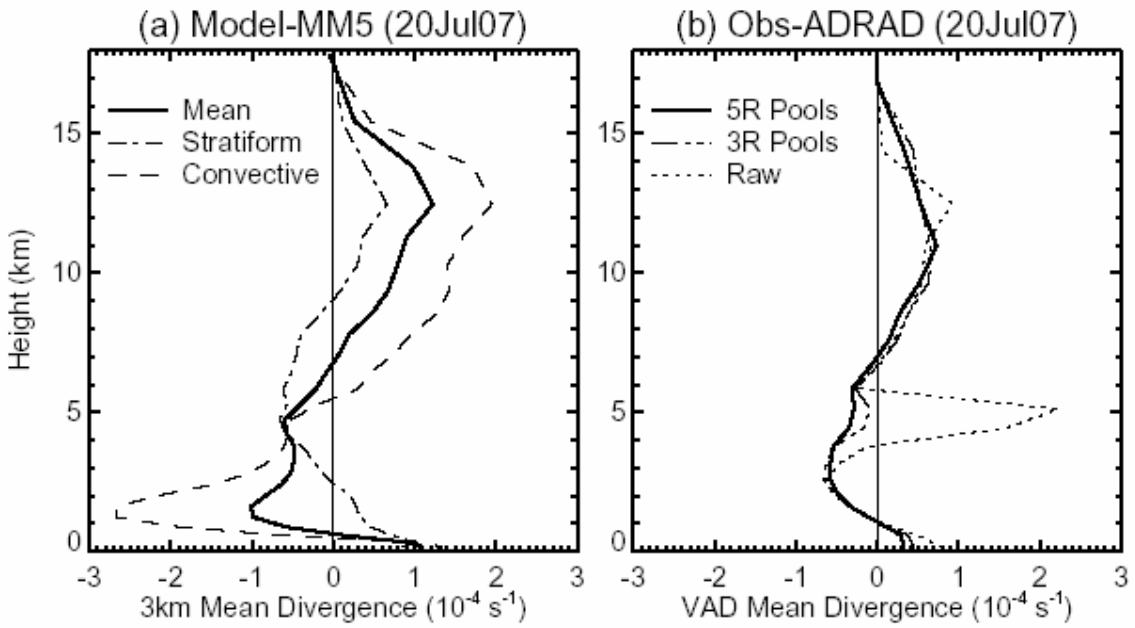

Figure 12 (a) MM5-derived mean grid-scale divergence profiles based on half-hourly model data (solid) and divergence profiles for stratiform (dash-dot) and convective (dashed) rain types as defined by the Steiner et al. (1995) separation algorithm applied to MM5-derived radar reflectivities between 1500-2300 UTC on 20 July 2007. The profiles include all grid boxes in a vertical column for which the surface radar reflectivity exceeds 5 dBZ. (b) Observed VAD (Mapes and Lin 2005) divergence profiles using ADRAD for five-range pooled data in 40-km annuli (solid), three-range pooled data in 24-km annuli (large dash with three smaller dashes), and the raw divergence from data in 8-km annuli (dotted). Each mean includes four sets of annuli centered about 28, 44, 60, and 76 km from ADRAD's center averaged hourly from 1500-1800 UTC. The mean divergence profile for the five-range pooled data is most closely analogous to the mean divergence in (a).

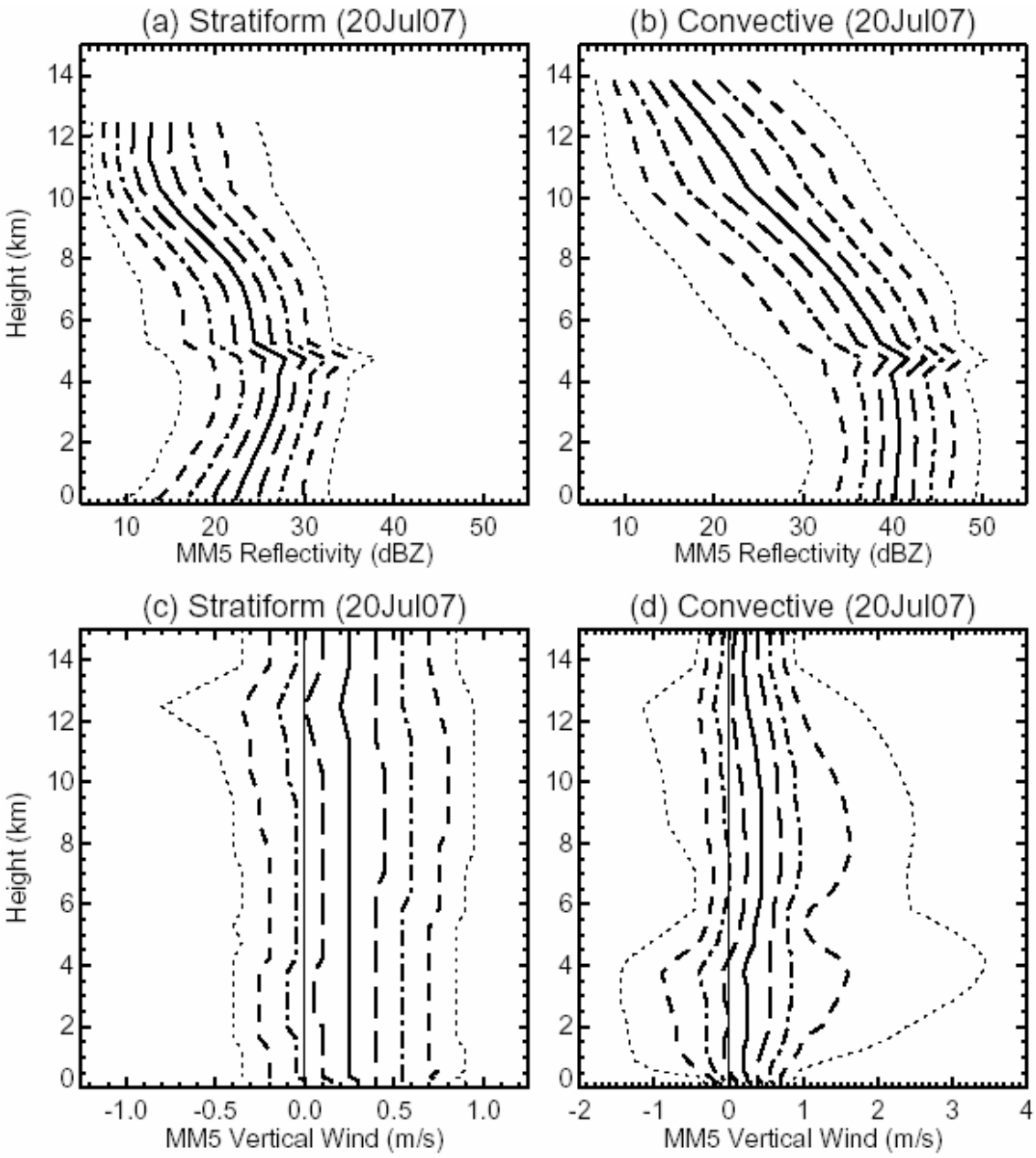

Figure 13 Vertical distributions of radar reflectivity (a-b) and vertical velocity (c-d) for stratiform and convective rain types as defined by the Steiner et al. (1995) separation algorithm applied to MM5 reflectivities between 1500-2300 UTC on 20 July 2007. The MM5 reflectivity profiles include all grid boxes in a vertical column for which the surface radar reflectivity exceeds 5 dBZ. Height levels with less than 0.5% of the total count are not plotted in the radar reflectivity plots. Each line represents a 10 % quantile from 10 to 90%; the median profile is the solid, thick line.

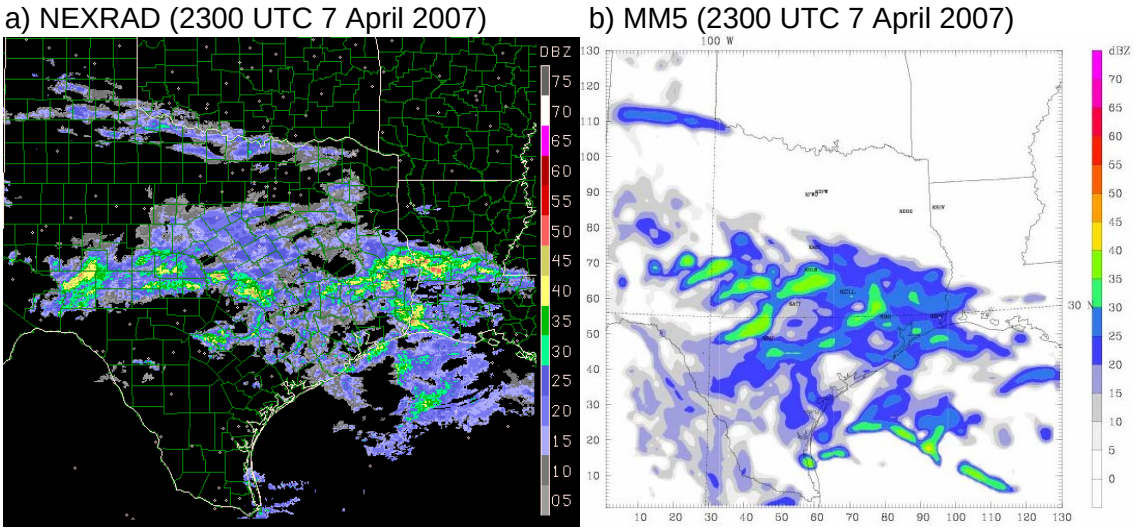

Figure 14 (a) NEXRAD and (b) MM5 reflectivity over D2 at the times indicated for the strongly baroclinic case presented in section 4b.

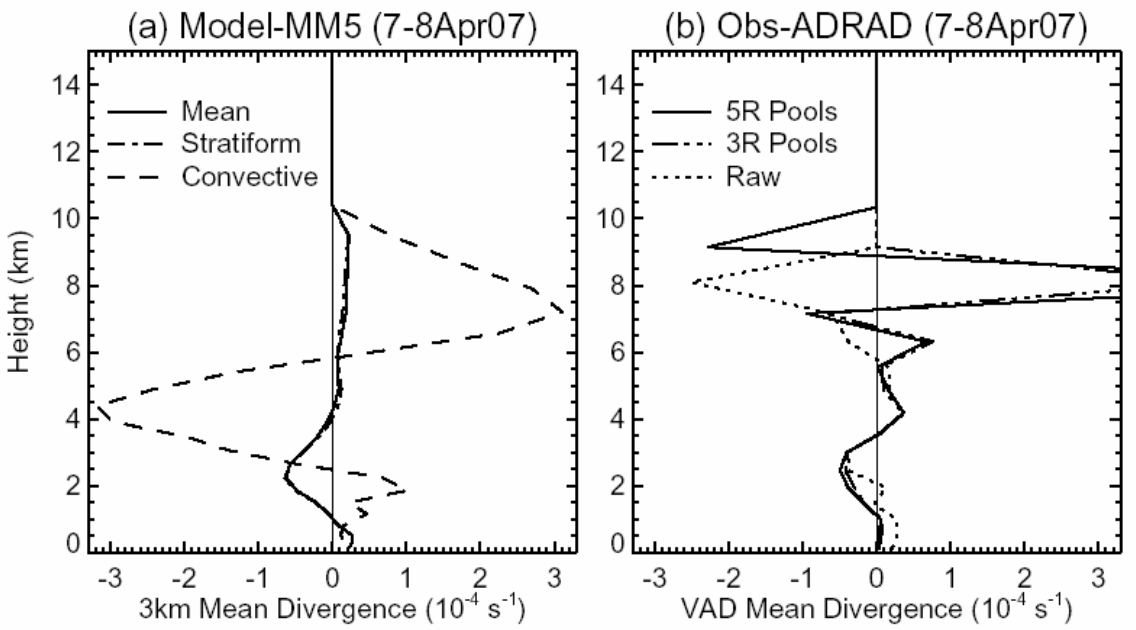

Figure 15 (a) MM5-derived mean grid-scale divergence profiles for half-hourly data from 1100 UTC 7 April to 1200 UTC 8 April 2007. (b) Observed VAD divergence profiles for hourly-averaged ADRAD data from 1900 UTC on 7 April to 0000 UTC on 8 April. The mean divergence profile for the five-range pooled data is most closely analogous to the mean divergence in (a). The same plotting conventions are followed as in Fig. 12.

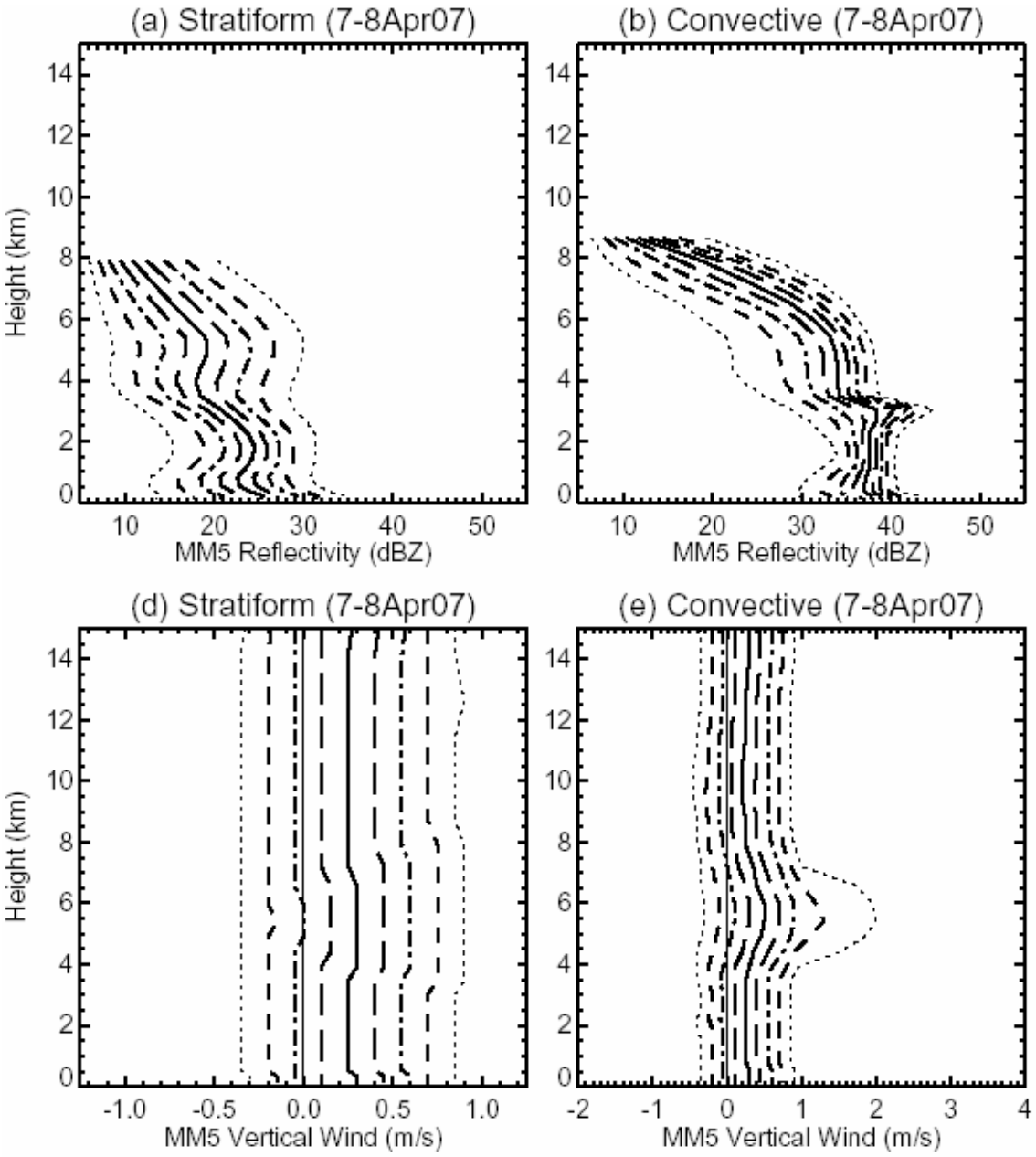

Figure 16 Vertical distributions of radar reflectivity (a-b) and vertical velocity (c-d) for stratiform and convective rain in MM5 from 1100 UTC 7 April 2007 to 1200 UTC 8 April 2007 following the plotting convention in Fig. 13.

a) NEXRAD (0130 UTC 14 March 2007)

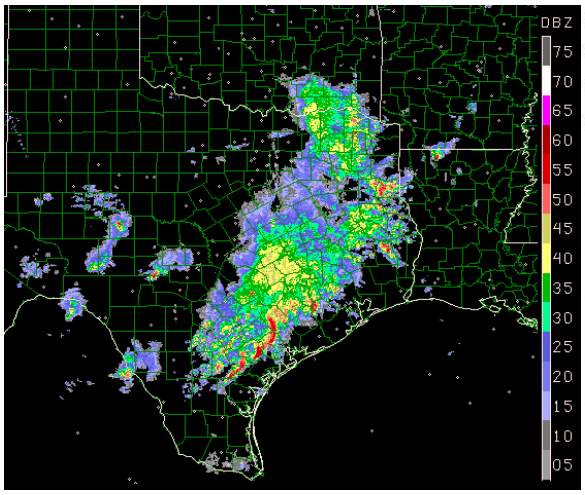

b) MM5 (0500 UTC 14 March 2007)

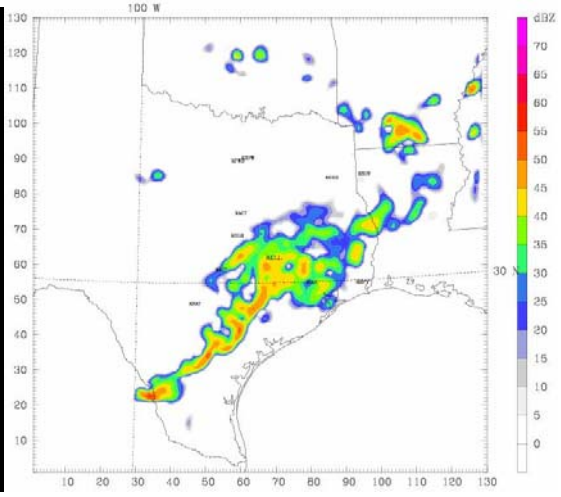

c) NEXRAD (2130 UTC 14 March 2007)

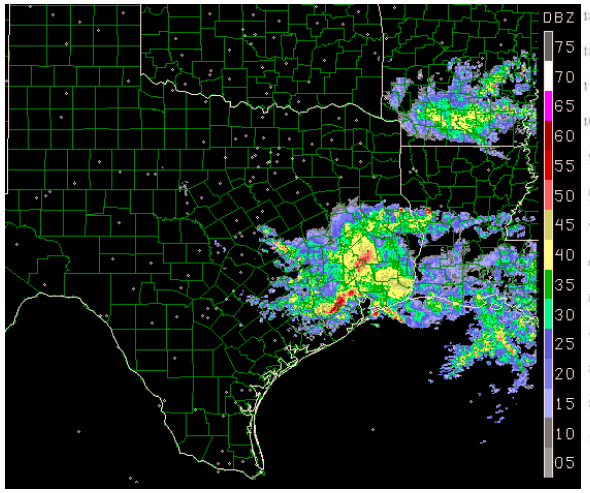

d) MM5 (2300 UTC 14 March 2007)

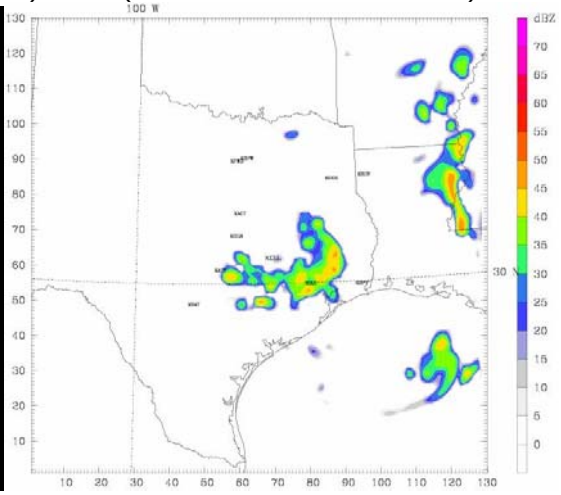

Figure 17 (a,c) NEXRAD and (b,d) MM5 reflectivity over D2 at the times indicated for the weakly baroclinic cases presented in section 4c.

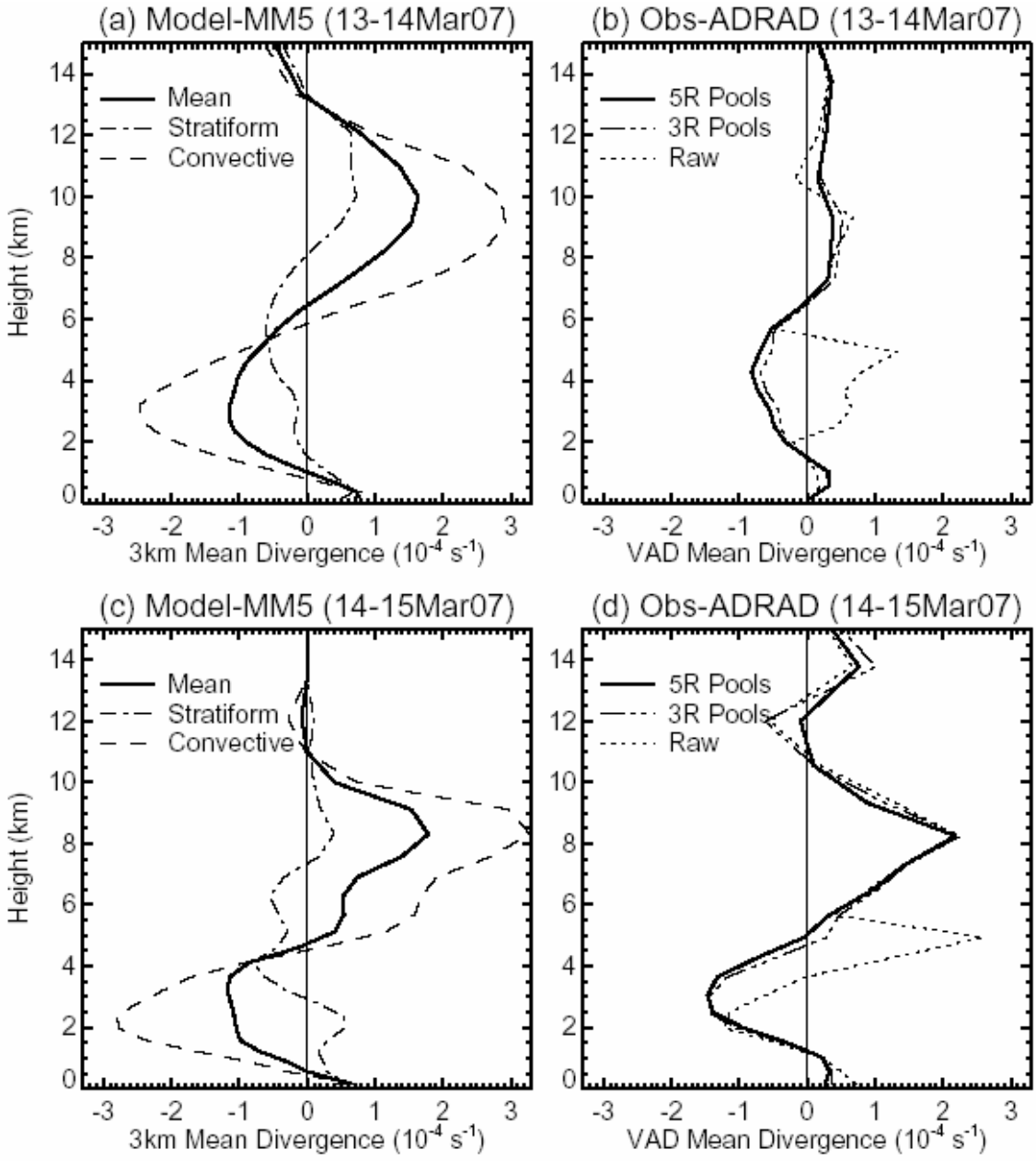

Figure 18 (a) MM5-derived mean grid-scale divergence profiles for half-hourly data from 1700 UTC 13 March to 1100 UTC 14 March 2007. (b) Observed VAD divergence profiles for hourly-averaged ADRAD data from 1900 UTC on 13 March to 0500 UTC on 14 March. (c) MM5-derived mean grid-scale divergence profiles for half-hourly data from 1400 UTC 14 March to 0400 UTC 15 March 2007. (d) Observed VAD divergence profiles for hourly-averaged ADRAD data from 1800-2300 UTC on 14 March. The mean divergence profiles for the five-range pooled data in (b) and (d) are most closely analogous to the mean divergence profiles in (a) and (c), respectively. The same plotting conventions are followed as in Figs. 12 and 15.

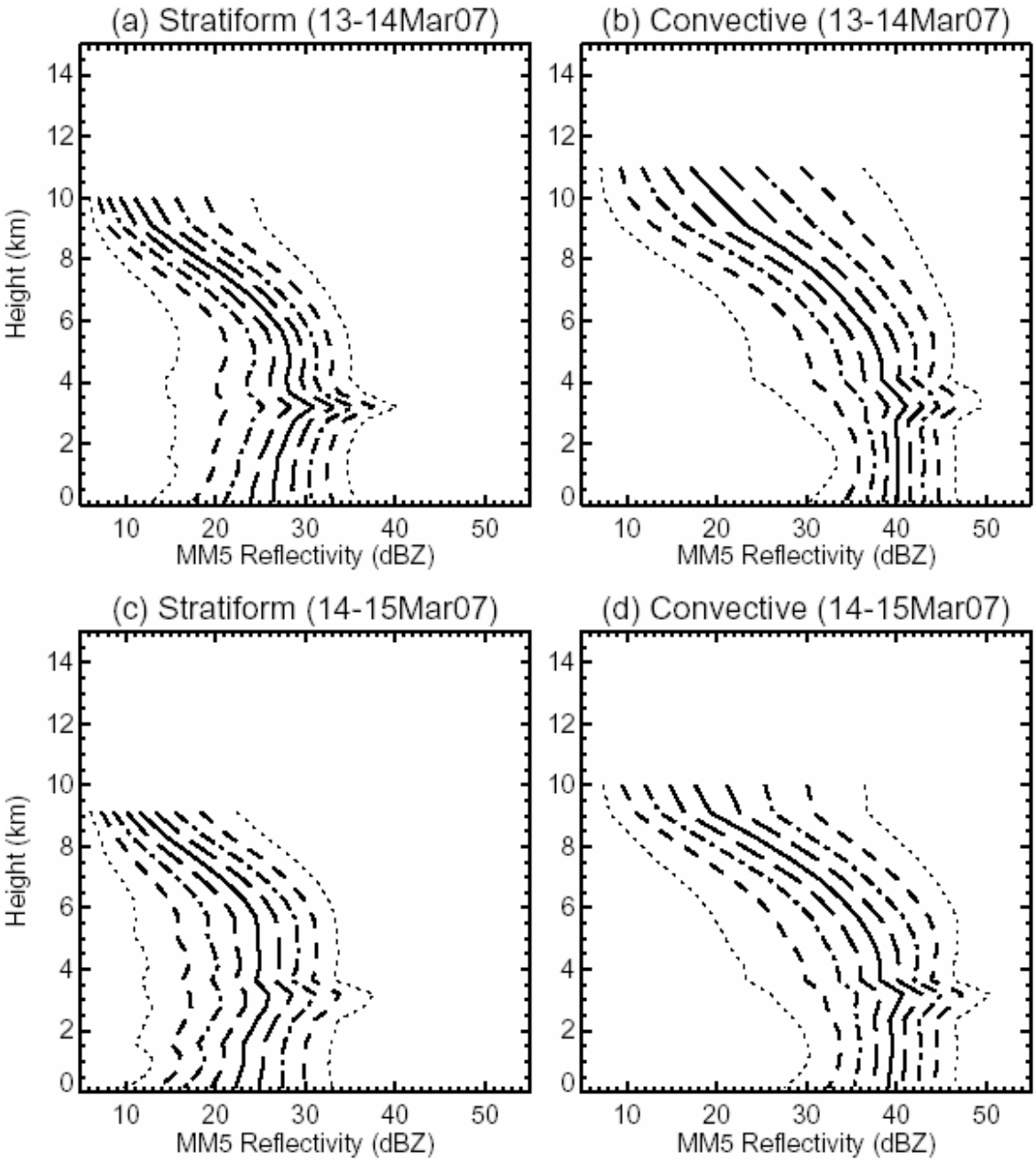

Figure 19 Vertical distributions of radar reflectivity for stratiform and convective rain in MM5 (a-b) from 1700 UTC 13 March 2007 to 1100 UTC 14 March 2007 and (c-d) from 1400 UTC 14 March 2007 to 0400 UTC 15 March 2007.

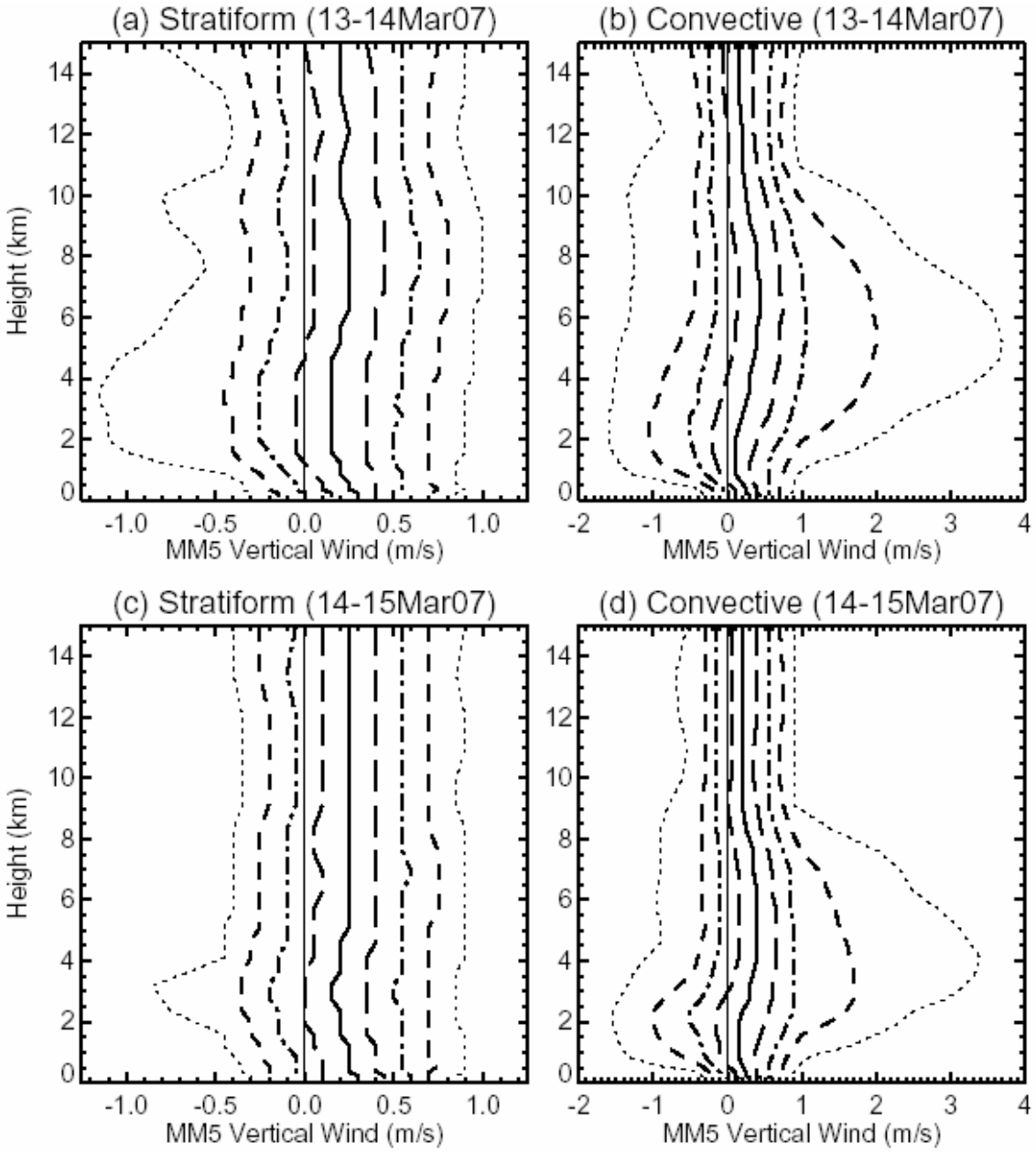

Figure 20 Vertical distributions of vertical velocity for stratiform and convective rain in MM5 (a-b) from 1700 UTC 13 March 2007 to 1100 UTC 14 March 2007 and (c-d) from 1400 UTC 14 March 2007 to 0400 UTC 15 March 2007.

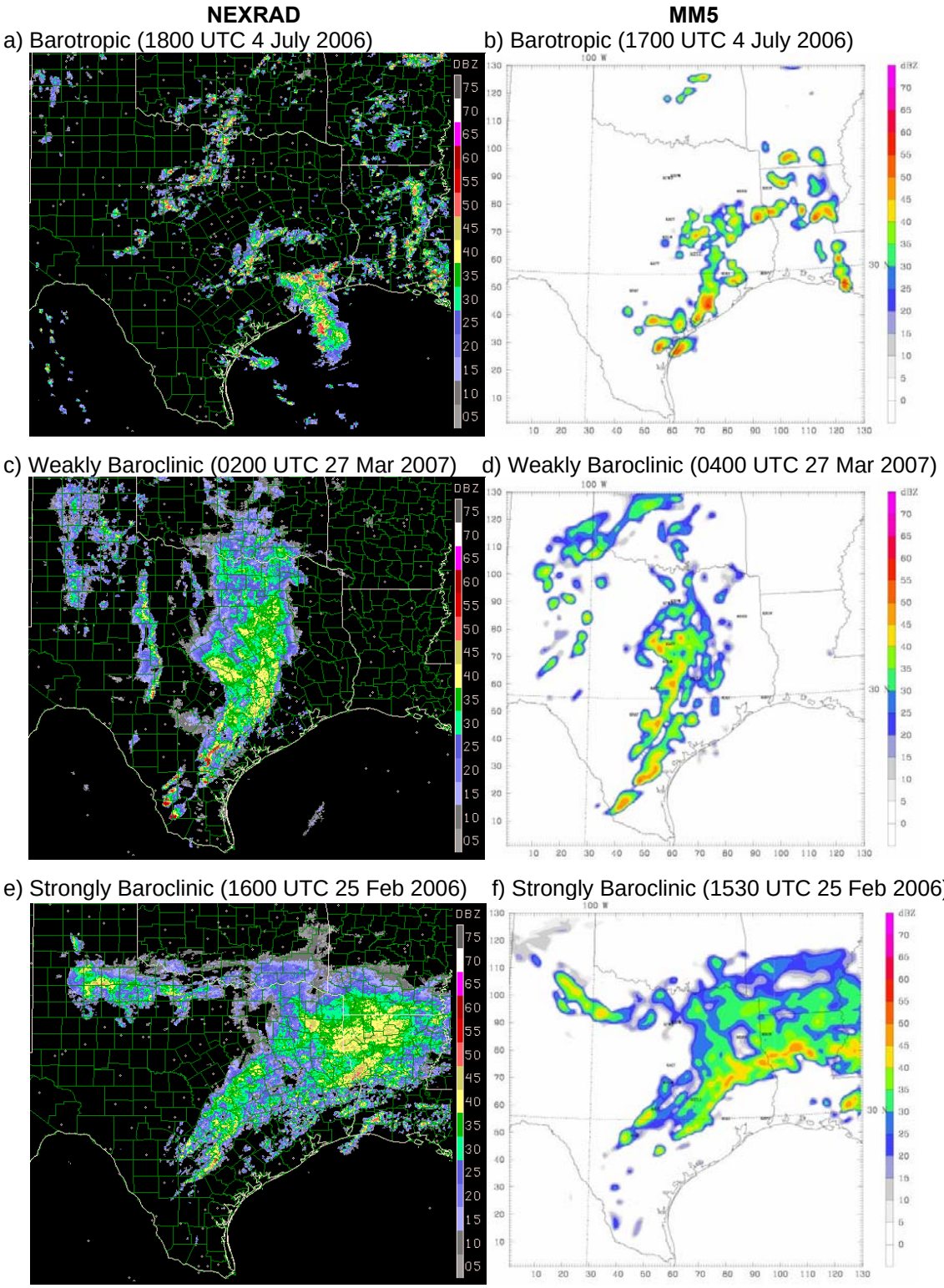

Figure 21 NEXRAD radar reflectivity and MM5 reflectivity over D2 at the times indicated for each of the upper-level disturbance cases presented in section 5a.

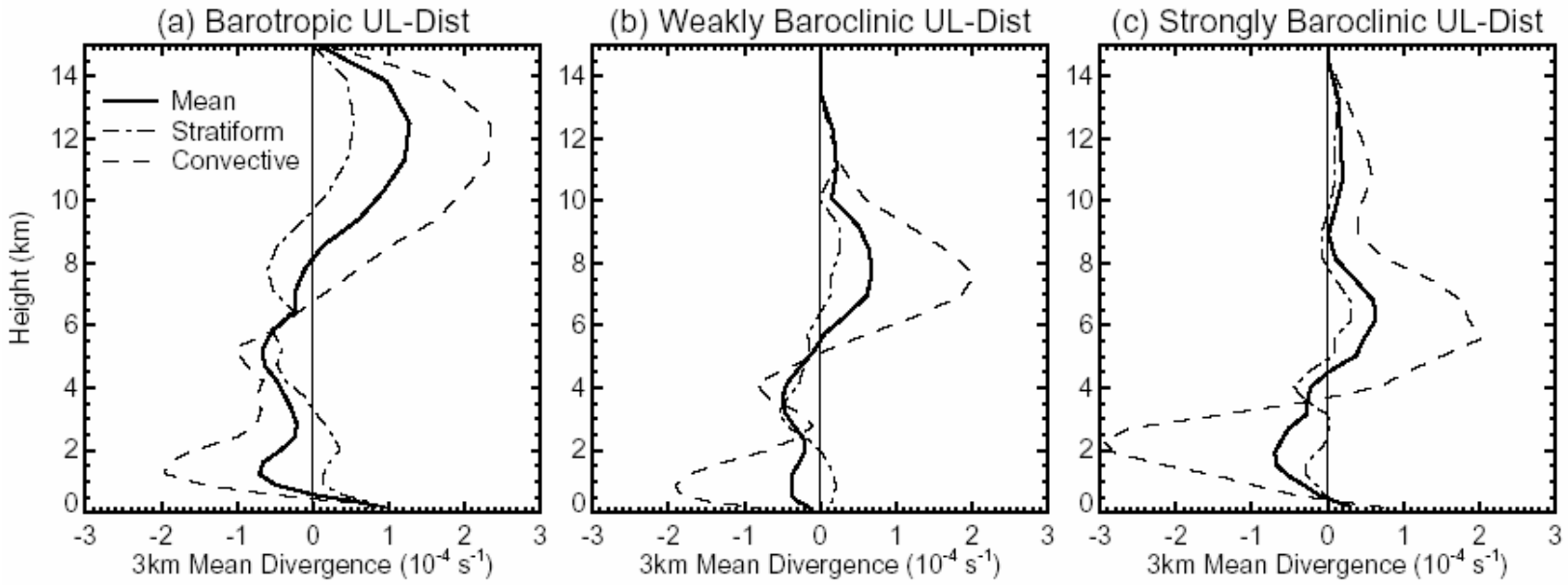

Figure 22 MM5-derived mean grid-scale divergence profiles for the upper-level disturbance cases using half-hourly model data for stratiform (dash-dot) and convective (dashed) rain types as defined by the Steiner et al. (1995) separation algorithm applied to MM5-derived radar reflectivities. The profiles include all grid boxes in a vertical column for which he surface radar reflectivity exceeds 5 dBZ. (a) Barotropic mean divergence profiles from 1000-2300 UTC on 4 July 2006. (b) Weakly baroclinic mean divergence profiles from 1900 UTC on 26 March to 1100 UTC on 27 March 2007. (c) Strongly baroclinic mean divergence profiles from 0500-2200 UTC on 25 February 2006.

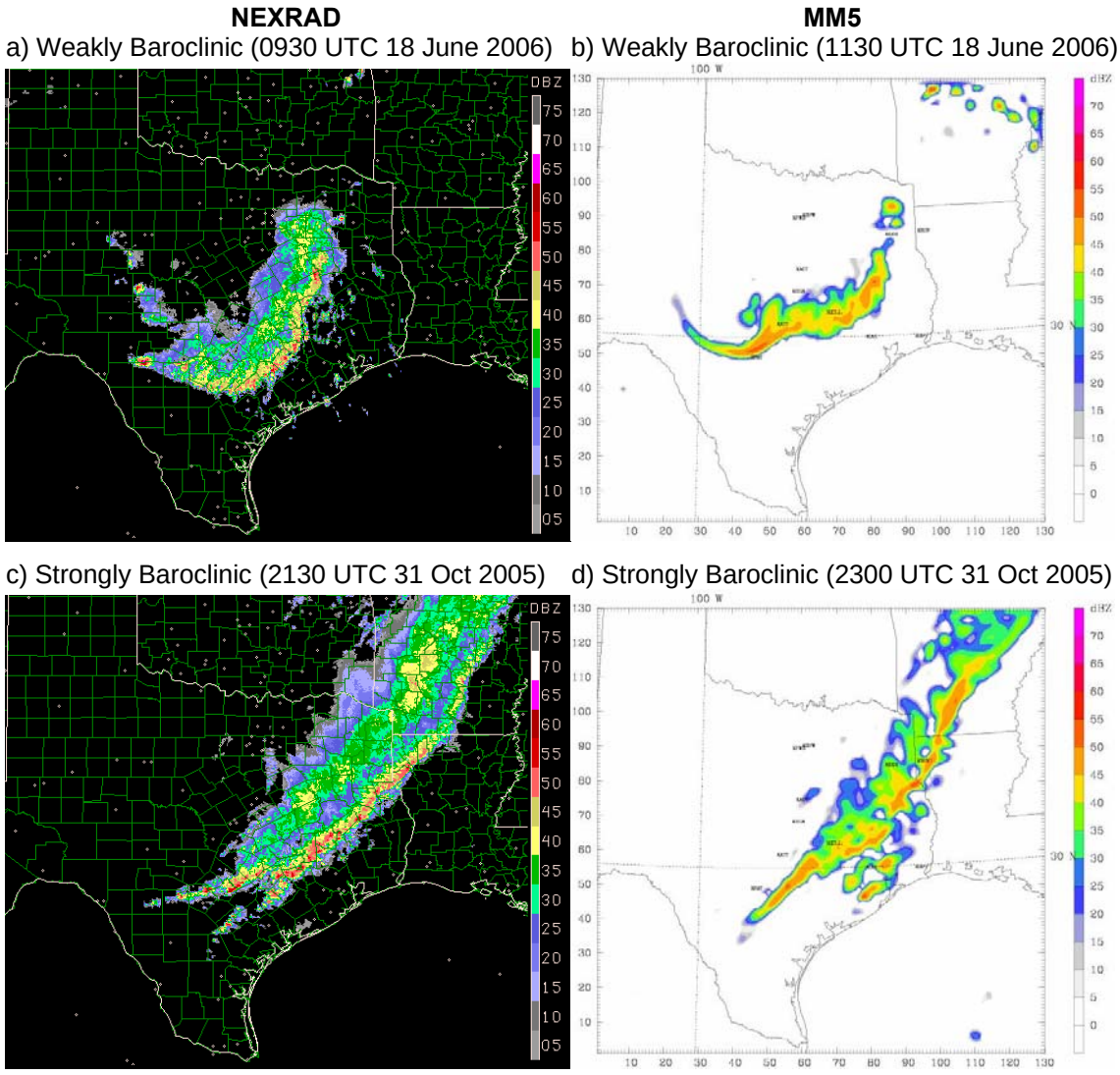

Figure 23 NEXRAD radar reflectivity and MM5 reflectivity over D2 at the times indicated for each of the frontal LLTS-MCS cases presented in section 5b.

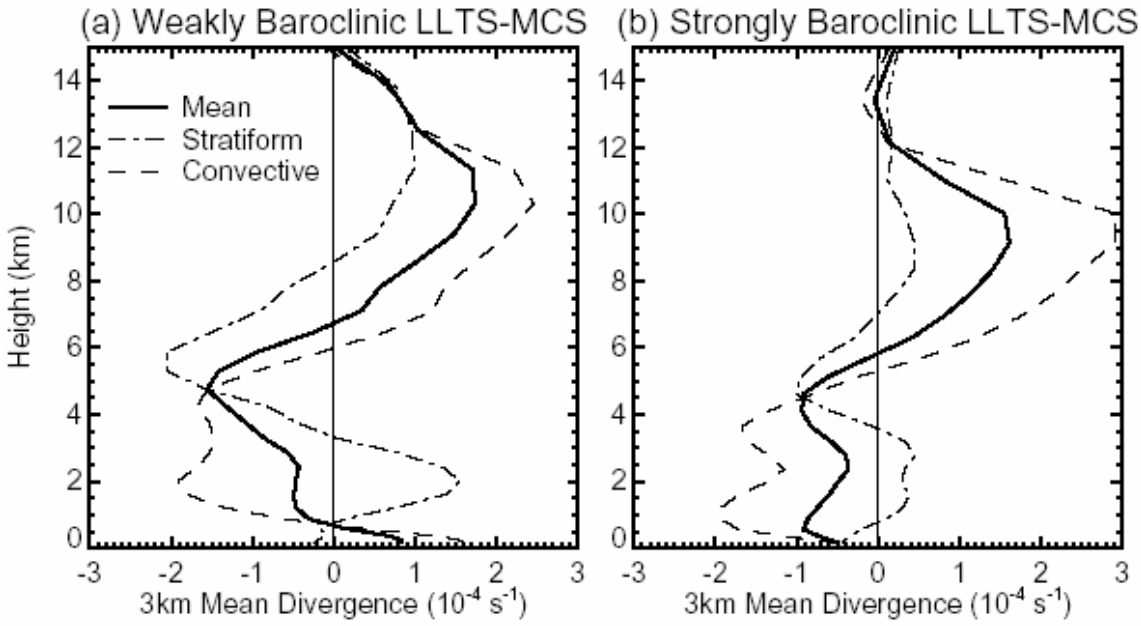

Figure 24 MM5-derived mean grid-scale divergence profiles for the frontal LLTS-MCSs using half-hourly model data following the plotting convection in Fig. 22. (a) Weakly baroclinic mean divergence profiles from 0600-1600 UTC on 18 June 2006. (b) Strongly baroclinic mean divergence profiles from 1800 UTC on 31 October to 0300 UTC on 1 November 2005.

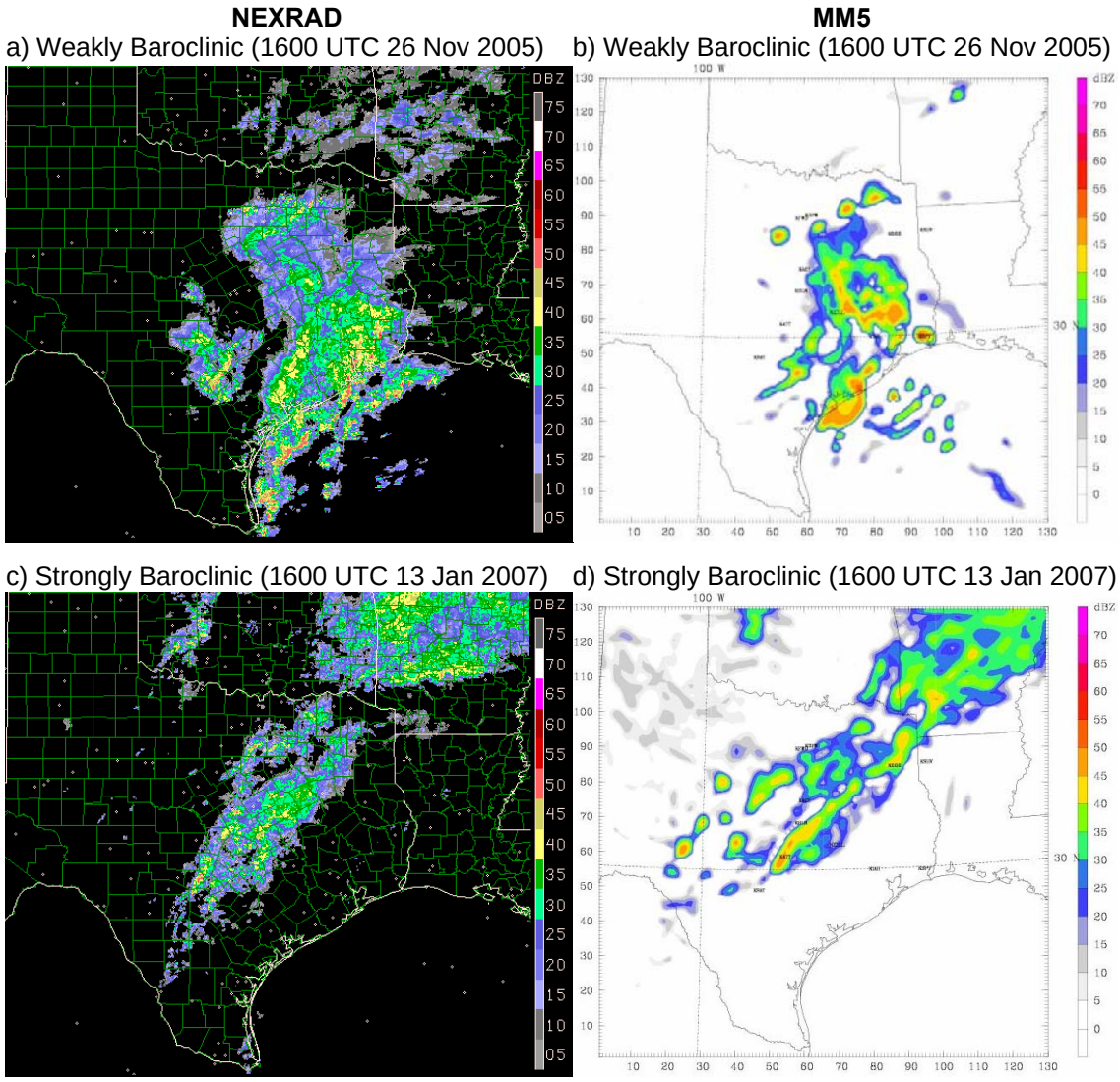

Figure 25 NEXRAD radar reflectivity and MM5 reflectivity over D2 at the times indicated for each of the frontal cases presented in section 5c.

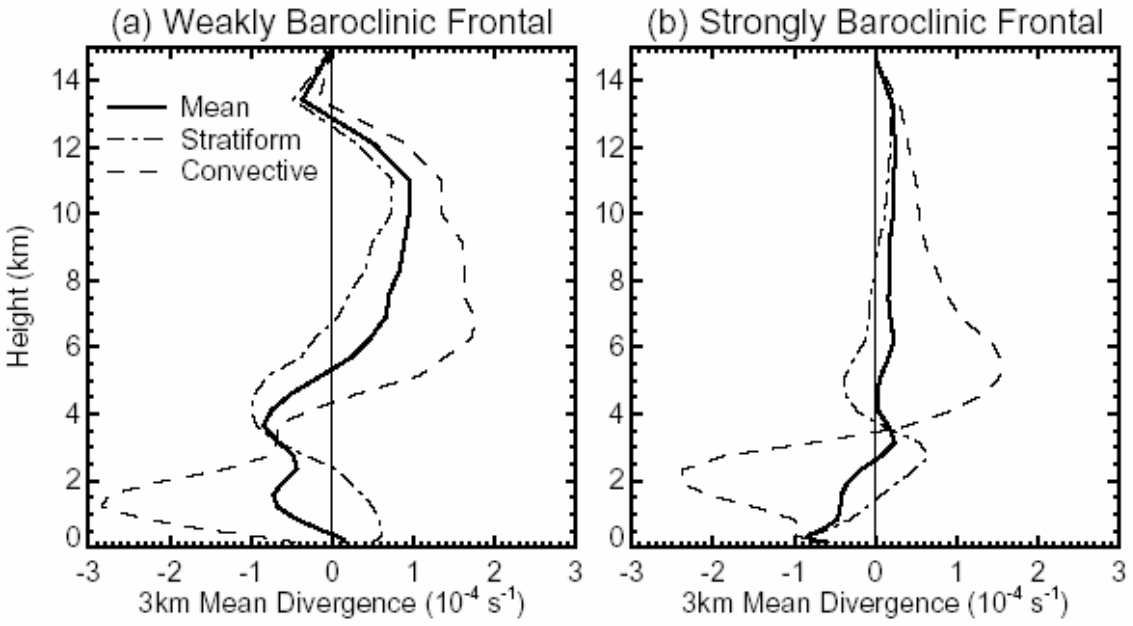

Figure 26 MM5-derived mean grid-scale divergence profiles for the frontal storm systems using half-hourly model data following the plotting convection in Figs. 22. (a) Weakly baroclinic mean divergence profiles from 0900-2000 UTC on 26 November 2005. (b) Strongly baroclinic mean divergence profiles from 0500 UTC on 13 January to 1700 UTC on 14 January 2007.

a) NEXRAD (0500 UTC 28 March 2006)

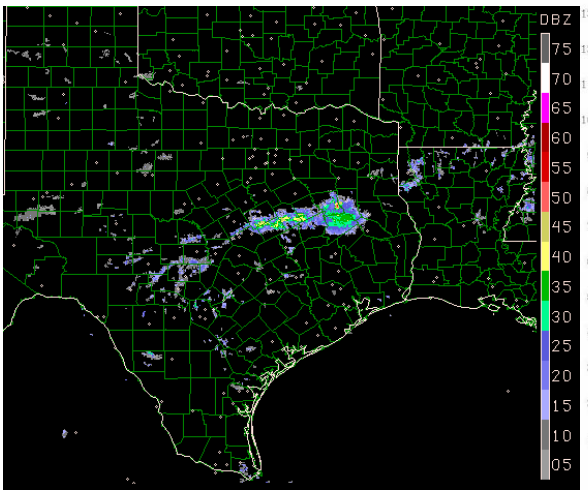

b) MM5 (0500 UTC 28 March 2006)

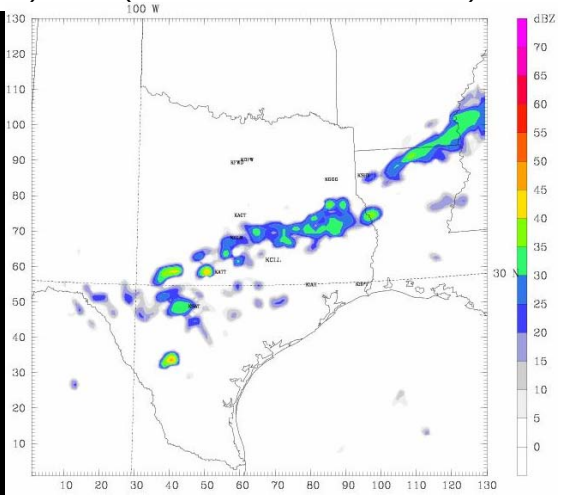

c) NEXRAD (1400 UTC 28 March 2006)

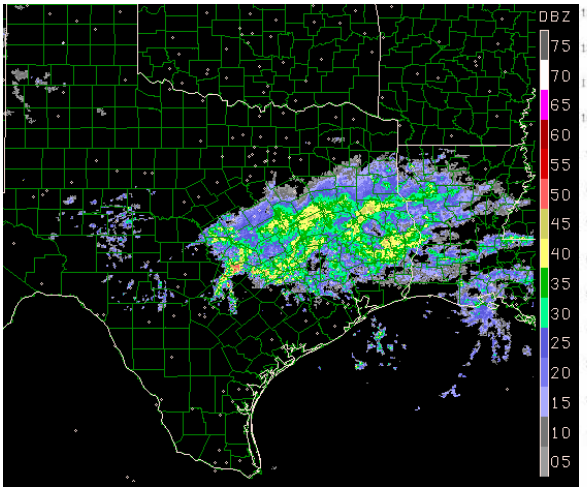

d) MM5 (1400 UTC 28 March 2006)

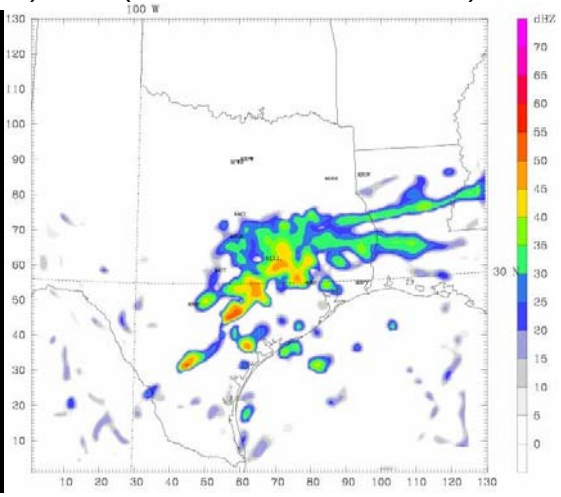

Figure 27 (a,c) NEXRAD and (b,d) MM5 reflectivity at the times indicated for the 28 March 2006 weakly baroclinic frontal case presented in section 5d.

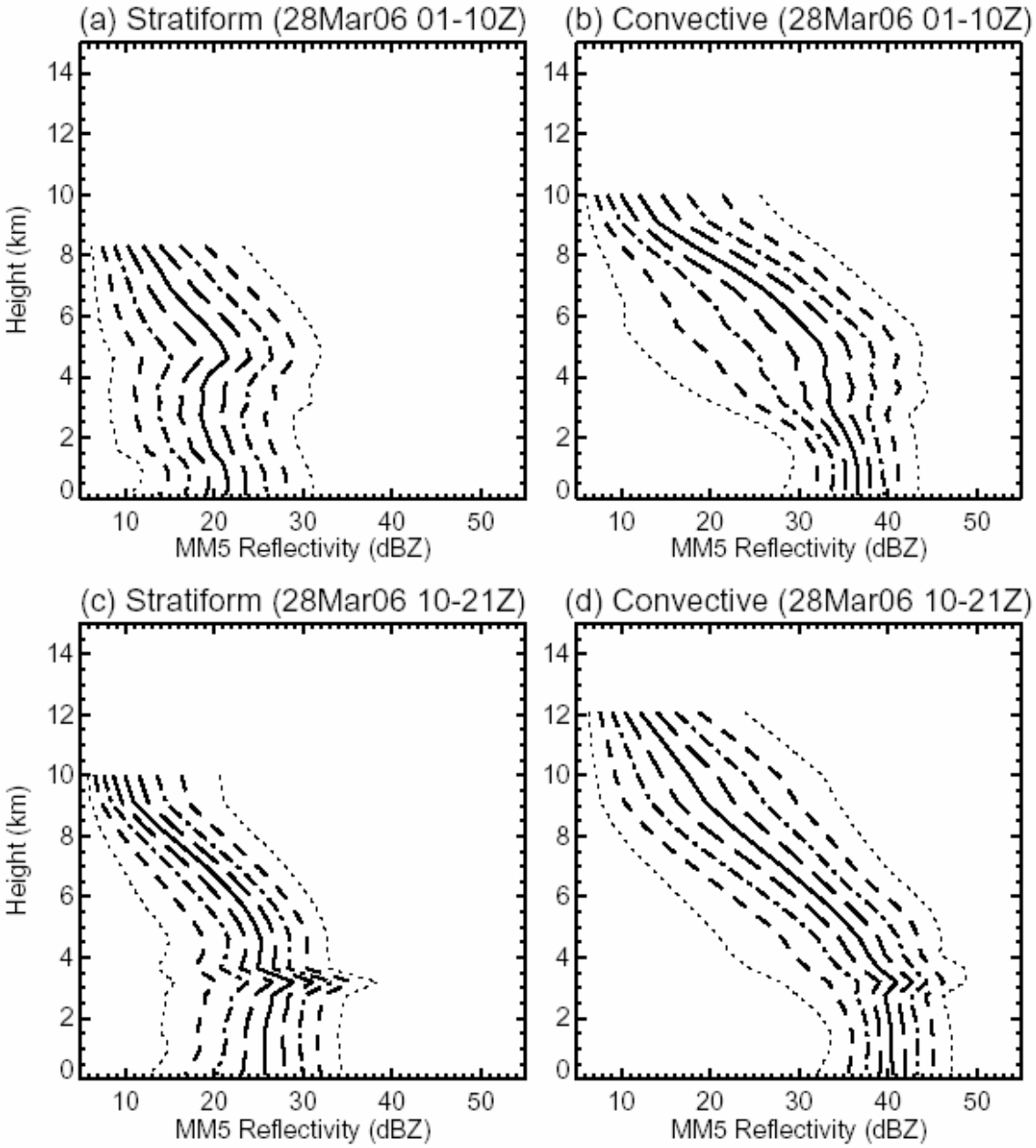

Figure 28 Vertical distributions of radar reflectivity for stratiform and convective rain in MM5 (a-b) for the stage of the storm with primarily elevated convection from 0100-0930 UTC on 28 March 2006 and (c-d) for the stage of the storm with deep convection from 1000-2100 UTC on 28 March 2006. Height levels with less than 0.5% of the total count are not plotted.

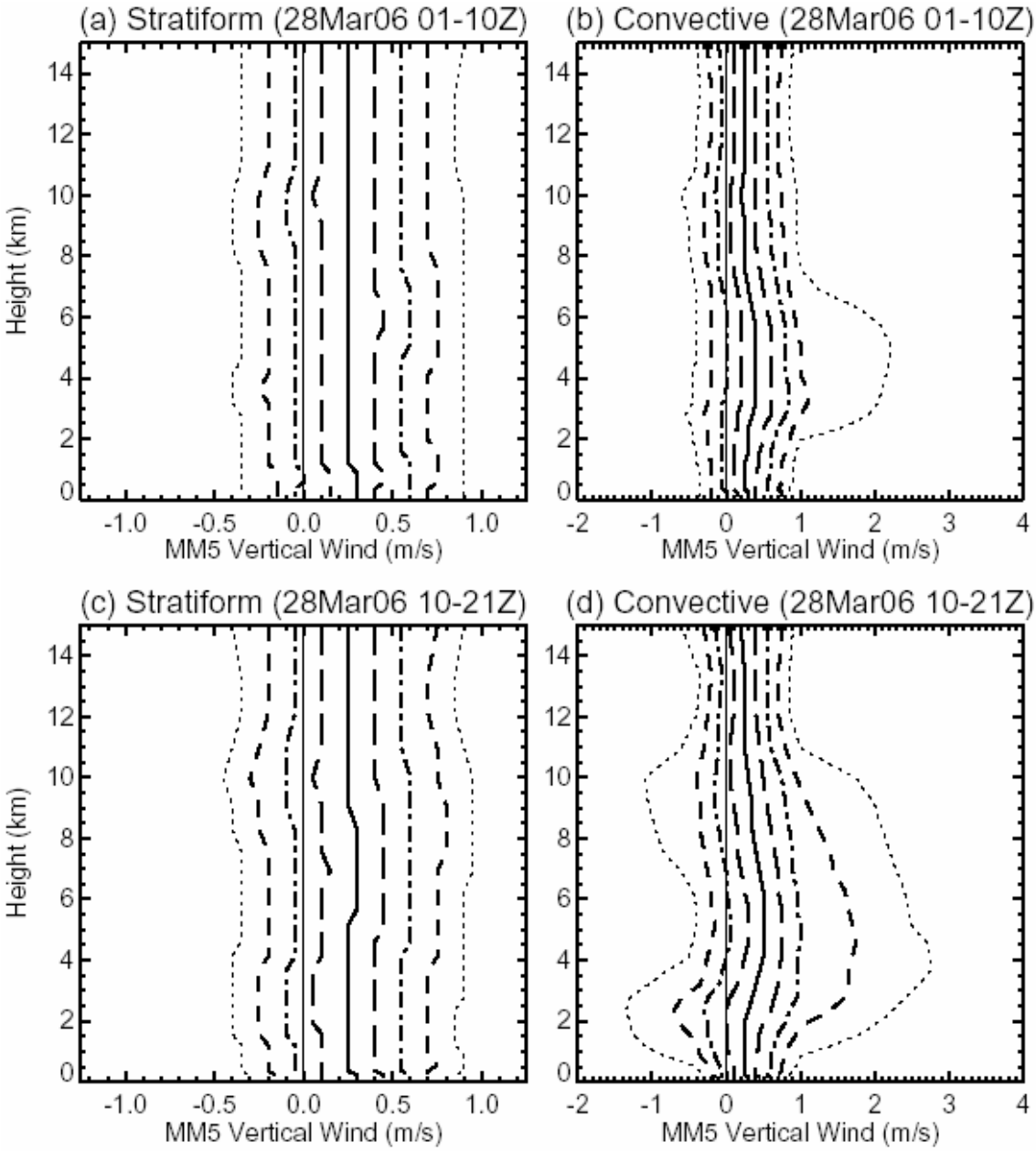

Figure 29 Vertical distributions of vertical velocity for stratiform and convective rain in MM5 (a-b) for the stage of the storm with primarily elevated convection from 0100-0930 UTC on 28 March 2006 and (c-d) for the stage of the storm with deep convection from 1000-2100 UTC on 28 March 2006.

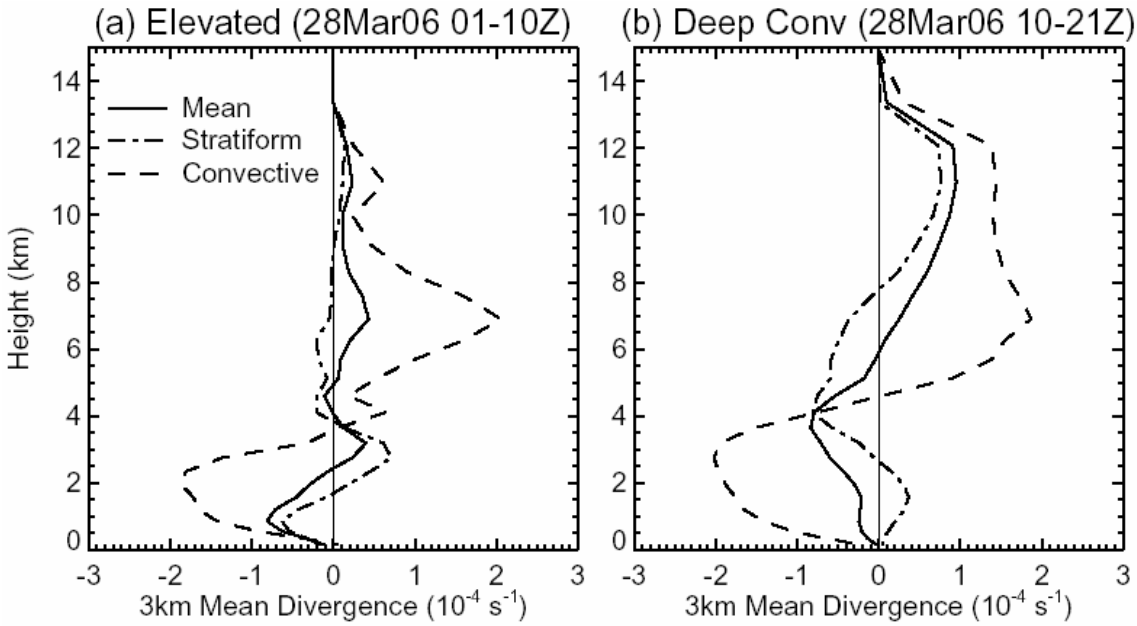

Figure 30 MM5-derived mean grid-scale divergence profiles for the 28 March 2006 weakly baroclinic frontal case using half-hourly model data following the plotting convection in Figs. 22. (a) Mean divergence profiles for the stage of the storm with primarily elevated convection from 0100-0930 UTC. (b) Mean divergence profiles for the stage of the storm with deep convection from 1000-2100 UTC.

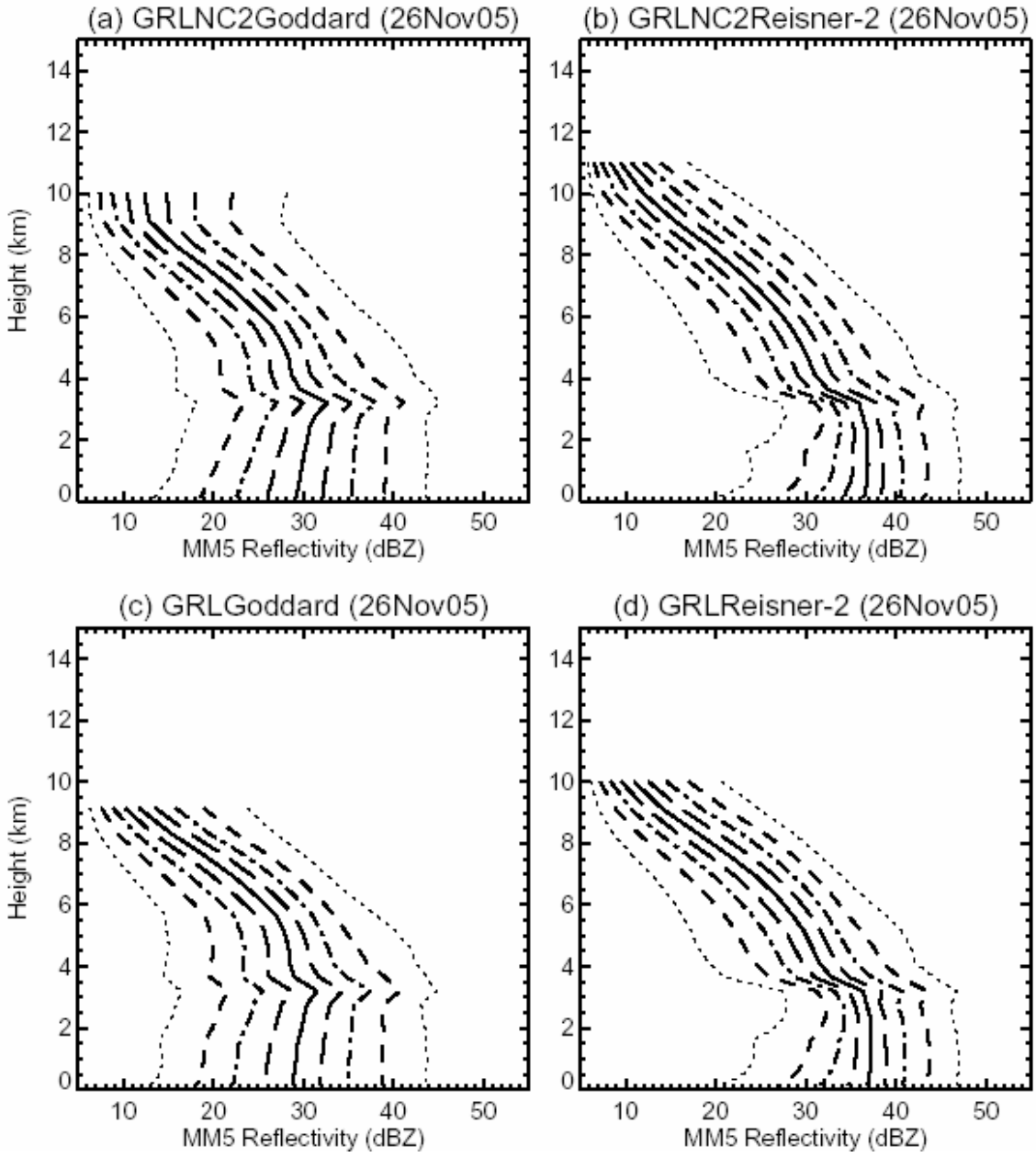

Figure 31 Vertical distributions of radar reflectivity in MM5 on 26 November 2005 for the model runs using (a) Grell cumulus on D1 only with Goddard microphysics, (b) Grell cumulus on D1 only with Reisner-2 microphysics, (c) Grell cumulus on D1 and D2 with Goddard microphysics, and (d) Grell cumulus on D1 and D2 with Reinser-2 microphysics. Height levels with less than 0.5% of the total count are not plotted.

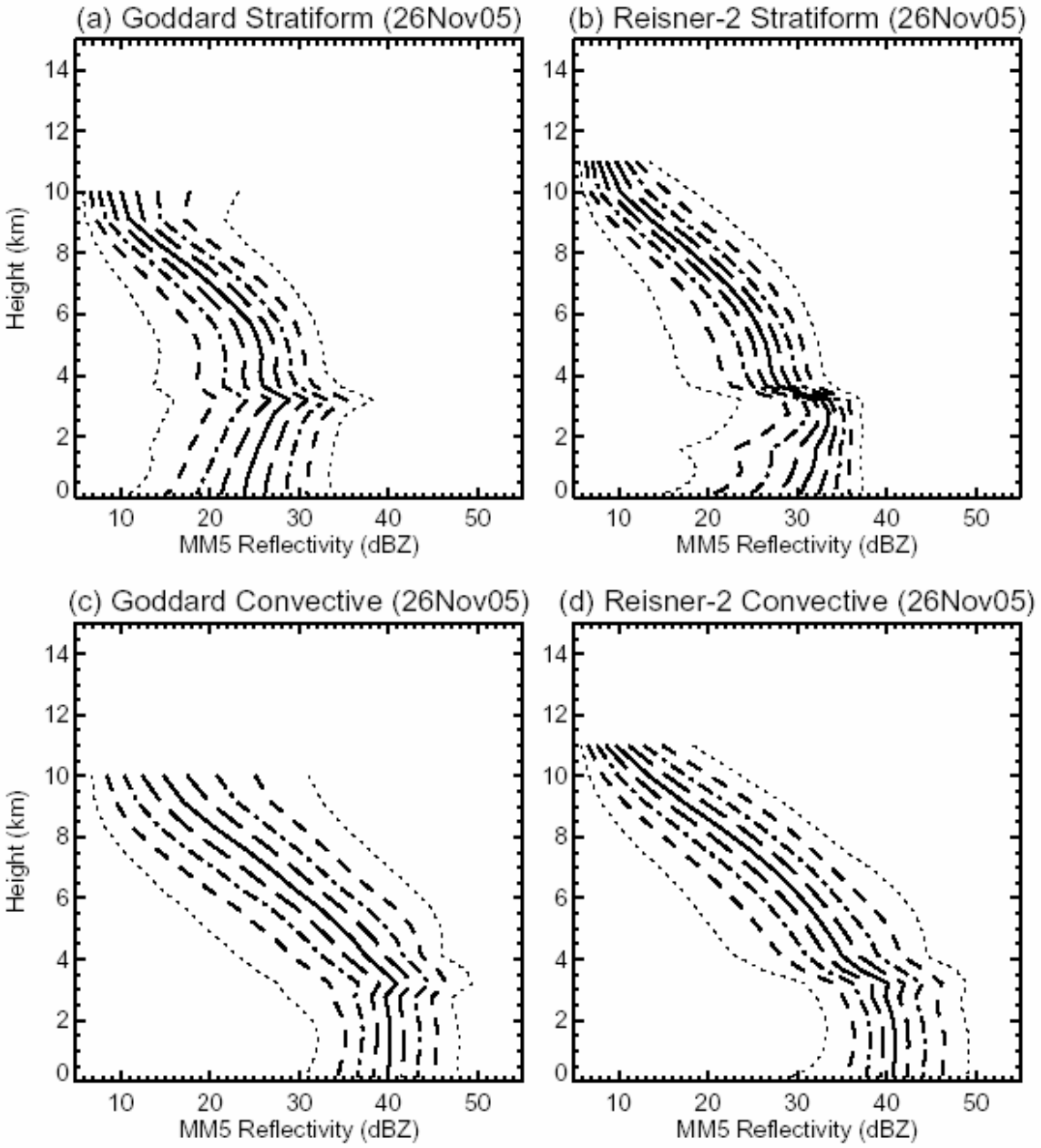

Figure 32 Vertical distributions of radar reflectivity for stratiform an convective rain in MM5 from 0900-2000 UTC on 26 November 2005 for the model runs using (a-b) Grell cumulus on D1 only with Goddard microphysics and (c-d) Grell cumulus on D1 only with Reisner-2 microphysics. Height levels with less than 0.5% of the total count are not plotted.

APPENDIX B: TABLES

Table 1 Occurrence of radar climatology storm types for the 74 identified storms (from Brugman 2007).

Dynamical Forcing	Precipitation Structure	Total
Cold Front (34%)	Well defined convective line (little stratiform)	6 of 25
	LLTS-MCS	5 of 25
	Less defined convective and stratiform regions	14 of 25
Stationary Front (16%)	Widespread rain (little or no convection)	3 of 12
	Regions of stronger convection (or LLTS-MCS)	9 of 12
Warm Front (7%)	Widespread rain (little or no convection)	1 of 5
	Regions of stronger convection	4 of 5
Weak Forcing (22%)	Isolated convective cells (little stratiform)	3 of 16
	Scattered convection w/stratiform (or LLTS-MCS)	13 of 16
Upper-level Disturbance (12%)	No subdivisions	9
Dryline (9%)	No subdivisions	7

Table 2 List of the storms in barotropic (BT), weakly baroclinic (WB), and strongly baroclinic (SB) environments modeled with their individual initialization times in MM5 along with the time periods the model calculations over the analysis domain (D3) are performed and the time periods these calculations are meant to represent as seen in NEXRAD observations.

Baroclinicity and Storm Type	**Initialization Date & Time**	**MM5 Analysis Time**	**NEXRAD Analysis Time**
BT, weak forcing	7/20/07 00Z	7/20 15Z-23Z	7/20 09Z-7/21 00Z
WB, upper-level disturbance	3/13/07 12Z	3/13 17Z-3/14 11Z	3/13 17Z-3/14 12Z
WB, upper-level disturbance	3/13/07 12Z	3/14 14Z-3/15 04Z	3/14 12Z-3/15 04Z
SB, upper-level disturbance	4/7/07 00Z	4/7 11Z-4/8 12Z	4/7 09Z-4/8 12Z
BT, upper-level disturbance	7/4/06 00Z	7/4 10Z-23Z	7/4 11Z-23Z
WB, upper-level disturbance	3/26/07 00Z	3/26 19Z-3/27 11Z	3/26 18Z-3/27 09Z
SB, upper-level disturbance	2/25/06 00Z	2/25 05Z-22Z	2/25 04Z-22Z
WB, cold frontal LLTS-MCS	6/18/06 00Z	6/18 06Z-16Z	6/18 05Z-15Z
SB, cold frontal LLTS-MCS	10/31/05 12Z	10/31 18Z-11/1 03Z	10/31 17Z-11/1 02Z
WB, stationary frontal	11/26/05 00Z	11/26 09Z-20Z	11/26 09Z-21Z
SB, cold frontal	1/13/07 00Z	1/13 05Z-1/14 17Z	1/13 04Z-1/14 14Z
WB, stationary frontal (elevated convection)	3/27/06 12Z	3/28 01Z-10Z	3/28 00Z-10Z
SB, stationary frontal (deep convection)	3/27/06 12Z	3/28 10Z-21Z	3/28 10Z-23Z

Table 3 Stratiform area fractions generated by different MM5 runs of the same storm.

Storm/Model Run	NC2gd	gd	NC2r2	r2		Mean	σ	gd σ	r2 σ
ADRAD-MM5									
7/20/2007 BT	56.0	56.9	29.1	21.6		**40.9**	**18.2**	0.6	5.3
3/13-14/07 WB	57.2	63.3	43.3	56.8		**55.2**	**8.4**	4.3	9.5
3/14-15/07 WB	51.8	59.8	45.7	59.9		**54.3**	**6.9**	5.7	10.0
4/7/07 SB	98.4	98.4	98.1	98.2		**98.3**	**0.2**	0.0	0.1
UL-DIST									
7/4/06 BT	59.3	55.2	31.4	31.5		**44.4**	**15.0**	2.9	0.1
3/26-27/07 WB	72.2	68.0	51.4	52.0		**60.9**	**10.8**	3.0	0.4
2/25/06 SB	79.5	80.6	70.5	80.8		**77.9**	**4.9**	0.8	7.3
LLTS-MCS									
6/18/06 WB	41.5	38.5	22.7	20.6		**30.8**	**10.7**	2.1	1.5
10/31/05 SB	52.9	49.0	36.7	37.9		**44.1**	**8.1**	2.8	0.8
FRONTAL									
11/26/05 WB	64.9	65.6	42.8	39.9		**53.3**	**13.9**	0.5	2.1
3/28/06 WB (all)	73.8	74.7	66.5	67.1		**70.5**	**4.3**	0.6	0.4
1/13-14/07 SB	76.9	78.7	81.4	84.3		**80.3**	**3.2**	1.3	2.1
3/28/06 (elevated)*	77.0	77.7	76.4	74.5		**76.4**	**1.4**	0.5	1.3
3/28/06 (deep)*	72.4	73.4	62.0	63.2		**67.8**	**6.0**	0.7	0.8
Mean	**65.4**	**65.7**	**51.6**	**54.2**				**2.0**	**3.3**
Standard Dev. (σ)	**15.5**	**15.9**	**22.9**	**25.1**					

*The "elevated" and "deep" parts of the 3/28/06 storm are not used to calculate the means and standard deviations of the stratiform area fractions.

NC2gd: Grell cumulus on D1 only; Goddard microphysics
Gd: Grell cumulus on D1 and D2; Goddard microphysics
NC2r2: Grell cumulus on D1 only; Reisner-2 microphysics
r2: Grell cumulus on D1 and D2; Reisner-2 microphysics

Table 4 Levels of non-divergence (LNDs; in km) generated by different MM5 runs of the same storm. When multiple LNDs are present, the one occurring directly above the greater peak in convergence is chosen.

Storm/Model Run	NC2gd	gd	NC2r2	r2		Mean	σ	gd σ	r2 σ
ADRAD-MM5									
7/20/2007 BT	6.8	4.8	4.9	4.0		**5.1**	**1.2**	1.4	0.6
3/13-14/07 WB	6.4	5.9	6.1	5.6		**6.0**	**0.3**	0.4	0.4
3/14-15/07 WB	4.7	5.1	4.7	3.7		**4.6**	**0.6**	0.3	0.7
4/7/07 SB	4.2	4.4	4.2	4.3		**4.3**	**0.1**	0.1	0.1
UL-DIST									
7/4/06 BT	8.1	4.9	5.5	4.3		**5.7**	**1.7**	2.3	0.8
3/26-27/07 WB	5.5	4.6	5.0	5.0		**5.0**	**0.4**	0.6	0.0
2/25/06 SB	4.5	3.7	4.4	3.6		**4.1**	**0.5**	0.6	0.6
LLTS-MCS									
6/18/06 WB	6.7	6.1	6.6	6.6		**6.5**	**0.3**	0.4	0.0
10/31/05 SB	5.8	5.5	5.8	5.6		**5.7**	**0.1**	0.2	0.1
FRONTAL									
11/26/05 WB	5.3	6.1	6.6	6.6		**6.2**	**0.6**	0.6	0.0
3/28/06 WB (all)	5.7	5.5	5.5	5.2		**5.5**	**0.2**	0.1	0.2
1/13-14/07 SB	2.6	2.1	2.7	2.3		**2.4**	**0.3**	0.4	0.3
3/28/06 (elevated)*	2.4	2.2	2.5	2.2		**2.3**	**0.1**	0.1	0.2
3/28/06 (deep)*	5.9	5.5	5.6	5.4		**5.6**	**0.2**	0.3	0.1
Mean	**5.5**	**4.9**	**5.2**	**4.7**				**0.6**	**0.3**
Standard Dev. (σ)	**1.4**	**1.1**	**1.1**	**1.3**					

*The "elevated" and "deep" parts of the 3/28/06 storm are not used to calculate the means and standard deviations of the total LND.

NC2gd: Grell cumulus on D1 only; Goddard microphysics
gd: Grell cumulus on D1 and D2; Goddard microphysics
NC2r2: Grell cumulus on D1 only; Reisner-2 microphysics
r2: Grell cumulus on D1 and D2; Reisner-2 microphysics

Table 5 Stratiform LNDs (in km) generated by different MM5 runs of the same storm. When multiple LNDs are present, the highest one is chosen.

Storm/Model Run	NC2gd	gd	NC2r2	r2		Mean	σ	gd σ	r2 σ
ADRAD-MM5									
7/20/2007 BT	9.0	8.9	8.6	9.2		**8.9**	**0.2**	0.1	0.4
3/13-14/07 WB	8.1	8.0	9.4	9.8		**8.8**	**0.9**	0.1	0.3
3/14-15/07 WB	7.4	7.5	7.8	7.3		**7.5**	**0.2**	0.1	0.4
4/7/07 SB	4.1	4.0	4.0	4.1		**4.1**	**0.1**	0.1	0.1
UL-DIST									
7/4/06 BT	9.7	9.6	9.2	7.1		**8.9**	**1.2**	0.1	1.5
3/26-27/07 WB	6.4	6.7	7.0	7.1		**6.8**	**0.3**	0.2	0.1
2/25/06 SB	4.9	5.9	5.0	6.0		**5.5**	**0.6**	0.7	0.7
LLTS-MCS									
6/18/06 WB	8.6	9.1	8.4	8.8		**8.7**	**0.3**	0.4	0.3
10/31/05 SB	7.0	7.0	7.1	6.5		**6.9**	**0.3**	0.0	0.4
FRONTAL									
11/26/05 WB	6.7	6.8	7.1	6.6		**6.8**	**0.2**	0.1	0.4
3/28/06 WB (all)	7.8	7.6	7.7	7.4		**7.6**	**0.2**	0.1	0.2
1/13-14/07 SB	8.2	8.0	7.5	7.8		**7.9**	**0.3**	0.1	0.2
3/28/06 (elevated)*	8.9	9.1	8.8	9.2		**9.0**	**0.2**	0.1	0.3
3/28/06 (deep)*	7.7	7.4	7.5	7.1		**7.4**	**0.2**	0.2	0.3
Mean	**7.3**	**7.4**	**7.4**	**7.3**				**0.2**	**0.4**
Standard Dev. (σ)	**1.6**	**1.5**	**1.6**	**1.5**					

*The "elevated" and "deep" parts of the 3/28/06 storm are not used to calculate the means and standard deviations of the stratiform LND.

NC2gd: Grell cumulus on D1 only; Goddard microphysics
gd: Grell cumulus on D1 and D2; Goddard microphysics
NC2r2: Grell cumulus on D1 only; Reisner-2 microphysics
r2: Grell cumulus on D1 and D2; Reisner-2 microphysics

Table 6 Convective LNDs (in km) generated by different MM5 runs of the same storm.

Storm/Model Run	NC2gd	gd	NC2r2	r2		Mean	σ	gd σ	r2 σ
ADRAD-MM5									
7/20/2007 BT	5.5	4.4	3.9	3.7		**4.4**	**0.8**	0.8	0.1
3/13-14/07 WB	5.8	5.6	5.5	5.3		**5.6**	**0.2**	0.1	0.1
3/14-15/07 WB	4.5	4.7	4.2	3.4		**4.2**	**0.6**	0.1	0.6
4/7/07 SB	5.8	5.9	5.9	5.9		**5.9**	**0.1**	0.1	0.0
UL-DIST									
7/4/06 BT	6.8	4.6	4.7	4.1		**5.1**	**1.2**	1.6	0.4
3/26-27/07 WB	5.1	4.2	4.8	4.6		**4.7**	**0.4**	0.6	0.1
2/25/06 SB	3.7	3.8	3.7	4.0		**3.8**	**0.1**	0.1	0.2
LLTS-MCS									
6/18/06 WB	6.0	5.7	6.0	6.0		**5.9**	**0.2**	0.2	0.0
10/31/05 SB	5.3	5.1	5.2	5.1		**5.2**	**0.1**	0.1	0.1
FRONTAL									
11/26/05 WB	4.3	4.2	4.5	4.3		**4.3**	**0.1**	0.1	0.1
3/28/06 WB (all)	4.5	4.1	4.5	3.9		**4.3**	**0.3**	0.3	0.4
1/13-14/07 SB	3.5	3.4	3.6	3.6		**3.5**	**0.1**	0.1	0.0
3/28/06 (elevated)*	3.6	2.9	3.7	3.1		**3.3**	**0.4**	0.5	0.4
3/28/06 (deep)*	4.6	4.2	4.6	4.0		**4.4**	**0.3**	0.3	0.4
Mean	**5.1**	**4.6**	**4.7**	**4.5**				**0.3**	**0.2**
Standard Dev. (σ)	**1.0**	**0.8**	**0.8**	**0.9**					

*The "elevated" and "deep" parts of the 3/28/06 storm are not used to calculate the means and standard deviations of the convective LND.

NC2gd: Grell cumulus on D1 only; Goddard microphysics
gd: Grell cumulus on D1 and D2; Goddard microphysics
NC2r2: Grell cumulus on D1 only; Reisner-2 microphysics
r2: Grell cumulus on D1 and D2; Reisner-2 microphysics

VITA

Name: Larry John Hopper, Jr.

Address: Department of Atmospheric Sciences, Texas A&M University
3150 TAMU, College Station, TX 77843-3150

Email Address: lhopper@ariel.met.tamu.edu

Education: B.S., Meteorology, University of Oklahoma, May 2005
M.S., Atmospheric Sciences, Texas A&M University, May 2008

Experience: Department of Atmospheric Sciences, Texas A&M University
Graduate Research Assistant (July 2005 to present)
University College, University of Oklahoma
Teaching Assistant (Fall 2004, Fall 2005, and Spring 2005)
Summer Enrollment Guide (May 2003-August 2003)
Department of Chemistry and Biochemistry, University of Oklahoma
Teaching Assistant (Fall 2002 to Spring 2005; 5 semesters)
Housing and Food Services, University of Oklahoma
Resident Advisor (August 2004 to May 2005)
KOCO-TV (ABC), Oklahoma City, OK
Weather Intern (June 2002 to May 2005)

Awards: Leitseizer Honor List (top 26 seniors campus-wide), OU, April 2005

Publications: Hopper, L. J., Jr., and C. Schumacher, 2007: Baroclinicity influences on storm divergence in the subtropics. Preprints, *87th AMS Annual Meeting*, San Antonio, TX, Amer. Meteor. Soc.

Presentations: Hopper, L. J., Jr., and C. Schumacher: "Effects of baroclinicity on stratiform rain production and storm divergence in the subtropics", Oral Presentation, *12th Conference on Mesoscale Processes*, Waterville Valley, NH. (August 2007)
Hopper, L. J., Jr., and C. Schumacher, K. Brugman, C. Hernandez, U. Karadkar, M. Nordt, and R. Furuta: "Undergraduate experience with technology in an education and research program to measure and understand the climatology of storms in Southeast Texas", Oral Presentation, *88th Annual AMS Meeting*, New Orleans, LA. (January 2008)

Courses Taught: ATMO 203, *Weather Forecasting Lab for Majors*: Fall 2006 (3 sect.)
ATMO 291/491 TA, *Research (SOAP)*: Spring 2006-2008
ATMO 201 TA, *Introduction to Atmospheric Science*: Spring 2006